MICROSTRUCTURE, TENSILE, AND CORROSION CHARACTERISTICS OF SIMILAR AND DISSIMILAR JOINTS OF FSW AA5086-H32 AND AA6061-T6511 FROM VARIOUS ATMOSPHERIC ENVIRONMENTS

A THESIS SUBMITTED TO THE GRADUATE DIVISION OF THE
UNIVERSITY OF HAWAIʻI AT MĀNOA IN PARTIAL FULFILLMENT OF
THE REQUIREMENTS FOR THE DEGREE OF

MASTER OF SCIENCE

IN

MECHANICAL ENGINEERING

March 2016

By

Khoa Anh Huynh

Thesis Committee:

Lloyd H. Hihara, Chairperson
Jingjing Li
Scott Miller

Acknowledgments

Dr. Lloyd H. Hihara was a pivotal contribution to developing this thesis, and I would like to thank him with the highest level of gratitude. He provided crucial insights to progress and steer the thesis; and this thesis may not have materialized without this endless support. I would also like to thank Dr. Jingjing Li and Dr. Scott Miller for agreeing to serve on the thesis committee.

Funding for this study was made possible by the Office of the Under Secretary of Dense for the project entitled “Correlation of Field and Laboratory Studies on the Corrosion of Various Alloys in a Multitude of Hawaii Micro-climates” (U.S. Air force Academy, Contract no.: FA7000-10-2-0010). Specifically, much appreciation is owed to Mr. Daniel Dunmire, Director, Corrosion Policy and Oversight, Office of the Under Secretary of Defense.

Additionally, I would like to recognize Mr. Ryan Sugamoto and Dr. Raghu Srinivasan of the Hawaii Corrosion Laboratory for their support in various portions of the development of the results provided here. Specifically, Ryan was instrumental in maintaining the samples over the course of the experiment and collecting the weather data. Natalie Wohner was a helpful lab-mate in helping me to develop a keen understanding of the scanning electron microscope. She also was integral in analyzing the unexposed samples. Also, my colleagues within the Hawaii Corrosion Laboratory—Brent Howard and Kate Quiambao—provided exceptional motivation and a safe working environment. Also, Mrs. Jamie Wong was critical in booking airfares to various test sites—thank you.

To all of my friends on Oahu and those who visited me, thank you for being the best stress reliever and bringing happiness to my life. Specifically, thank you Dan, Evan, J.J., Krishna, and Paige for your comedic relief and for showing me life outside of the lab.

Lastly and most importantly, thank you Don, Tracey, Quyen, Jenny, Mina, and extended family members for your love, support, and encouragement. The peace and tranquility that you provided me during my time at UH Manoa was paramount to completing this thesis.

I, humbly, dedicate this work to my younger sister. Shoot for the stars Jenny.

Abstract

Corrosion behavior, tensile properties, and microstructure of similar and dissimilar Friction Stir Welded (FSW) butt-joints between AA5086 and AA6061 exposed to five atmospheric environments—acidic, rainforest, mild marine, harsh marine, and arid— for three exposure periods—6-month, 1-year, and 2-year—were investigated. Weight loss test via the ISO 8407:1991 (E) C.1.1, tensile test via the Instron-5500R testing machine, and microstructure characterization via the Scanning Electron Microscope (SEM) equipped with an Oxford Instrument energy dispersive X-Ray analyzer (EDXA) were conducted. Results show that AA5086 similar welds had best corrosion resistance in the most severe case, 2-year at acidic test site. Yield strength changes were insignificant over time and between test sites. AA5086 similar welds had the highest ultimate tensile strength (UTS), but also had the highest degradation; further investigation showed premature fractures. AA6061 similar welds and AA6061-AA5086 dissimilar welds shared same UTS with the latter being slightly lower. AA5086 similar welds had the highest elongation percentage. AA6061-AA5086 dissimilar weld samples exposed in the most severe test scenario exhibited marked changes in elemental composition and surface features at the parent material zone (PM), heat affected zone (HAZ), thermo-mechanically affected zone (TMAZ), and nugget zone (NZ) when compared to an unexposed sample. The microstructure of 2-year samples exposed at the three most corrosive sites was also discussed. This study provides better understanding of similar and dissimilar FSW butt-joints of AA6061 and AA5086 for potentially greater application in shipping and aerospace industries.

Table of Contents

Acknowledgments 2

Abstract 4

Table of Contents 5

List of Figures 8

List of Tables 11

Chapter 1 12

1.1 Objectives of this Study 12

Chapter 2 13

2.1 Description of FSW 13

2.2 Microstructure of FSW Alloys 14

2.2.1 Nugget Zone 15

2.2.2 Thermo-mechanically affected zone 15

2.2.3 Heat Affected Zone 16

2.3 Tensile Strength of FSW Alloys 16

2.4 Corrosion of FSW Alloys 17

Chapter 3 19

3.1 Base Metal 19

3.2 Friction Stir Welding Method 19

3.3 Atmospheric Corrosion Method 21
3.3.1 Test Sites 21
3.3.2 Recorded Test Sites Atmospheric Conditions 24
3.3.3 Procedure 25
3.4 Weight Loss Method 26
3.5 Tensile Characterization Method 27
3.6 Microstructure Characterization Method 28
Chapter 4 30
4.1 Weight Loss 30
4.1.1 Results 30
4.1.2 Discussion 33
4.2 Tensile Test 34
4.2.1 Results 34
4.2.2 Discussion 42
4.3 Microstructure 48
4.3.1 Results 48
4.3.2 Discussion 72
Chapter 5 77
5.1 Corrosion Behavior 77
5.2 Mechanical Properties 77

5.3 Microstructure 79

5.3.1 Comparison of Unexposed Parent Metal and the Two-Year, Kilauea-Exposed AA6061-AA5086 Weld Samples 79

5.3.2 Comparison of Two-Year Exposure Samples at Kilauea, Pyramid Rock, and Lyon Arboretum 81

References 83

List of Figures

Figure 1: FSW Process. 14

Figure 2: Typical cross section of FSW displaying the various zones. 15

Figure 3: Vectrax CL Series Three Phase Knee Milling Machine Used for FSW. [28] 19

Figure 4: AA6061-AA6061 FSW test coupons before flash machined. 20

Figure 5: Five locations for atmospheric corrosion testing in Hawai'i. [29] 22

Figure 6: Exposed Samples Layout and Orientation at Kilauea. 25

Figure 7: Locations of yield and ultimate strengths example (AA5086-AA5086 at Pyramid Rock for 2-year. 27

Figure 8: Orientation of dog-bone to FSW of AA6061-AA5086. 28

Figure 9: Unexposed BM of AA5086 (left), BM of AA6061 (center), NZ-up (right 1), NZ-down (right 2), HAZ AA5086 (right 3), HAZ AA6061 (right 4), TMAZ AA5086 (right 6), and TMAZ AA6061 (right 7). 29

Figure 10: Comparison of corrosion rates for the three welded materials grouped by test site and exposure period. Abbreviations: 6061 – AA6061-AA6061 weld specimen; 5086 – AA5086-AA5086 weld specimen; 61-86 – AA6061-AA5086 weld specimen. 31

Figure 11: Comparison of corrosion rates for the three time exposures grouped by test site and material type. Abbreviations: 6061 – AA6061-AA6061 weld specimen; 5086 – AA5086-AA5086 weld specimen; 61-86 – AA6061-AA5086 weld specimen. 32

Figure 12: Comparison of corrosion rates for the five test sites grouped by the exposure time and material type. Abbreviations: 6061 – AA6061-AA6061 weld specimen; 5086 – AA5086-AA5086 weld specimen; 61-86 – AA6061-AA5086 weld specimen. 33

Figure 13: Stress-strain curves for the three materials at Kilauea for two years (AP### is AA6061-AA6061, BP### is AA5086-AA5086 and CP### is AA6061-5086). 35
Figure 14: Average stress-strain curves for the three materials at Pyramid Rock for two years (AP is AA6061-AA6061, BP is AA5086-AA5086, and CP is AA6061-AA5086). 36
Figure 15: Yield strength. Comparison of exposure times grouped by test site and material type. Abbreviations: 6061 – AA6061-AA6061 weld specimen; 5086 – AA5086-AA5086 weld specimen; 61-86 – AA6061-AA5086 weld specimen. 37
Figure 16: Yield strength. Comparison of material type grouped by test site and exposure time. Abbreviations: 6061 – AA6061-AA6061 weld specimen; 5086 – AA5086-AA5086 weld specimen; 61-86 – AA6061-AA5086 weld specimen. 38
Figure 17: Yield strength. Comparison of test sites grouped by exposure time and material type. Abbreviations: 6061 – AA6061-AA6061 weld specimen; 5086 – AA5086-AA5086 weld specimen; 61-86 – AA6061-AA5086 weld specimen. 38
Figure 18: UTS. Comparison of exposure times grouped by test site and material type. Abbreviations: 6061 – AA6061-AA6061 weld specimen; 5086 – AA5086-AA5086 weld specimen; 61-86 – AA6061-AA5086 weld specimen. 39
Figure 19: UTS. Comparison of material type grouped by test site and exposure time. Abbreviations: 6061 – AA6061-AA6061 weld specimen; 5086 – AA5086-AA5086 weld specimen; 61-86 – AA6061-AA5086 weld specimen. 39
Figure 20: UTS. Comparison of test sites grouped by exposure time and material type. Abbreviations: 6061 – AA6061-AA6061 weld specimen; 5086 – AA5086-AA5086 weld specimen; 61-86 – AA6061-AA5086 weld specimen. 40

Figure 21: Strain to failure. Comparison of exposure times grouped by test site and material type. Abbreviations: 6061 – AA6061-AA6061 weld specimen; 5086 – AA5086-AA5086 weld specimen; 61-86 – AA6061-AA5086 weld specimen. 40

Figure 22: Strain to failure. Comparison of material type grouped by test site and exposure time. Abbreviations: 6061 – AA6061-AA6061 weld specimen; 5086 – AA5086-AA5086 weld specimen; 61-86 – AA6061-AA5086 weld specimen. 41

Figure 23: Strain to failure. Comparison of test sites grouped by exposure time and material type. Abbreviations: 6061 – AA6061-AA6061 weld specimen; 5086 – AA5086-AA5086 weld specimen; 61-86 – AA6061-AA5086 weld specimen. 41

Figure 24: Fracture surface of AA5086-AA5086 welds at Kilauea for 2-year exposure. 44

Figure 25: Fracture surface of AA5086-AA5086 welds at Waipahu for 1-year exposure. 45

Figure 26: Fracture surface of AA5086-AA5086 welds at Lyon Arboretum 6-month exposure. ..46

Figure 27: Fracture surface of AA5086-AA5086 welds at Lyon Arboretum 1-year exposure. 47

Figure 28: Chemical Composition of AA6061- AA6061 at Kilauea for Two Years. 56

Figure 29: Chemical Composition of AA5086-AA5086 at Kilauea for Two Years. 58

Figure 30: Chemical Composition of AA6061-AA5086 at Kilauea for Two Years. 60

Figure 31: Chemical Composition of AA6061-AA6061 at Pyramid Rock for Two Years. 62

Figure 32: Chemical Composition of AA5086-AA5086 at Pyramid Rock for Two Years. 64

Figure 33: Chemical Composition of AA6061-AA5086 at Pyramid Rock for Two Years. 66

Figure 34: Chemical Composition of AA6061-AA6061 at Lyon Arboretum Rock for Two Years. 68

Figure 35: Chemical Composition of AA5086-AA5086 at Lyon Arboretum for Two Years. 70

Figure 36: Chemical Composition of AA6061-AA5086 at Lyon Arboretum for Two Years. 72

List of Tables

Table 1. Chemical Composition of AA5086 and AA6061 in Weight %.[27] 19

Table 2. Test Sites. 24

Table 3. Annual Average Weather Data of Five Test Sites. [32] 24

Table 4. Parent Material. (EDXA region in red) 49

Table 5. EDX Analysis of Parent Metal compared to ASTM Standard.[34] 49

Table 6. HAZ of AA5086 Side. 50

Table 7. HAZ of AA6061 Side. 51

Table 8. TMAZ of AA5086. 52

Table 9. TMAZ of AA6061. 52

Table 10. Comparison of the Topside and Underside of the AA6061-AA5086 Nugget Zone 53

Table 11. SEM of AA6061-AA6061 at Kilauea for Two Years. (EDXA regions in red) 55

Table 12. SEM of AA5086-AA5086 at Kilauea for Two Years. (EDXA regions in red) 57

Table 13. SEM of AA6061-AA5086 at Kilauea for Two Years. (EDXA regions in red) 59

Table 14. SEM of AA6061-AA6061 at Pyramid Rock for Two Years. (EDXA regions in red)....61

Table 15. SEM of AA5086-AA5086 at Pyramid Rock for Two Years. (EDXA regions in red)....63

Table 16. SEM of AA6061-AA5086 at Pyramid Rock for Two Years. (EDXA regions in red)....65

Table 17. SEM of AA6061-AA6061 at Lyon Arboretum for Two Years. (EDXA regions in red).67

Table 18. SEM of AA5086-AA5086 at Lyon Arboretum for Two Years. (EDXA regions in red).69

Table 19. SEM of AA6061-AA5086 at Lyon Arboretum for Two Years. (EDXA regions in red).71

Chapter 1

INTRODUCTION

Friction Stir Welding, FSW, is a relatively new solid state joining process invented by The Welding Institute in 1991 [1]. The technique is gaining popularity in joining a wide range of aluminum alloys for numerous applications due to advantages such as lower heat input and weight reduction relative to conventional welding processes such as inert gas and arc welding. Large industries such as shipping and aeronautics can benefit greatly. AA5086 is used widely in the former for its high strength and good corrosion resistance while AA6061 is used significantly in the latter for its weldability and good corrosion. However, few studies have taken into consideration the microstructure and corrosion characteristics of these metals in relation to FSW. This study attempts to bridge that gap by investigating the corrosive, mechanical, and microstructure properties of FSW butt joints of AA6061-AA6061, AA5086-AA5086, and AA6061-AA5086.

1.1 Objectives of this Study

Specifically, the study will investigate FSW samples of AA6061-AA6061, AA5086-AA5086, and AA6061-AA5086 exposed for 6-months, 1-year, and 2-year at five test sites representing arid, harsh marine, mild marine, acidic, and rainforest environments to assess the degree of corrosion, to explore the mechanical properties changes, and to characterize the microstructural changes.

Chapter 2

LITERATURE REVIEW

2.1 Description of FSW

Due to its unique characteristics, aluminum alloys have been utilized in major transportation industries such as aerospace, automotive, and shipbuilding. However, conventional fusion welding of aluminum alloys, such as 2xxx and 7xxx, has been relatively difficult. Friction Stir Welding (FSW) is a new welding technique, invented at The Welding Institute of UK in 1991, whereby the aluminum alloys are welded through a solid-state welding process. According to Murray W. Mahoney from the Rockwell Scientific Company, FSW can and most often have superior properties compared to fusion welds since there is no melting of the alloys during the process [1].

In general, FSW generates frictional heat between a rotating probe made of a harder material than the two base metals being welded as shown in Figure 1. The frictional heat from the probe, as well as the larger diameter shoulder, creates a plasticized condition in the abutting base metals [2]. As the probe rotates and translates, the highly plasticized material from both base metals is redistributed from the leading edge to the trailing edge of the probe—where it cools to form a solid-state weld.

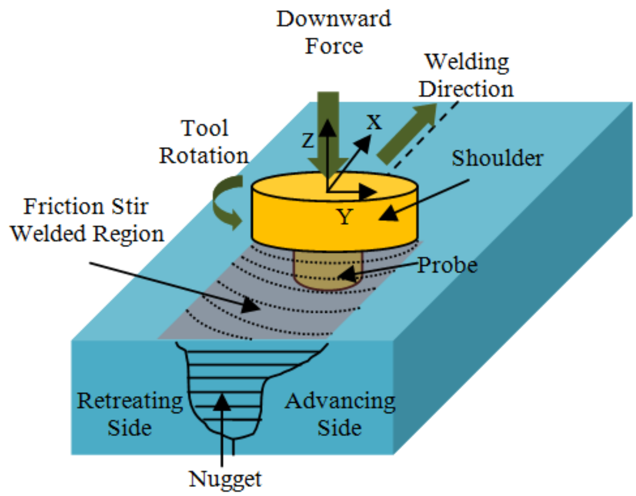

Figure 1: FSW Process.

Because FSW can be done below the melting temperature of the base metals, the consolidated welds do not exhibit fusion welding defects like porosity. Furthermore, no consumable filler materials, shielding gas, or edge preparation are required which reduces as much as 10% of the final weight compared to traditional welding [4]. In regards to metallurgical advantages, FSW has low distortion of the work piece(s), excellent properties in the joint area, and no cracking [3]. Other benefits include the discontinuation of surface cleaning and the use of only 2.5% of the energy needed for a laser weld. The reduction in overall weight and energy consumption make FSW an attractive option for the transportation industries.

2.2 Microstructure of FSW Alloys

The plastic deformation and near-melting temperature caused by the rotating and translating probe moving between the two work pieces create three distinct zones apart from the base metal (BM): the nugget zone (NZ), the thermo-mechanically affected zone (TMAZ), and the heat affected zone (HAZ) [5-10]. In general, the NZ and the TMAZ are dynamically different to the base metal in regard to their grain orientation, shape, and size. While weld parameters, such as rotational speed, probe design, and cool rate, directly impact the morphology and structure of the grains and precipitates in the various zones, the following summary generalizes the differing results to create a general overview. Figure 2 below illustrates the grain structures of the various zones.

Figure 2: Typical cross section of FSW displaying the various zones.

2.2.1 Nugget Zone

The nugget zone is often characterized by a recrystallized fine and equiaxed grain with 2-4 µm in diameter caused by the immense plastic deformation and frictional heating the welding process [11]. As seen in Figure 1, concentric circles are present in this zone as a result of the rotating probe creating increments of plastic deformation. The rotation relative to the translating direction of the weld piece causes the nugget zone to be asymmetrical. Additionally, precipitates are not as likely to nucleate as in the base metal.

2.2.2 Thermo-mechanically affected zone

Unique to FSW and situated outside of the NZ where the strain and temperature is lower, the microstructure of the TMAZ exhibits a highly deformed structure with virtually no sign of recrystalization compared to the nugget zone [12]. Within the TMAZ, dissolution of some precipitates was observed due to high-temperature exposure; and grains usually contain a high density of sub-boundaries [13].

2.2.3 Heat Affected Zone

As the name suggests, the material in this zone is subjected only to the frictional heat and not plastic deformation. It is located between the base material and the TMAZ. Yet, exposure to the high temperature may still significantly affect the microstructure. This region has the lowest microhardness of all post welding. It exhibits an elongated grain structure similar to the base metal, but it has a larger precipitate free zone [7]. Jata et al. [14] found that FSW resulted in coarsening of the strengthening precipitates and the precipitate free zone.

2.3 Tensile Strength of FSW Alloys

In general, aluminum is easily machined, casted, drawn, and extruded compared to other metals such as steel. In regard to tensile strength of after being stir-welded, the result is a function of a host of factors such as tool travel speed, tool rotation rate, tool design, tool tilt, material thickness, alloy composition, initial material temper, cooling rate, heat sink, test sample size, surface oxides, joint design, and natural aging [1]. For butt joints, Silva et al. [15] reported that the top three parameters, from most to least significant, are probe penetration, welding speed and shoulder/probe diameter ratio interaction, and rotational speed and shoulder/probe diameter ratio interaction. They concluded that 1000 rpm, 290 mm/min, shoulder of 15 mm, and probe penetration of 2.85 mm should be applied for various butt welds of AA6082-T6 aluminum alloy. Furthermore, the study found that the tensile strength efficiency (weld/base material tensile strengths) was 76% for butt welds. Krasnowski et al. [16] reported 68%-73% for Al 6062 whereby the higher tensile strength efficiency was achieved with a conventional probe consisting of a housing, a cylindrical threaded probe, and a shoulder with a grooved spiral. Aditya et al. [17] reported 63.95-78.56% for AA-2024 and 40.85-51.72% for AA-5754. Krasnowski et al. [18] have noted that welded samples invariably fracture within the welded area.

Welding, whether fusion welding or friction stir welding, often combines dissimilar materials as well as similar. Shigematsu et al. [18] investigated FSW of dissimilar AA6061–AA5083 and reported that welding properties, such as the hardness distribution and the tensile strength, are strongly influenced by the material combination. Leital et al. [19] reported that AA6016-T4 similar welds and AA6016-T4-AA51 dissimilar welds experienced a 10-20% strength reduction relative to the parent metals along with important losses in ductility. Miles et al. [20] studied various combinations of similar and dissimilar joining of AA-5182-O, AA-5754-O, and 6022-T4 and concluded that 5182/5754 alloy pairs maintained good formability compared to parent metal while 5182/6022 and 5754/6022 had significantly reduced formability with failures occurring in the HAZ of 6022.

2.4 Corrosion of FSW Alloys

Aluminum is touted for its excellent corrosion resistivity, and studies regarding this are abundant. This unique characteristic results from aluminum's passivity produced by a protective oxide film that is bonded tightly to its surface [21]. Passivation occurs when certain ranges of potential and pH coincide, which differ among materials. Additionally, when the film is damaged, aluminum has the ability to reform the oxide film with varying degree depending on the environment; however, if the damage is too severe, then corrosion will take place usually in the form of aluminum hydroxide $Al(OH)_3$ and boehmite AlO(OH) in low and high temperature, respectively [21].

Natural atmospheric corrosivity of aluminum varies due to the different conditions present at different sites despite belonging to the same atmospheric category such as marine. Additionally, corrosivity varies for different types of aluminum alloys. Thus, corrosion rates ranging from 0.03 to 4.1 µm/yr have been reported from atmospheric tests on aluminum in various locations around the world [22]. Aesthetically, aluminum corrodes by roughening of the surface as a result of pitting and turning gray, matted gray, and jet black in rural, marine, and industrial atmospheres, respectively [22].

FSW AA5086 and AA6061 have not been tested in various atmospheric conditions, but an aqueous corrosion experiment has been conducted. Chen [23] specifically investigated the corrosion of FSW AA5086 and AA6061 Al alloys by immersing them in 3.15% NaCl, 0.5 M Na_2SO_4 and ASTM sea water for 90 and 120 days at 30^{o}C. Chen [23] found that the corrosion rate for the alloys was highest in the 3.15% NaCl, then ASTM sea water, and then the 0.5 Na_2SO_4. Most importantly, this study concluded that the HAZ has the best corrosion resistance of the various regions.

Sensitization has been documented to affect the AA5086 used in this study and the 5XXX family more broadly. Sensitization results in degraded mechanical properties. Generally, higher concentration of Mg in Al-Mg alloys leads to increased strength meanwhile producing the adverse effect of decreased corrosion resistance. Specifically, the solid solution in Al-Mg alloys with $\geq$3 wt.% of Mg is supersaturated at room temperature and the excess Mg solute atoms are predisposed to precipitate out as highly anodic β-phase (Mg_5Al_8) particles where they tend to migrate to the grain boundaries leading to susceptibility in intergranular corrosion or stress corrosion cracking [24-26].

Chapter 3

MATERIALS AND METHODS

3.1 Base Metal

The two aluminum alloys used in this study were AA6061-T6511 and AA5086-H32. They were supplied by McMaster-Carr with the following chemical composition (Table 1).

Table 1. Chemical Composition of AA5086 and AA6061 in Weight %.[27]

	Cu	**Mn**	**Mg**	**Zn**	**Cr**	**Ti**	**Si**	**Fe**	**Al**
AA5086	≤0.10	0.2~0.7	3.5~4.5	0.25	0.05~0.25	0.15	≤0.4	≤0.5	Balance
AA6061	0.05~0.4	≤0.15	0.8~1.2	≤0.25	0.4~0.8	≤0.15	0.4~0.8	≤0.7	Balance

3.2 Friction Stir Welding Method

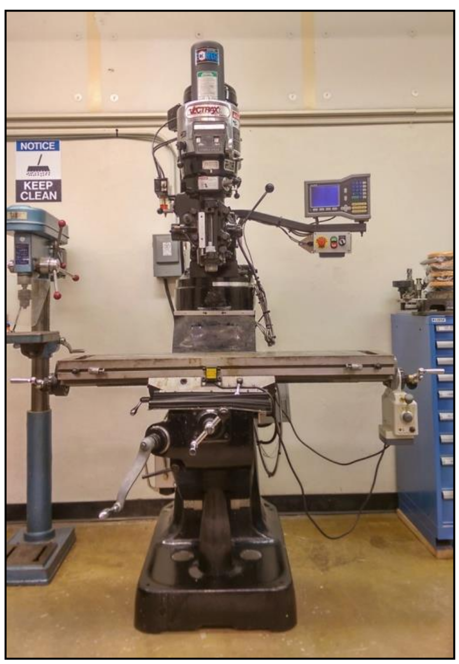

Figure 3: Vectrax CL Series Three Phase Knee Milling Machine Used for FSW.

The Vectrax CL Series Milling Machine in Figure 3 was used to create the FSW of the AA6061 and AA5086 in this study. Furthermore, the FSW in this investigation utilized an 8 mm in diameter and 6.35 mm long welding probe with a shoulder of 25 mm in diameter. The rotational speed was 1000 RPM and the translational speed was 20 mm/min with the probe angles at 3° towards the fed material. The probe was manually driven into the joining materials in the z direction. These parameters were selected to join AA6061 with AA6061, AA5086 with AA5086, and AA6061 with AA5086. Once the two base metals were friction stir welded, the plates were partitioned into smaller test coupons. Figure 4 below displays the topside of the AA6061-AA6061 test coupons after the FSW and partitioning of the coupons and before the flash formation and surface layers were machined off. The coupons exhibit a transversal weld. On some plates, the flash and surface layers were machined off first prior to the section of the specimen into smaller samples.

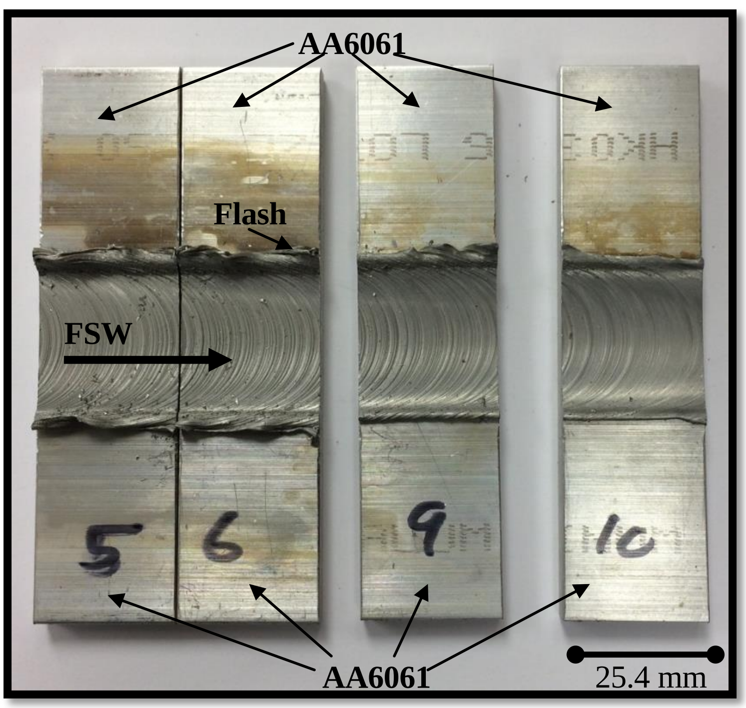

Figure 4: AA6061-AA6061 FSW test coupons before flash machined.

3.3 Atmospheric Corrosion Method

The test coupons were exposed for three different lengths of time to various atmospheric conditions to study the relationship between corrosion and tensile strength, microstructure, and environment. This section explains the conditions of the various test sites, the actual atmospheric data logged over the three exposure periods, and the procedure used to secure the coupons to the test rack.

3.3.1 Test Sites

Hawai'i, while small in landmass, possesses a wide range of micro-climates. This study capitalizes on this geological advantage by exposing the aluminum alloys at the following locations: Kilauea, Waipahu, Lyon Arboretum, Pyramid Rock, and Coconut Island.

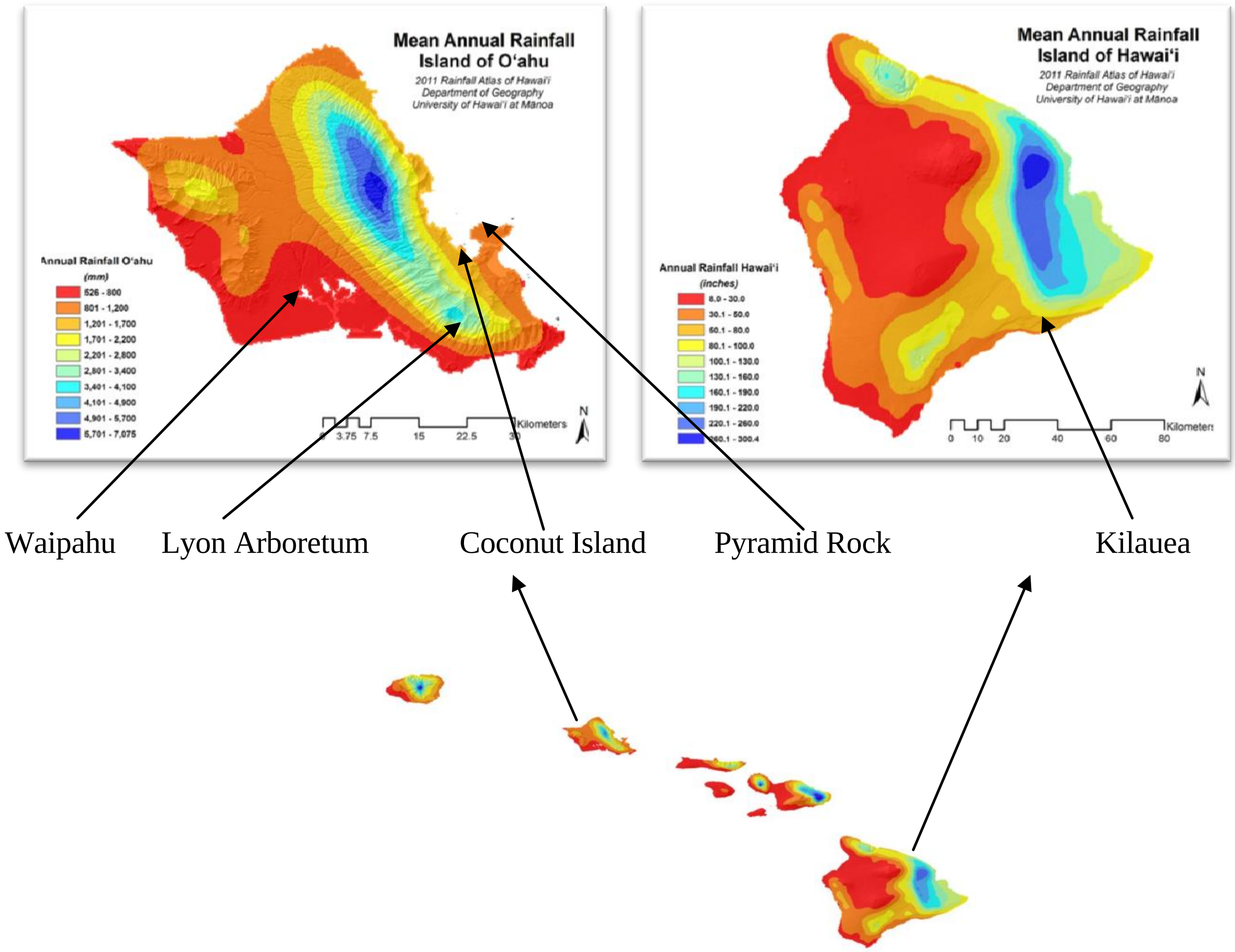

Figure 5: Five locations for atmospheric corrosion testing in Hawai'i. [29]

Kilauea replicates a high acidity environment due to its severe acid rain associated with volcanic activities. When sulfur dioxide (SO_2) gas is emitted by active volcano vents such as Pu'u O'o, it reacts with the water, oxygen, and sunlight in the air to form a mixture of sulfate (SO_4^{-2}) aerosols, sulfuric acid (H_2SO_4), and other oxidized sulfur species [30]. This is known as "vog", short for volcanic fog. The vog along with other characteristics of Kilauea makes it an interesting test sites to observe atmospheric corrosion, and relevant to corrosion in the Pacific Ring of Fire.

Waipahu represents an arid region located along the northern shore of Pearl Harbor. Once the location of a sugar plantation town, it is now considered a low-intensity developed area. The average annual air temperature, relative humidity, and solar radiation are 75° F, 0.7038, and 195.53 W/m^2, respectively [31].

Lyon Arboretum replicates a tropical rainforest environment. It is nestled atop the Manoa Valley watershed. With the average rainfall of 165 inches annually and with the average temperature of 78° F, this test location has been used extensively by the University of Hawai'i for research in tropical plants. Specifically, it is home to more than 5,000 taxa of tropical and sub-tropical plants [33].

Pyramid rock represents a marine environment in that it is a beach facing northwest to the Pacific Ocean. Here, the average annual air temperature, relative humidity, and precipitation are 74° F, 0.702, and 939.26 mm, respectively [31].

Coconut Island also replicates a marine environment; however, it is located inside Kaneohe bay. The prevalent NW trade-wind on Oahu is buffeted by the landmass where Marine Corp Base Hawaii (MCBH) resides. The surf here is relatively weaker than at Pyramid Rock due to, again, MCBH. Average annual atmospheric conditions here are similar to Pyramid Rock.

Coordinates and microclimate representation are shown in Table 2.

Table 2. Test Sites.

	Geographic Coordinates		**Microclimate Representation**
Test Sites	**Latitude**	**Longitude**	
Lyon Arboretum	21° 19′ 58″ N	157° 48′ 12″ W	Tropical Rainforest
Coconut Island	21° 26′ 09″ N	157° 47′ 15″ W	Marine (Mild)
Kilauea	22° 12′ 43″ N	159° 24′ 44″ W	Acidic (acid rain)
Waipahu	21° 42′ 00″ N	159° 24′ 44″ W	Arid
Pyramid Rock	21° 27′ 50″ N	157° 54′ 00″ W	Marine (Severe)

3.3.2 Recorded Test Sites Atmospheric Conditions

The weather along with atmospheric conditions at the test sites directly correlate to the corrosion behavior of the aluminum alloys. Thus, over thirty weather and atmospheric parameters were recorded bi-hourly such as ultraviolet rays (UV), leaf wetness, wind direction and speed, precipitation, relative humidity, and temperature by a Davis Vantage Pro® weather station. The average temperature, humidity, and rainfall are shown in Table 3; however, are public data from the University at Hawai'i at Manoa because some of the sensors malfunctioned during the experiment. The published data matches closely with the recorded data for times when the sensor did function.

Table 3. Annual Average Weather Data of Five Test Sites. [32]

Test Site	**Ave. Temperature (°C)**	**Ave. Humidity (%RH)**	**Ave. Rainfall (mm)**	**Cl^- Depos. ($mg/m^2/day$)**	**SO_4^{2-} Depos. ($mg/m^2/day$)**
Lyon Arboretum	21.8	74	3836.3	1.4	0.3
Coconut Island	23.5	70	1184.7	19.0	3.2
Kilauea	19.5	84.5	2158.4	15.1	13.6
Waipahu	23.7	70	578.5	7.5	2.9
Pyramid Rock	23.6	70	938.2	1879.8	266.9

3.3.3 Procedure

Using the Telesis Benchmark 320 making system, the coupons were stamped with alphanumerical codes such as AP501 for cataloging purposes. After the coupons were partitioned, the flash machined off, and the alphanumerical code stamped, they were cleaned with 18.1 MΩ water in the Fisher Scientific FS220H ultrasonic cleaning tub. Each combination of the FSW aluminum alloys had four test coupons. Thus, there were 12 coupons for the three combinations, AA6061-AA6061, AA5086-AA5086, and AA6061-AA5086. Another set was created in the shape of a dog-bone which would later be used for tensile testing. Altogether, 24 coupons were exposed at each site for each exposure period such that there were 72 coupons being exposed on day one. After six months, one year, and two years, a set of 24 coupons (i.e., 12 regular and 12 dog-bone) were taken back to the lab for analysis. An example of a typical layout and orientation for the exposed samples is shown in Figure 6.

Figure 6: Exposed Samples Layout and Orientation at Kilauea.

3.4 Weight Loss Method

After retrieving the test coupons from the sites after the pre-determined exposure period, the corrosion products were removed according to the International Standard Procedure ISO 8407:1991 (E) C.1.1. This cleaning procedure specifically targets aluminum and aluminum alloys. The cleaning solution was produced by adding 50 ml phosphoric acid (H_3PO_4, ρ= 1,69 g/ml) and 20 g of chromium trioxide (CrO_3) to distilled water to make a 1,000 ml solution. Effectively, the cleaning solution was 2% chromium trioxide and 5% phosphoric acid by weight. Next, the cleaning solution was heated to 90^{o} F and maintained at this temperature or above using the Jenway 1103 digital hotplate/stirrer fitted with a temperature probe. According to the standard, the test coupons could be immersed in the cleaning solution from five to ten minutes. The author chose ten minutes to reduce the iterations of cleaning. Next, the test coupons were rinsed and cleaned ultrasonically for 20 minutes in deionized water. The test coupons, lastly, were dried and weighed. The final weight in conjunction with the initial weight was used to calculate the mass loss of each coupon.

Equation 1. Corrosion Rate Equation

$$CR = \frac{(MI - MF)}{A \times D}$$

Where: $C.R. \cong Corrosion\ Rate; MI \ \cong Mass\ Initial; MF \ \cong Mass\ Final; A \ \cong Area;$

$$D \ \cong Days\ of\ Exposure$$

3.5 Tensile Characterization Method

To understand the tensile characteristics of the aluminum alloys before and after the corrosion, this study applied the uniaxial tensile test using an Instron-5500R testing machine. The dog-bone test coupons were machined from the weld whereby the FSW traversed the coupons normally.

Figure 8 below illustrates how a dog-bone coupon for FSW of AA606 and AA5086 was machined from the larger parent material. The samples had the same gauge length of 62.9 mm, same width of 12.8 mm, and varying thickness from 3.20 mm to 5.16 mm. Figure 7 below showed how the two points of interest, yield (0.2% offset) and ultimate strengths, were determined from the resulting stress-strain data generated by the Instron machine. This curve represents AA5086-AA5086 at Pyramid Rock exposed for two years.

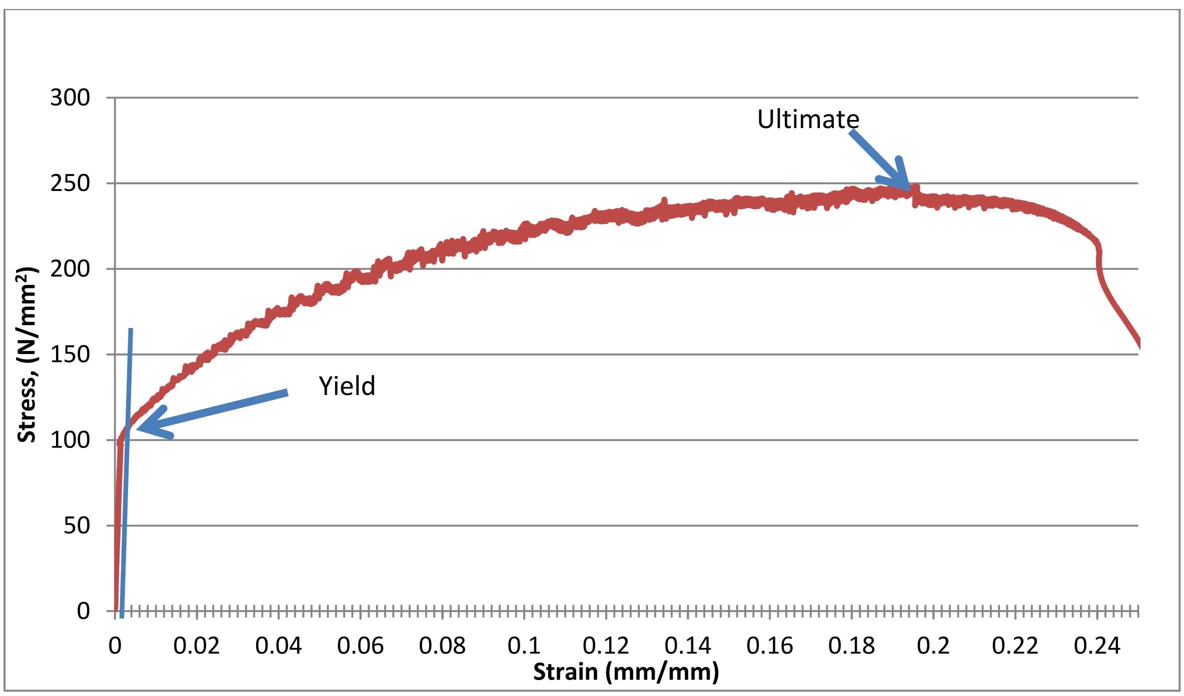

Figure 7: Locations of yield and ultimate strengths example (AA5086-AA5086 at Pyramid Rock for 2-year.

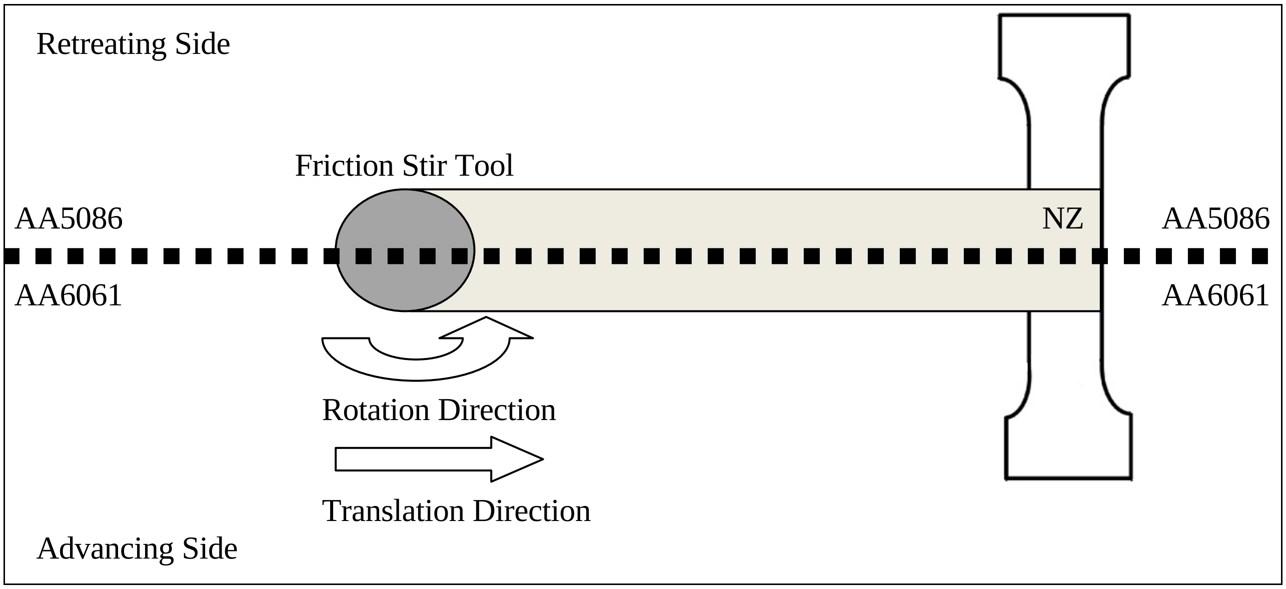

Figure 8: Orientation of dog-bone to FSW of AA6061-AA5086

To measure the elongation of the coupons, a 50.8 mm extensometer was attached to the gauge section. The tensile of the joints for the three different weld combinations were then analyzed by the ASME automatic strain measuring system. The crosshead speed of 3 mm/min was selected for the Instron machine. Percent elongation was calculated by the dividing the difference between the elongated length at rupture and original gauge length by the original gauge length, then multiplied by 100.

3.6 Microstructure Characterization Method

The AA6061-AA5086 FSW coupons were analyzed before and after the atmospheric corrosion exposures. In particular, the nugget zone, thermo-mechanically affected zone, heat affected zone, and base metal were analyzed for microstructural constituents and their influence on corrosion morphology. Microstructural analyses of the AA5085-AA5086 and AA6061-AA6061 were performed elsewhere [23] . The Scanning Electron Microscope (SEM)—Hitachi S-3400N SEM equipped with an Oxford Instrument energy dispersive X-Ray analyzer (EDXA)—was used to characterize the aluminum alloys. To characterize the alloys before corrosion, distinct BM, HAZ, TMAZ, and NZ regions were cut from a AA5086-AA6061 welded specimen and mounted in epoxy, Figure 9. The mounted specimens were subsequently ground with 320, 400, and 600 grit silicon carbide grinding paper, and then subsequently polished using 1, 0.3, and 0.025 μm diamond slurries. After polishing, the specimens were cleaned in the ultrasonic cleaner in ultrapure 18 MΩ•cm water for 30 minutes. The exposed coupons were analyzed as they were in the field, i.e., they were not sectioned and mounted in epoxy.

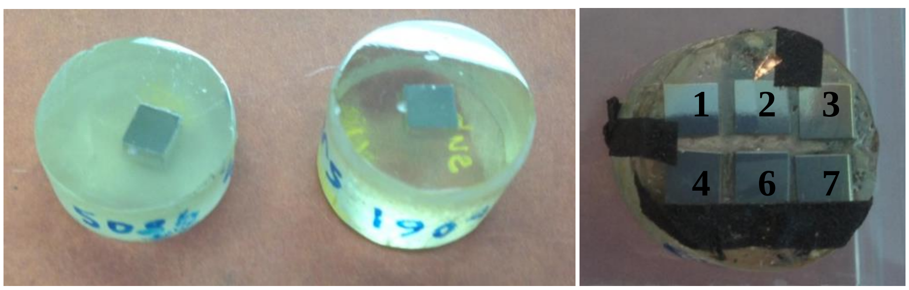

Figure 9: Unexposed BM of AA5086 (left), BM of AA6061 (center), NZ-up (right 1), NZ-down (right 2), HAZ AA5086 (right 3), HAZ AA6061 (right 4), TMAZ AA5086 (right 6), and TMAZ AA6061 (right 7).

A sample was then placed inside the SEM whereby the software interface was configured to 20 kV, and the samples were placed 10 mm from the scanning probe. Once the INCA software was calibrated to the standardized copper material, the samples were systematically imaged and the chemical compositions at various sites were calculated.

Chapter 4

RESULTS AND DISCUSSIONS

The results from the weight-loss test, tensile test, and microstructure analysis will be presented along with their discussion in the respective order.

4.1 Weight Loss

Altogether, there were 180 coupons used for this test. There were five sites being considered: Kilauea, Waipahu, Coconut Island, Pyramid Rock, and Lyon Arboretum. At each site, there were three types of FSW materials being analyzed: AA6061-AA6061, AA5086-AA5086, and AA6061-AA5086. There were four coupons created for each of the three materials. Only three of the four coupons underwent cleaning (135 coupons total) while the fourth one was reserved for microstructure and corrosion morphology analyses.

4.1.1 Results

The weight loss data of the 135 cleaned coupons were organized in three different configurations. The first configuration compares the weight loss of the three materials grouped by test site and exposure time (Figure 10).

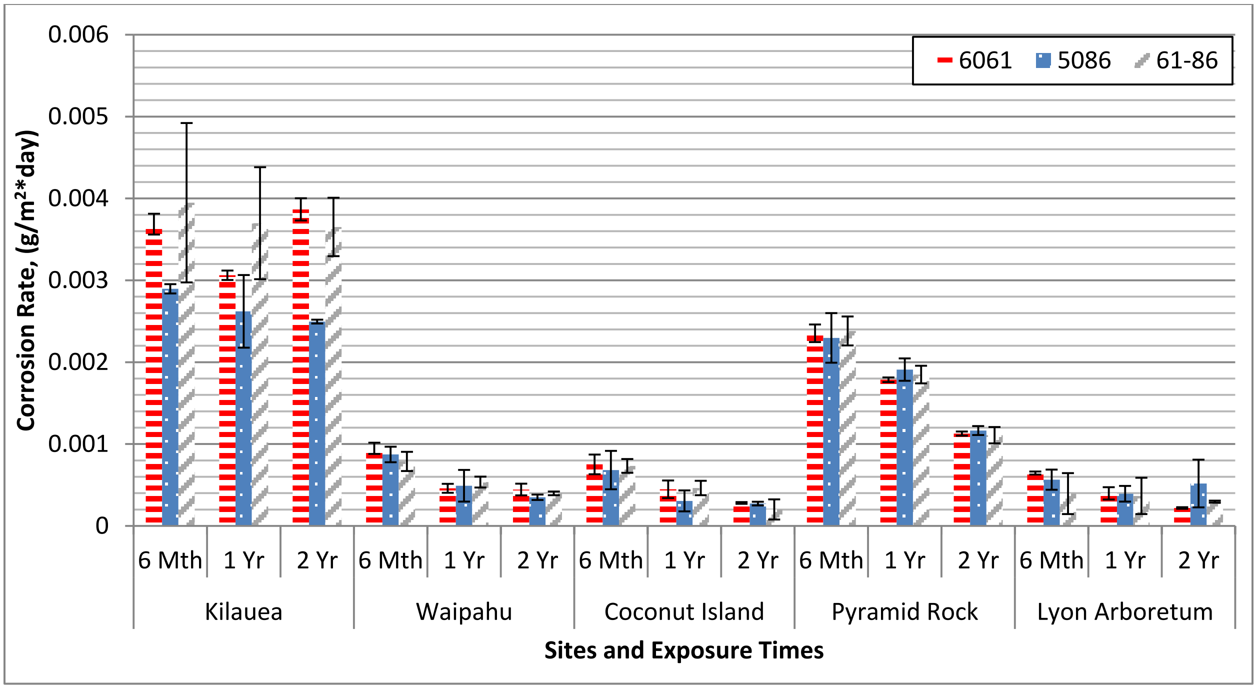

Figure 10: Comparison of corrosion rates for the three welded materials grouped by test site and exposure period. Abbreviations: 6061 – AA6061-AA6061 weld specimen; 5086 – AA5086-AA5086 weld specimen; 61-86 – AA6061-AA5086 weld specimen.

The second configuration compares the weight loss of the three time exposures grouped by test site and material type (Figure 11).

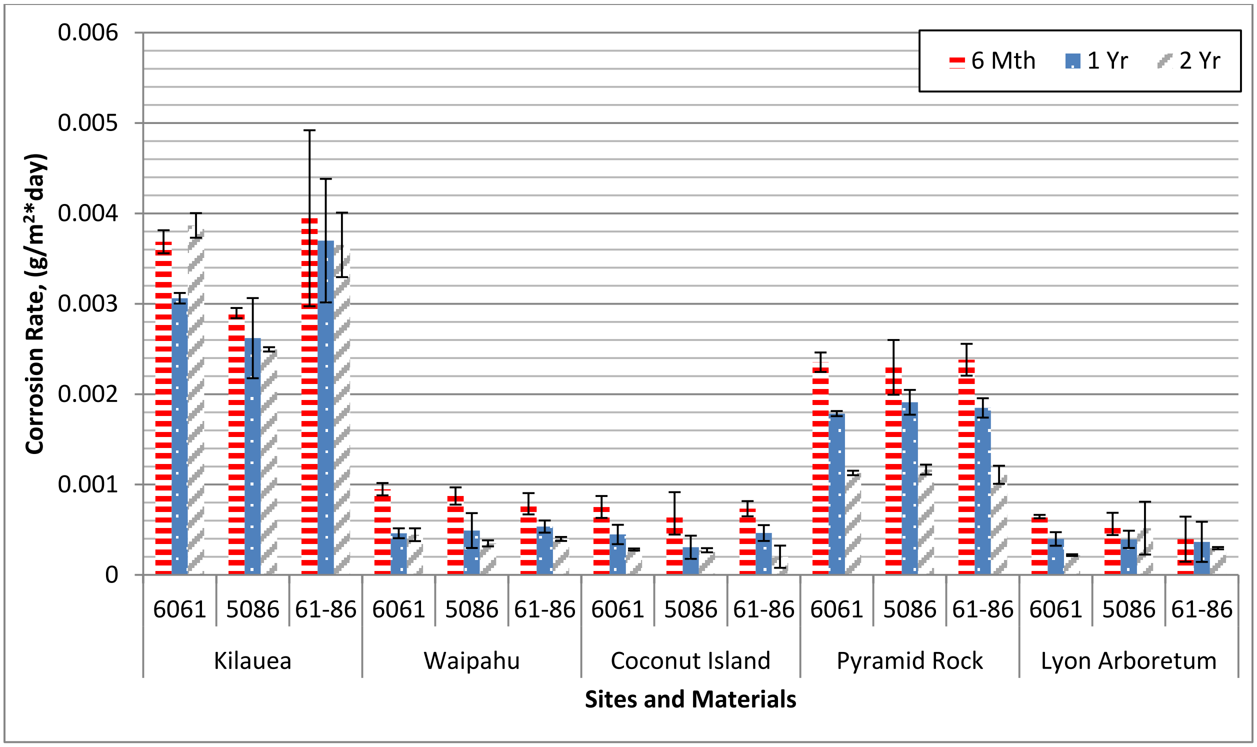

Figure 11: Comparison of corrosion rates for the three time exposures grouped by test site and material type. Abbreviations: 6061 – AA6061-AA6061 weld specimen; 5086 – AA5086-AA5086 weld specimen; 61-86 – AA6061-AA5086 weld specimen.

The third configuration compares the weight loss for various exposure times grouped by test site and material type (Figure 12).

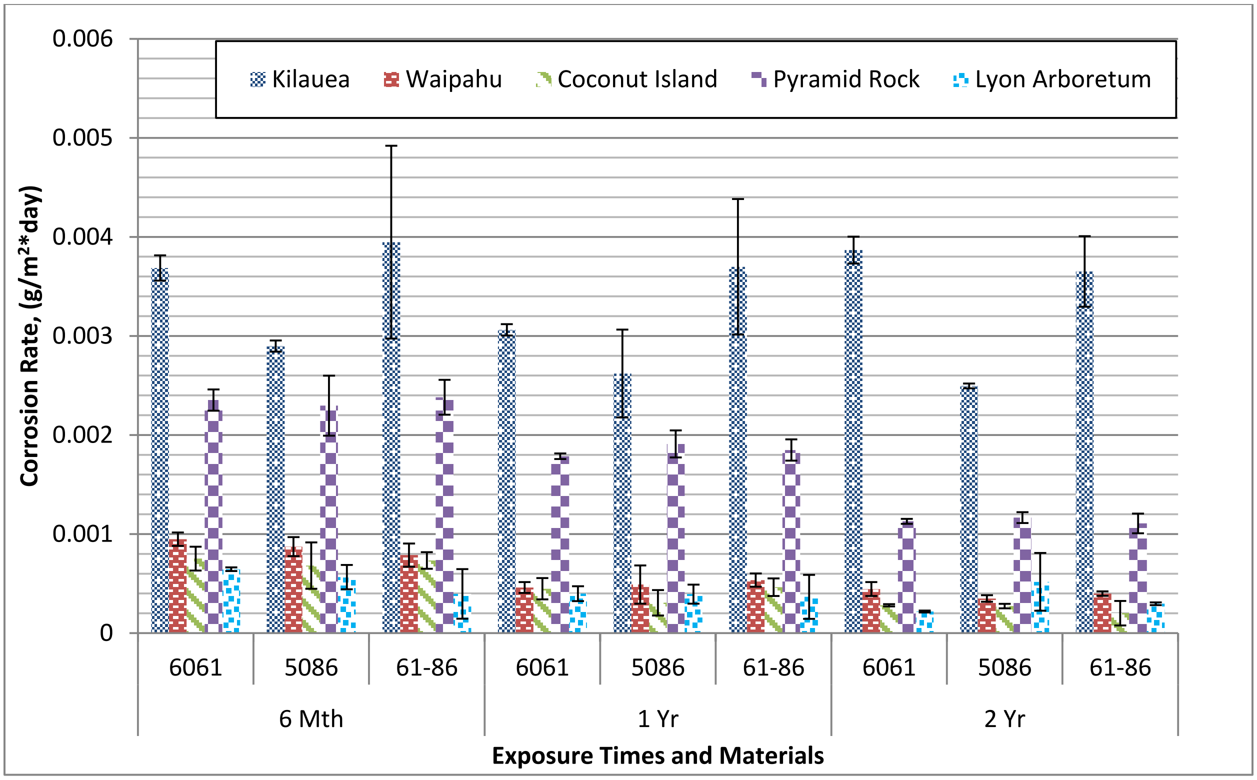

Figure 12: Comparison of corrosion rates for the five test sites grouped by the exposure time and material type. Abbreviations: 6061 – AA6061-AA6061 weld specimen; 5086 – AA5086-AA5086 weld specimen; 61-86 – AA6061-AA5086 weld specimen.

4.1.2 Discussion

The AA5086-AA5086 showed the best corrosion resistance of the three materials at Kilauea test site (acid rain) for the three exposure periods (Figure 10). At the Waipahu (arid), Lyon Arboretum (rainforest), Coconut Island (mild marine), and MCBH (severe marine) test sites, the AA5086-AA5086, AA6061-AA6061, and the AA6061-AA5086 had comparable corrosion rates that were generally within the upper and lower bounds set by standard deviation bars for each material (Figure 10).

Regarding exposure period, the corrosion rate consistently decreased with exposure time (Figure 11). The corrosion rates representing the 6 month exposure period (red with white dashes) was higher than those of the 1-year and 2-year exposure periods for all sites and materials except for one instance: AA6061-AA6061 at Kilauea. The 1-year exposure rates (blue with white dots) were lower than the 6-month rates for all sites and materials. This was the most consistent trend in Figure 11. The 2-year exposure rates (gray with white stripes) were lower than the 6-month and 1-year rates for all cases except for at Kilauea for AA6061-AA6061 and AA6061-AA5086 and at Lyon Arboretum for AA5086-AA5086. Nevertheless, the general trend was that the corrosion rates decrease as the time exposure increases.

The Kilauea test site with acid rain generated the highest corrosion rates (Figure 12) for all time exposures and materials with the highest overall corrosion rates at 0.003946$\frac{g}{m^2 * day}$. The second noticeable trend was that the severe marine test site at Pyramid Rock generated the next highest corrosion rates after Kilauea. The Waipahu (arid), Coconut Island (mild marine) and Lyon Arboretum (rain forest) sites had much lower rates. In many instances, the rates at the rain forest site were the lowest, which is likely related to the very low levels of chlorides.

4.2 Tensile Test

One hundred and eighty dog-bone tensile samples were recovered from the five test sites over the three exposure periods. One sample representing each combination of site, exposure time, and material was reserved for future studies while the other three underwent tensile testing. The result of the test, particularly the yield, ultimate, and strain to failure, is shown in this section.

4.2.1 Results

Generally, the AA5086-AA5086 exhibited the highest yield, ultimate, and strain to failure of the three materials. Figure 13 displays, as an example, the stress-strain curve for the three types of materials at Pyramid Rock exposed for two years. AP### represents AA6061-AA6061, BP### represents AA5086-AA5086, and CP### represents AA6061-AA5086. Each material had three replicas used to create averages and standard deviations. AA5086-AA5086 in Figure 13 clearly exhibits the highest ultimate strengths and strain to failure as indicated by the pink, green, and navy blue lines.

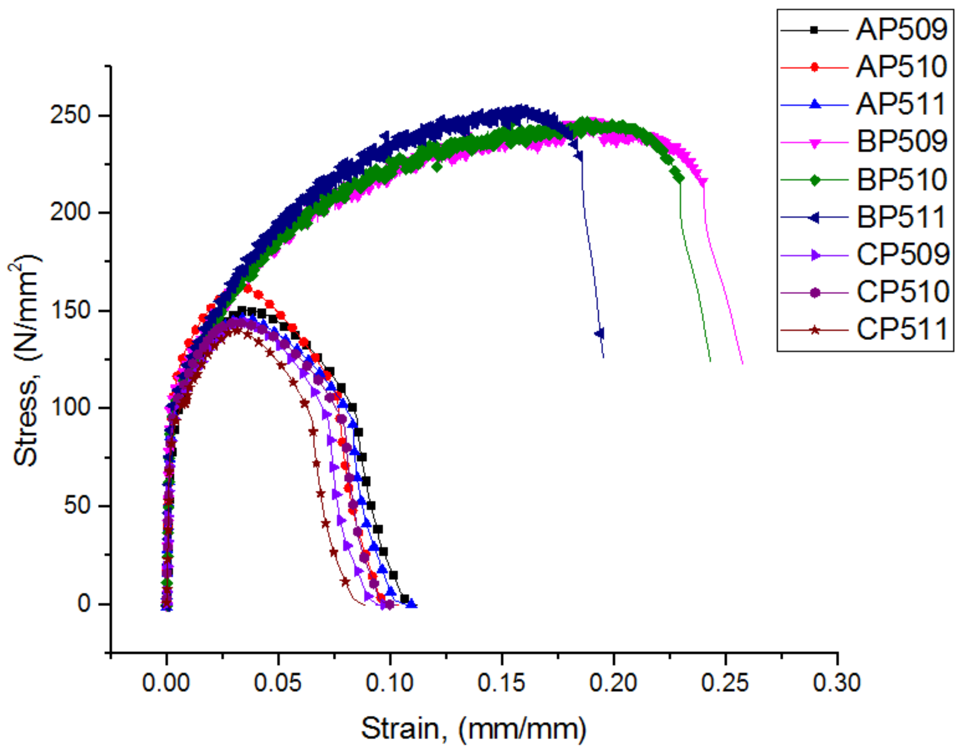

Figure 13: Stress-strain curves for the three materials at Kilauea for two years (AP### is AA6061-AA6061, BP### is AA5086-AA5086 and CP### is AA6061-5086).

To better show the data above by reducing the number of curves shown, the average curve of the three replicas for each material was graphed in Figure 14. Again, the UTS and strain to failure of AA5086-AA5086 were superior to the other two weld types. It is interesting to see that the average yield, ultimate, and fracture strengths of AA6061-AA5086 welds were all lower than the two parent materials.

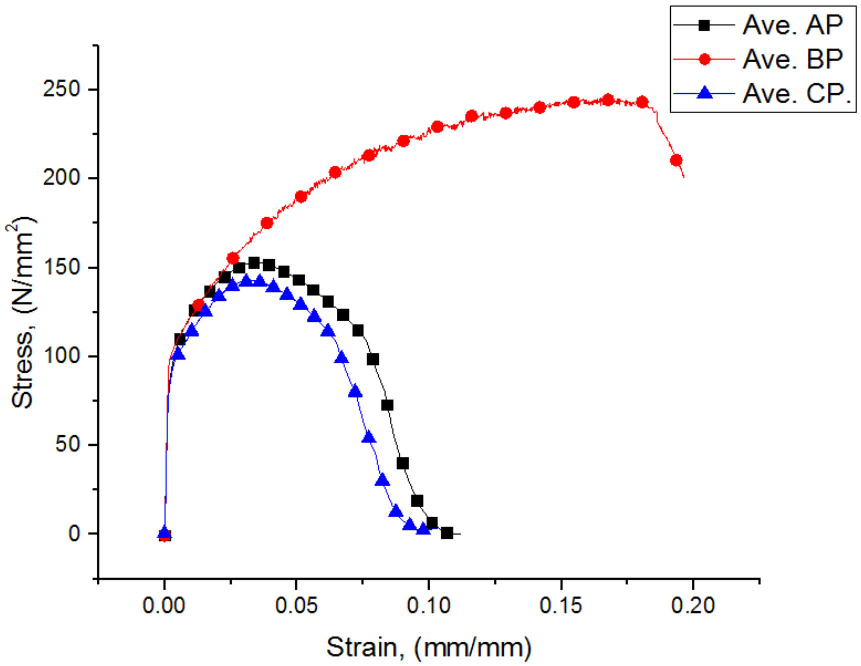

Figure 14: Average stress-strain curves for the three materials at Pyramid Rock for two years (AP is AA6061-AA6061, BP is AA5086-AA5086, and CP is AA6061-AA5086).

Incorporating the average stress-strain curves of all sites, materials, and exposure periods would be too dense in a single plot. Rather, only the three important properties of interest were recorded and compared. Figure 15, Figure 16, and Figure 17 analyze the yield strength; Figure 18, Figure 19, and Figure 20 analyze the ultimate strength; and Figure 21, Figure 22, and Figure 23 analyze the strain to failure. At each of the three items of interest, the data was organized to show trends over time, between materials, and between test sites.

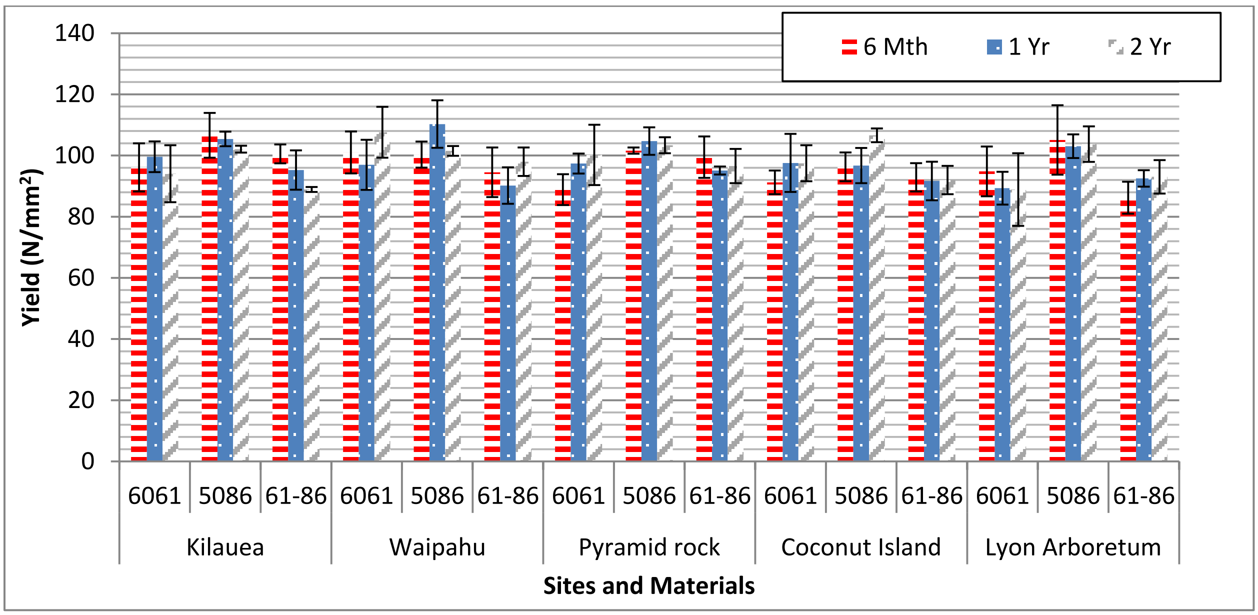

Figure 15: Yield strength. Comparison of exposure times grouped by test site and material type. Abbreviations: 6061 – AA6061-AA6061 weld specimen; 5086 – AA5086-AA5086 weld specimen; 61-86 – AA6061-AA5086 weld specimen.

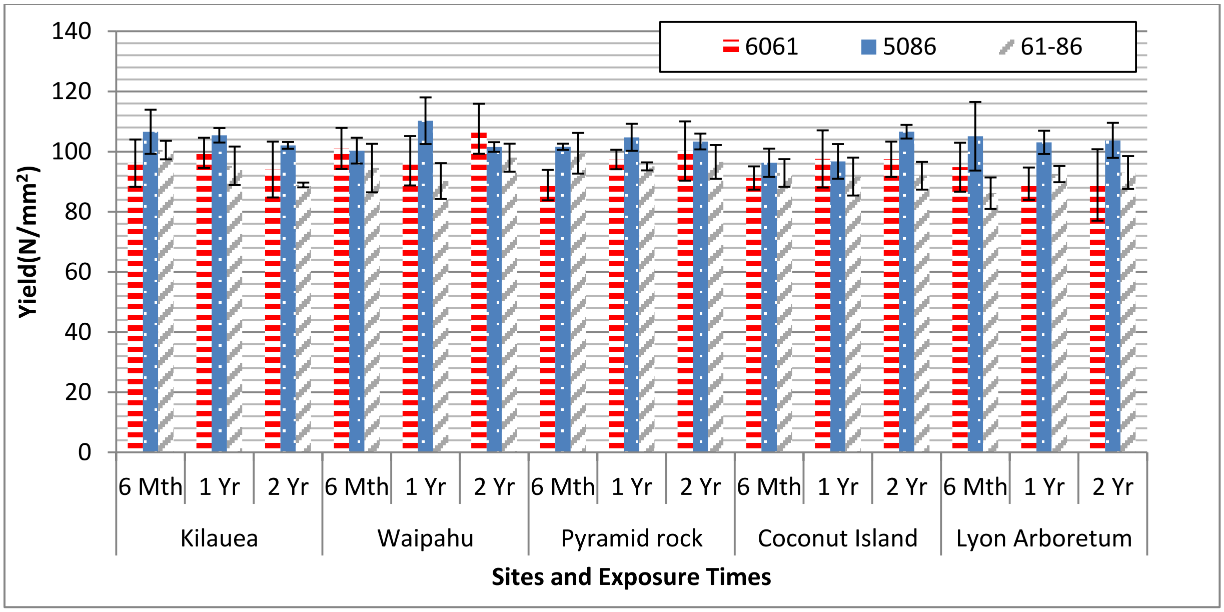

Figure 16: Yield strength. Comparison of material type grouped by test site and exposure time. Abbreviations: 6061 – AA6061-AA6061 weld specimen; 5086 – AA5086-AA5086 weld specimen; 61-86 – AA6061-AA5086 weld specimen.

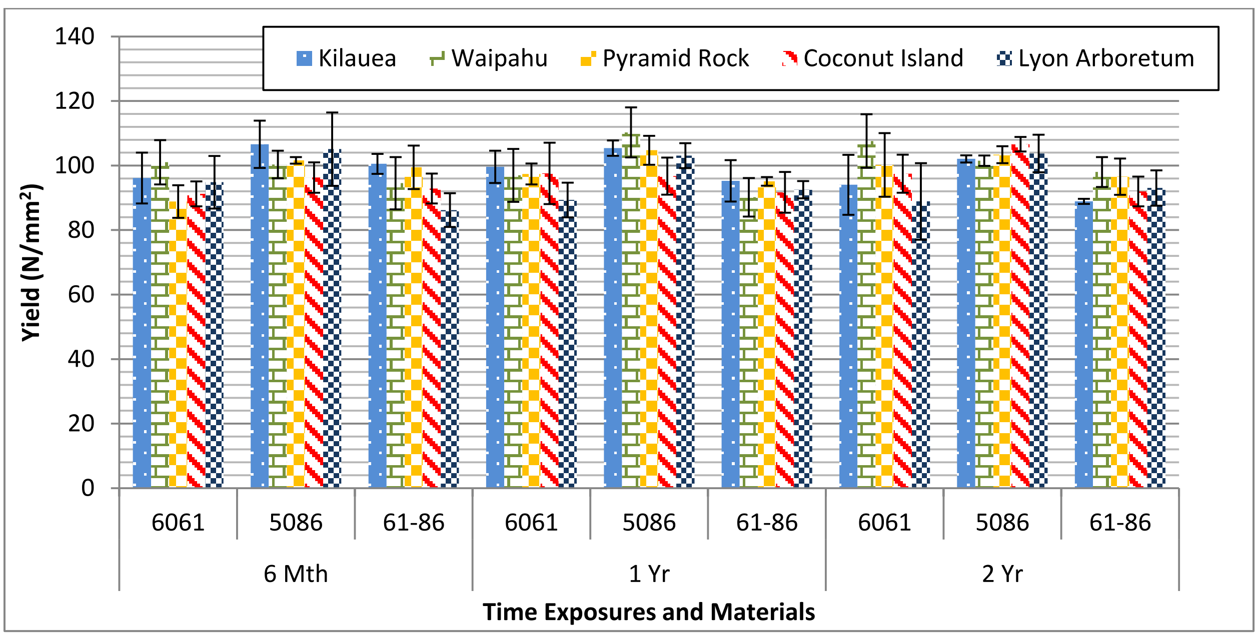

Figure 17: Yield strength. Comparison of test sites grouped by exposure time and material type. Abbreviations: 6061 – AA6061-AA6061 weld specimen; 5086 – AA5086-AA5086 weld specimen; 61-86 – AA6061-AA5086 weld specimen.

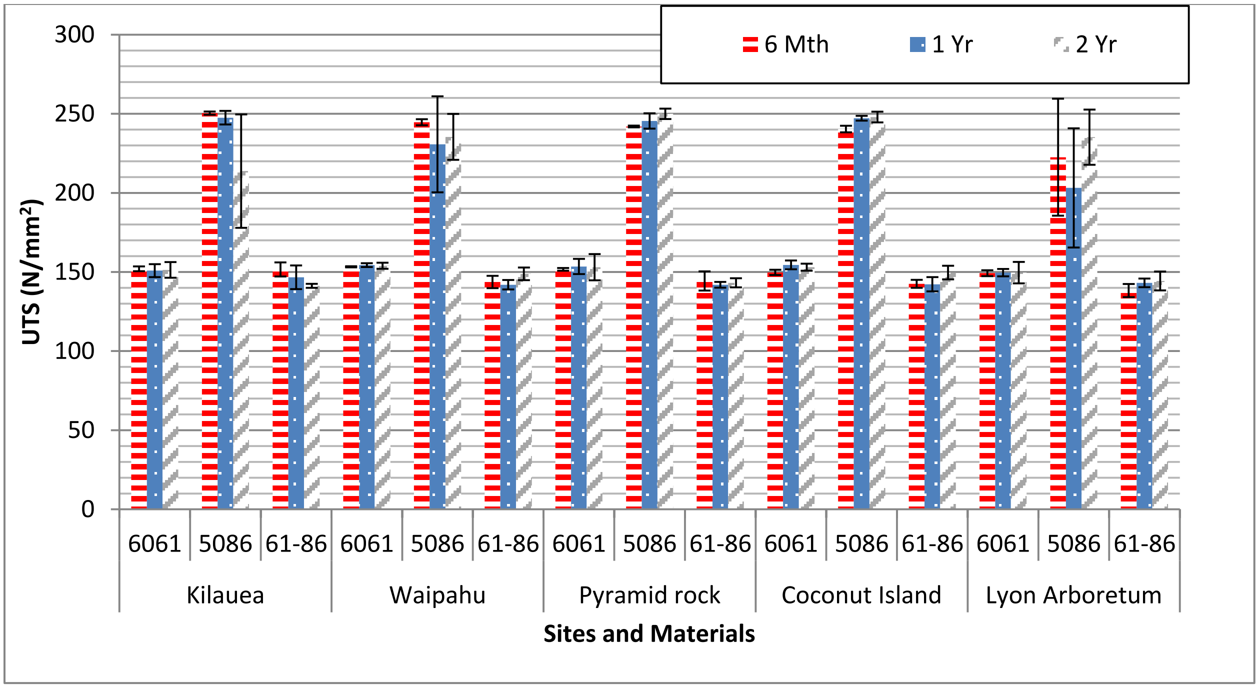

Figure 18: UTS. Comparison of exposure times grouped by test site and material type. Abbreviations: 6061 – AA6061-AA6061 weld specimen; 5086 – AA5086-AA5086 weld specimen; 61-86 – AA6061-AA5086 weld specimen.

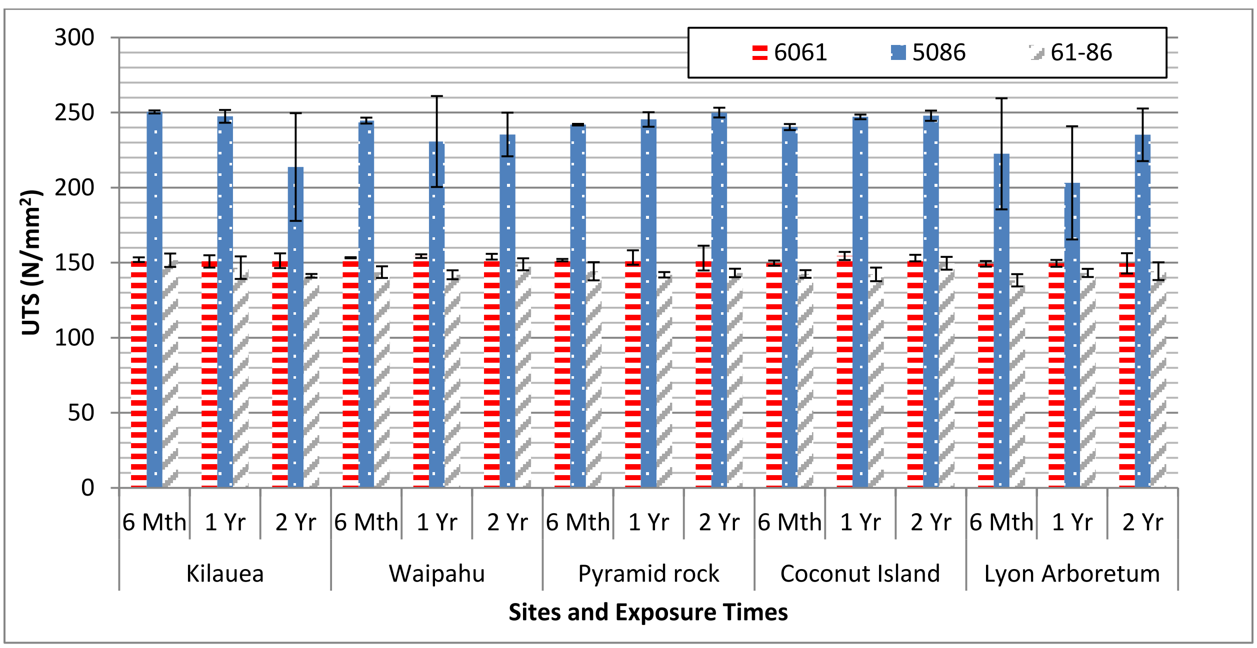

Figure 19: UTS. Comparison of material type grouped by test site and exposure time. Abbreviations: 6061 – AA6061-AA6061 weld specimen; 5086 – AA5086-AA5086 weld specimen; 61-86 – AA6061-AA5086 weld specimen.

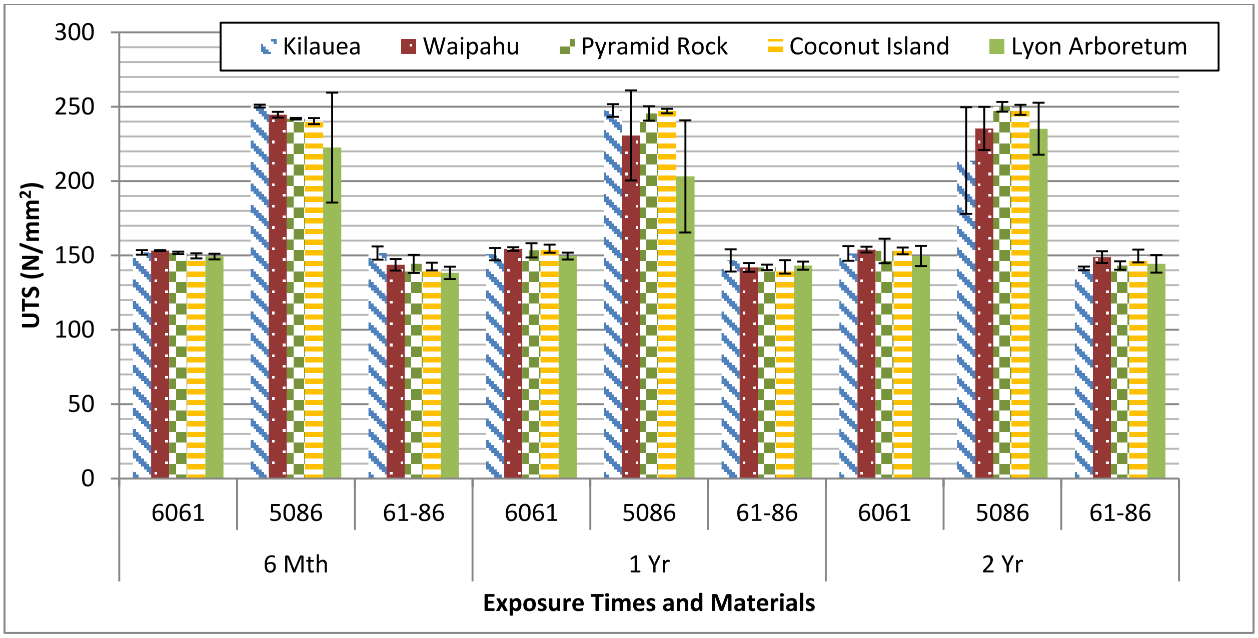

Figure 20: UTS. Comparison of test sites grouped by exposure time and material type. Abbreviations: 6061 – AA6061-AA6061 weld specimen; 5086 – AA5086-AA5086 weld specimen; 61-86 – AA6061-AA5086 weld specimen.

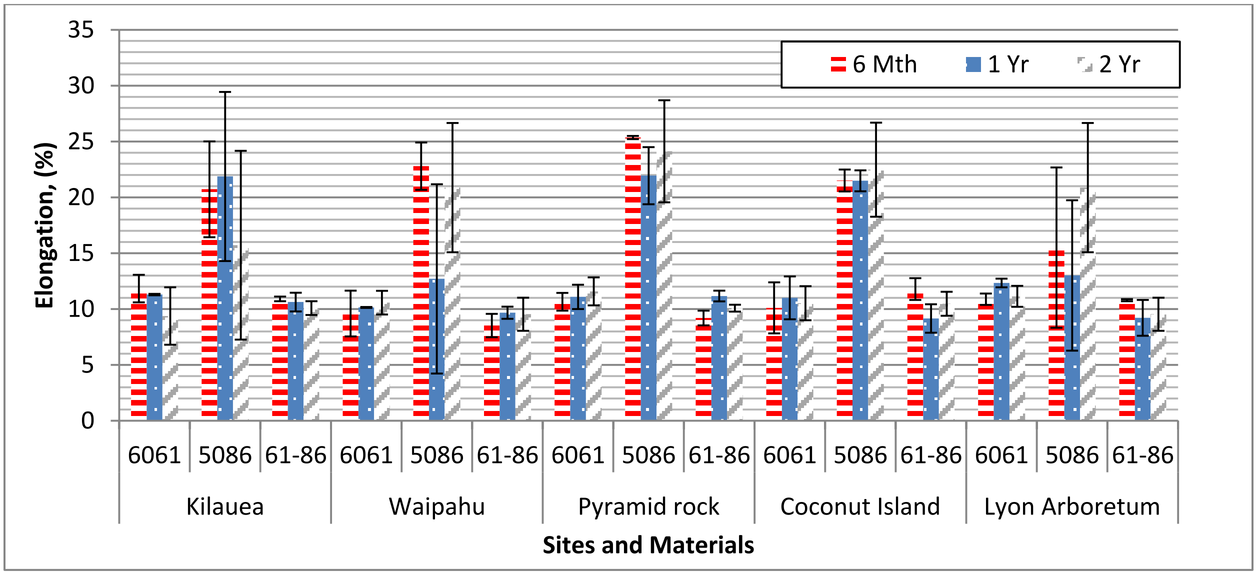

Figure 21: Strain to failure. Comparison of exposure times grouped by test site and material type. Abbreviations: 6061 – AA6061-AA6061 weld specimen; 5086 – AA5086-AA5086 weld specimen; 61-86 – AA6061-AA5086 weld specimen.

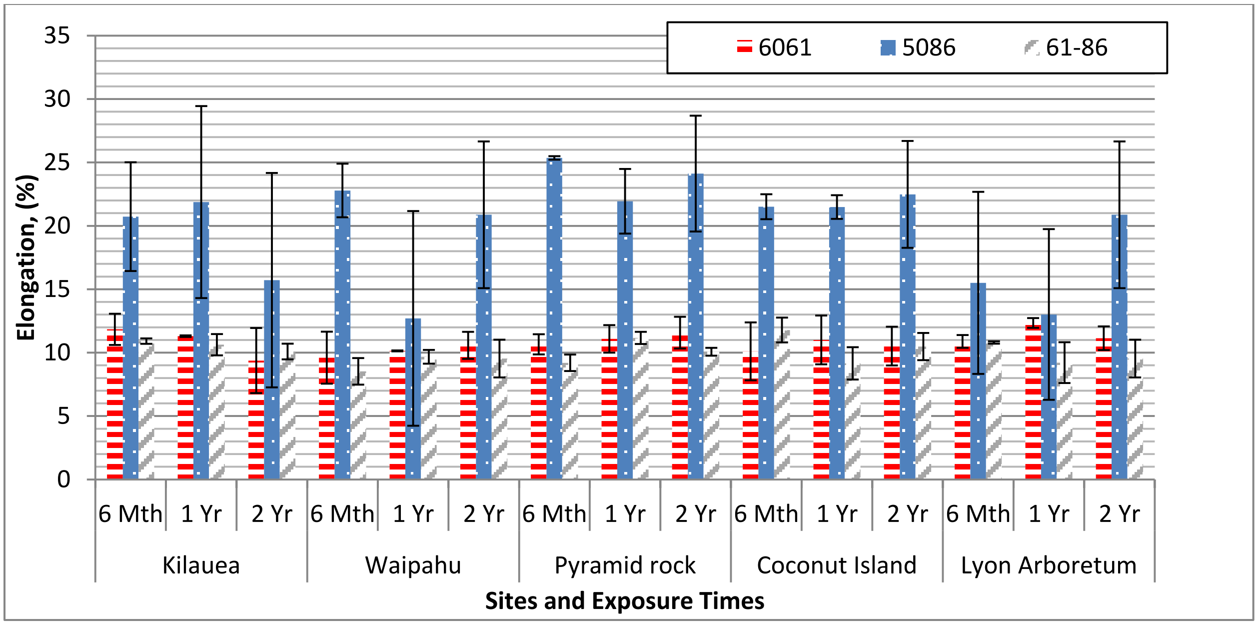

Figure 22: Strain to failure. Comparison of material type grouped by test site and exposure time. Abbreviations: 6061 – AA6061-AA6061 weld specimen; 5086 – AA5086-AA5086 weld specimen; 61-86 – AA6061-AA5086 weld specimen.

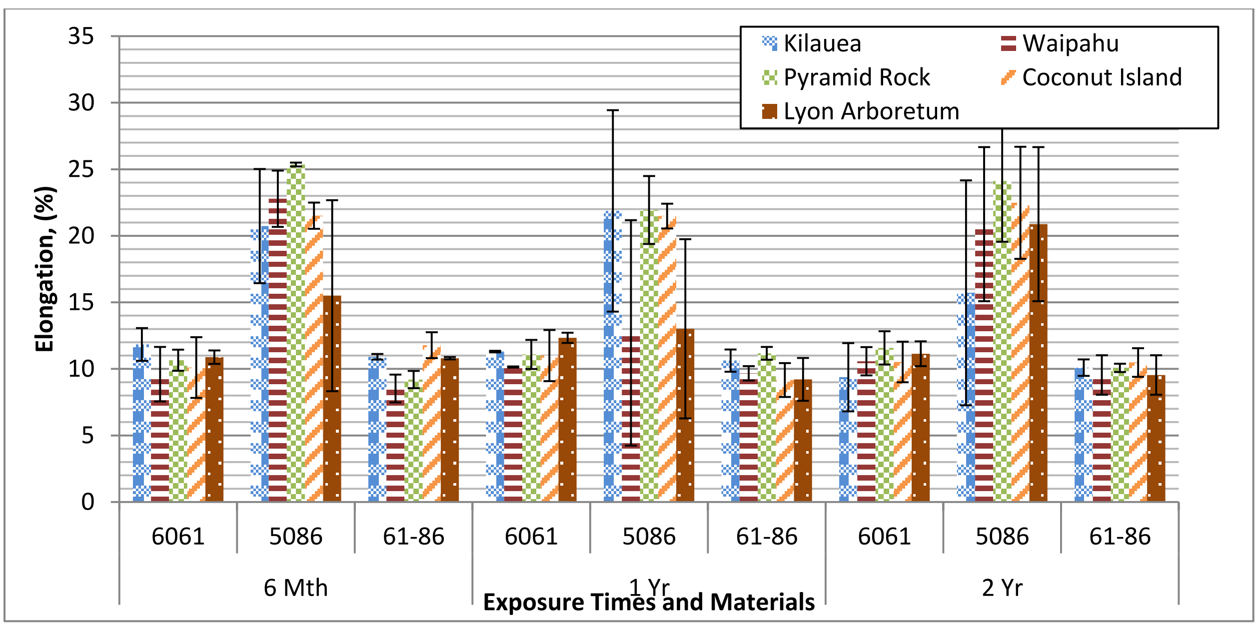

Figure 23: Strain to failure. Comparison of test sites grouped by exposure time and material type. Abbreviations: 6061 – AA6061-AA6061 weld specimen; 5086 – AA5086-AA5086 weld specimen; 61-86 – AA6061-AA5086 weld specimen.

4.2.2 Discussion

For the AA5086-AA5086, AA6061-AA6061, and the AA6061-AA5086 welded specimens, there were no consistent changes in the gaining or losing of yield strength based on exposure time or test site location (Figures 15, 16, and 17). The slight variations in yield strength were likely due to slight variations in the weld properties. Comparison between weld types showed that the AA5086-AA5086 had the highest yield strength by a small margin, and the AA6061-AA6061 and the AA6061-AA5086 had similar yield strengths. The lack of significant decreases in the yield strength is not unexpected since the corrosion damage of the specimens was relatively low, rendering any decrease in cross-sectional areas of the specimens to be minimal.

For the AA6061-AA6061 and the AA6061-AA5086 welded specimens, the ultimate tensile strength (UTS) did not change significantly over time. Figure 20 shows that both type of welds retained the same UTS at the five different test sites. The AA6061-AA6061 welds had an average UTS of approximately 151.99 $\frac{\mathrm{N}}{\mathrm{mm}^2}$ with a standard deviation (SD) of 1.84 $\frac{\mathrm{N}}{\mathrm{mm}^2}$; whereas, the AA6061-AA5086 welds had an average UTS of approximately 144.25$\frac{\mathrm{N}}{\mathrm{mm}^2}$ with a standard deviation (SD) of 3.54 $\frac{\mathrm{N}}{\mathrm{mm}^2}$. The AA5086-AA5086 welds had an average UTS of 237.08 $\frac{\mathrm{N}}{\mathrm{mm}^2}$ with a standard deviation of 14.11 $\frac{\mathrm{N}}{\mathrm{mm}^2}$. The AA6061-AA5086 welds always fractured on the weaker AA6061 side. The slight degradation of UTS of the AA6061-AA5086 welds compared to that of the AA6061-AA6061 welds may indicate that the mixing of the AA6061 and AA5086 alloys during FSW had a slight deleterious effect. The AA5086-AA5086 welds generally had a much higher UTS ($\approx 237 \frac{\mathrm{N}}{\mathrm{mm}^2}$) compared to the AA6061-AA6061 and the AA6061-AA5086 welds; however, large degradations appeared at the Kilauea, Waipahu, and Lyon Arboretum

(Figures 18, 19, and 20) test sites. Degradation of the UTS was observed at Kilauea for the 2-year exposure, at Waipahu for the 1-year and 2-year exposures, and at Lyon Arboretum at the 6-month, 1-year, and 2-year exposures. These degradations possibly could be due to sensitization of 5000-series aluminum alloys; where Mg migrates to grain boundaries and cause cracking.

Because the AA5086-AA5086 welds showed the highest degradation in UTS, the fracture surfaces of the welds were investigated. In two of the three AA5086-AA5086 test coupons exposed at Kilauea for two years, there seemed to be no sign of necking (Figure 24). This suggests that some of the AA5086-AA5086 specimens experienced premature fracturing before being fully elongated. The samples that did not neck exhibited lower UTS than the samples that did. For example, BK509 and BK510 (did not neck) had UTS of 176.18 and 217.47$\frac{\mathrm{N}}{\mathrm{mm}^2}$, respectively, while BK511 (necked) has UTS of 247.65 $\frac{\mathrm{N}}{\mathrm{mm}^2}$ (Figure 24). This characteristic was also observed in some of the specimens at Waipahu for the 1-year (Figure 25) and 2-year exposures, and at Lyon Arboretum for the 6-month (Figure 26), 1-year (Figure 27), and 2-year exposures.

For AA5086-AA5086 samples that underwent full elongation, the microstructure of the fracture surface was very fine while that of the premature fracture surface was course and with large cavities. Another interesting point is that the fracture surface of fully elongated samples had the same color while that of the pre-mature fracture samples had zones of different colors, particularly dark grey (Figure 27).

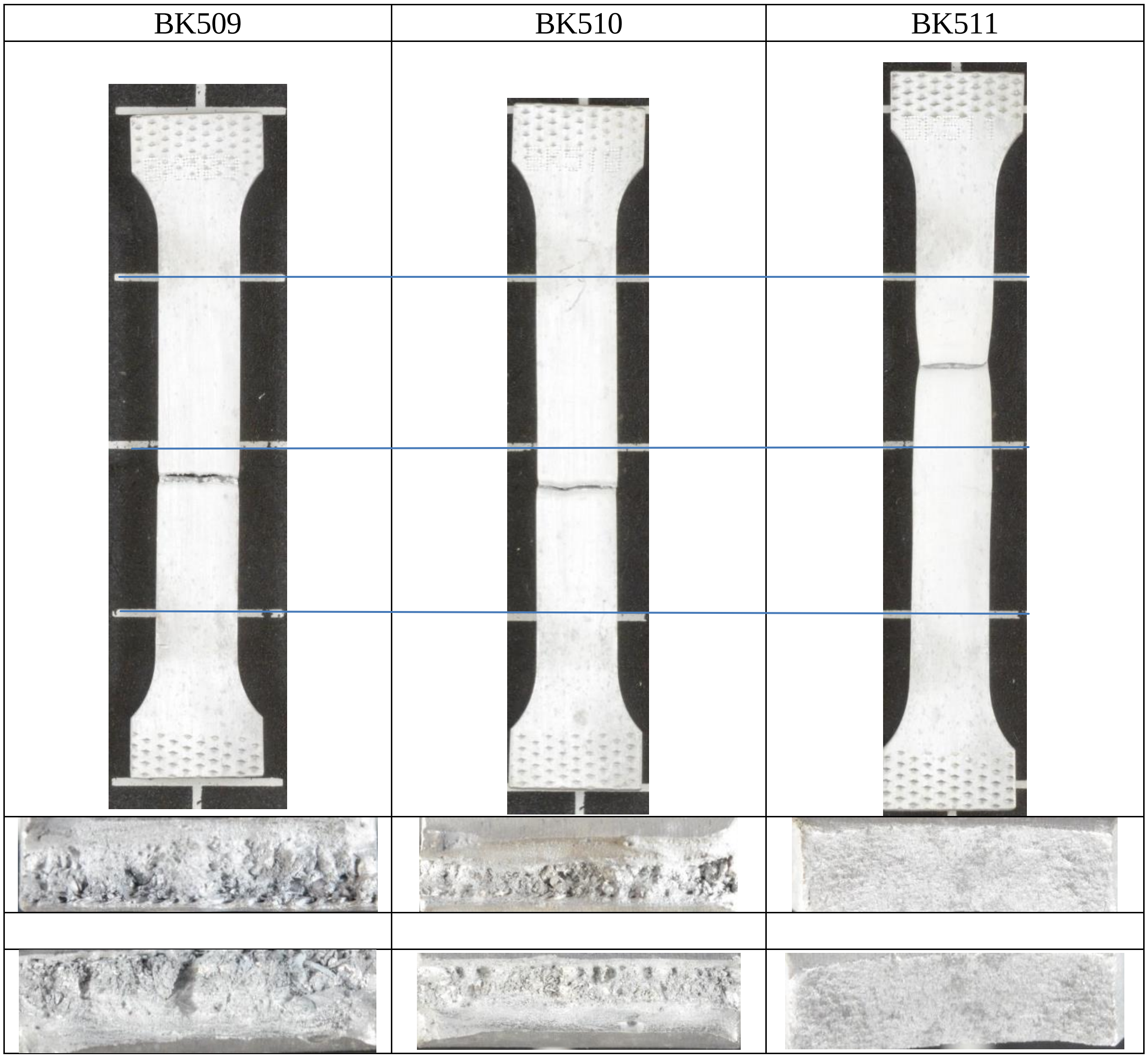

Figure 24: Fracture surface of AA5086-AA5086 welds at Kilauea for 2-year exposure.

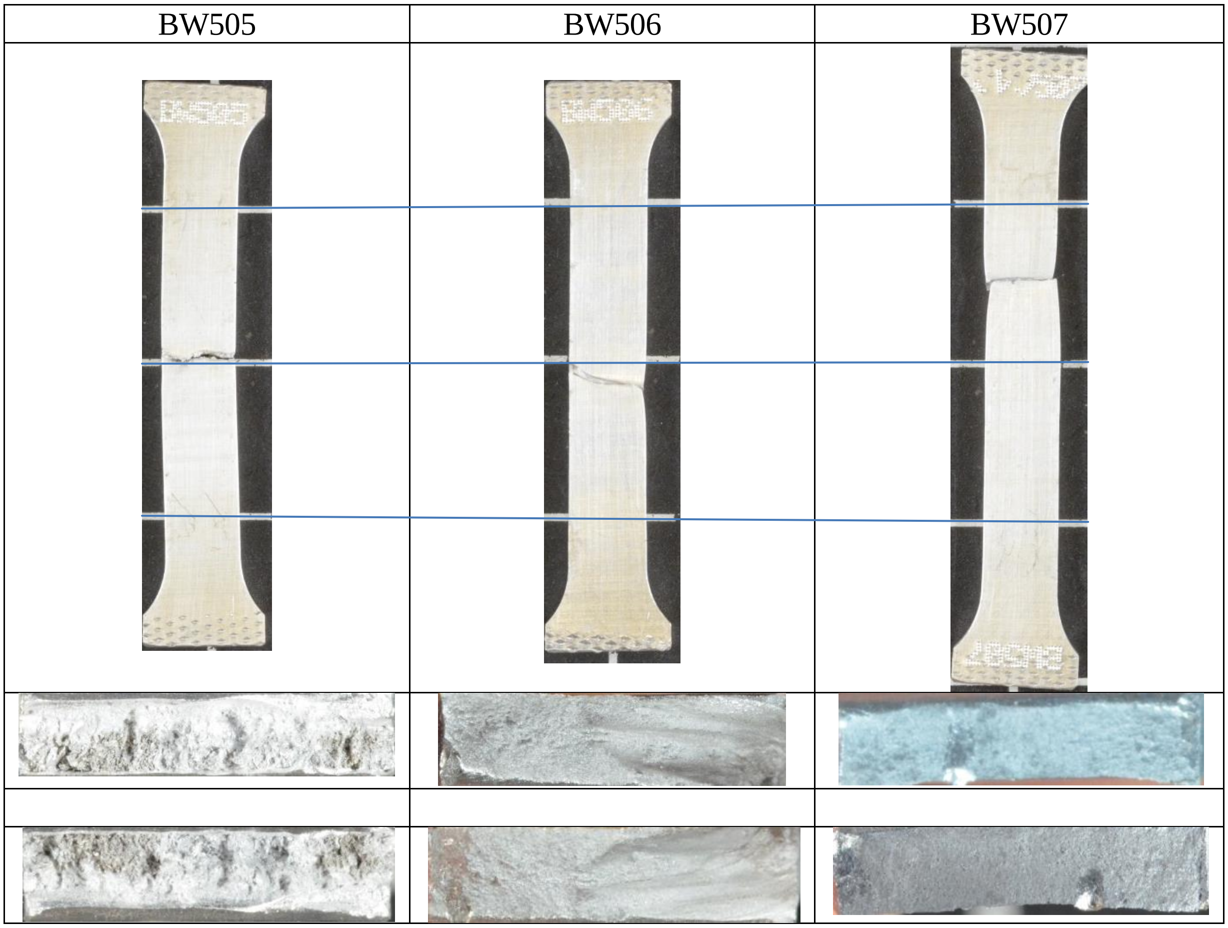

Figure 25: Fracture surface of AA5086-AA5086 welds at Waipahu for 1-year exposure.

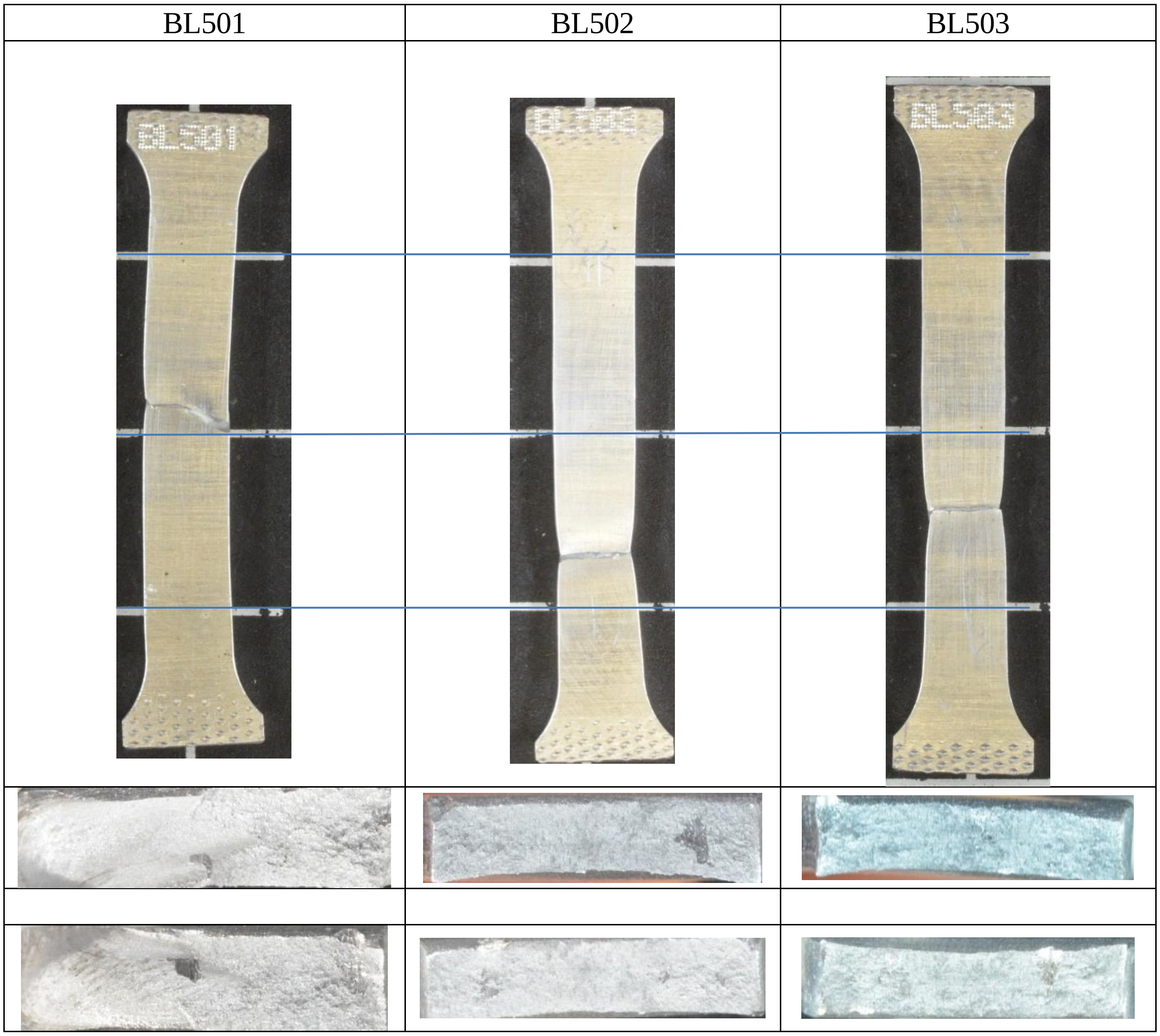

Figure 26: Fracture surface of AA5086-AA5086 welds at Lyon Arboretum 6-month exposure.

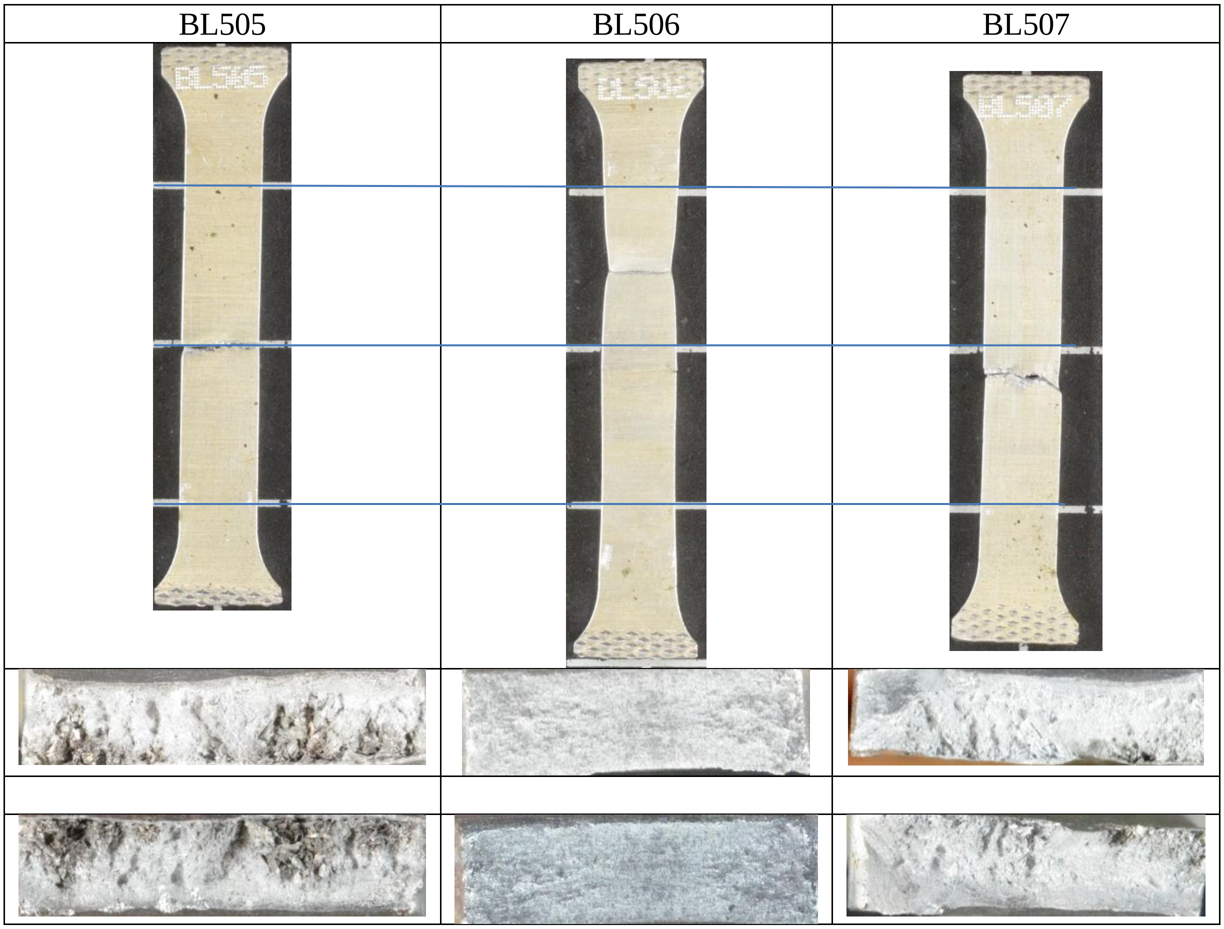

Figure 27: Fracture surface of AA5086-AA5086 welds at Lyon Arboretum 1-year exposure.

The most ductile or highest elongation to failure corresponded to the AA5086-AA5086 welds (Figure 21). At all test sites and time exposures, AA5086-AA5086 exhibited the highest elongation to failure and variability of the three materials. The variation in elongation to failure (Figures 21 to 23) for the AA5086-AA5086 welds seemed to generally be an amplification of the variations seen in UTS (Figures 18 to 20). In general, AA6061-AA5086 had similar elongation percentage as AA6061-AA6061 with the latter having slightly higher ductility in 11 out of 15 cases (Figure 22). The variations in the strain to failure for the AA6061-AA6061 and AA6061-AA5086 welds were significantly less than that of the AA5086-AA5086 welds. When comparing the ductility of the materials across the five test sites, it appeared that AA5086-AA5086 had the highest elongation to failure with the least variation at Pyramid Rock and at Coconut Island. Currently, it is not known if the variation in elongation to failure is related to the surface temperature of the specimens, which could influence the sensitization of the AA5086-AA5086 welds.

4.3 Microstructure

4.3.1 Results

The corrosion products on the various test coupons at the five test sites were analyzed with the Hitachi S-3400N SEM equipped with Oxford Instruments Energy Dispersive Z-Ray Analyzer (EDXA) system. First, an analysis on an unexposed sample of AA6061-AA5086 will be presented to establish a benchmark to evaluate the exposed samples. To be concise, only samples from the top three most corrosive sites were included in this study: Kilauea, Pyramid rock, and Lyon Arboretum. The tables and figures in Section 4.3.1.2 show the surface corrosion products on the alloys at 50X and 500X magnification and the chemical composition of each zone for each test coupons.

4.3.1.1 Unexposed AA6061-AA5086

Table 4 below shows the unexposed AA6061 and AA5086 parent materials of the AA6061-AA5086 dissimilar weld at two magnifications, and Table 5 displays the chemical composition of the two parent materials relative to the published standards.

Table 4. Parent Material. (EDXA region in red)

AA5086 (500X)

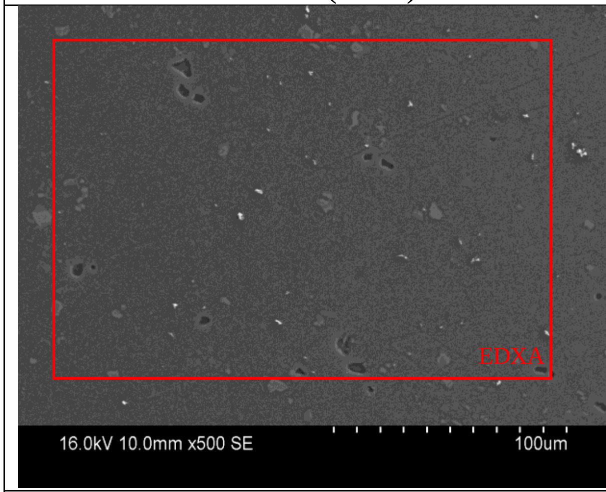

AA6061(500X)

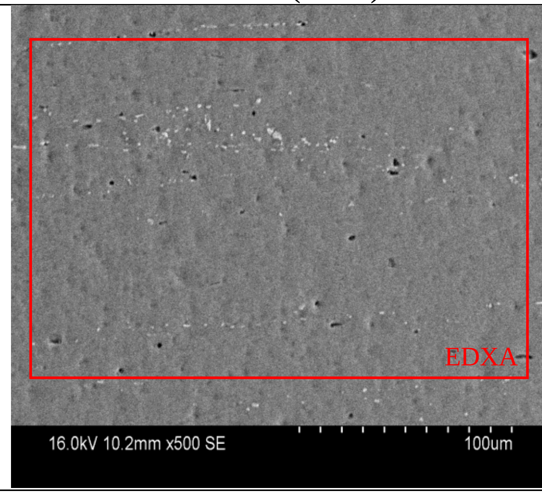

AA5086 (3,000X)

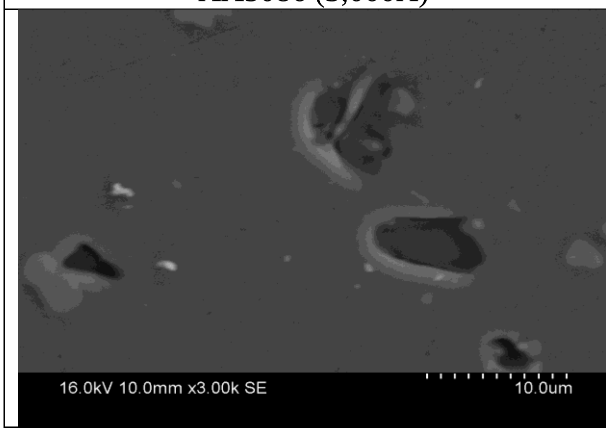

AA6061(3,000X)

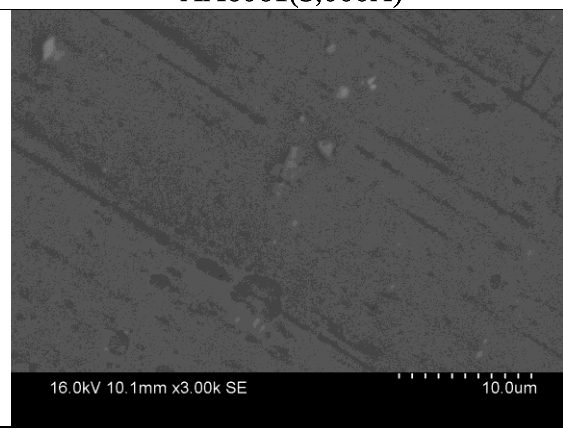

Table 5. EDX Analysis of Parent Metal compared to ASTM Standard.[34]

Alloy	**Al**	**O**	**Si**	**Fe**	**Cu**	**Mn**	**Mg**	**Cr**	**Ti**	**Zn**	**others**
6061 (base)	96.64	1.42	0.54	-	0.62	-	0.79	-	-	-	
6061-T6 (Literature)[1]	95 - 98.6	-	0.4 – 0.8	0.7 max	0.15 – 0.4	0.15 max	0.8 - 1.2	0.04 – 0.35	0.15 max	0.25 max	0.15 max
5086 (base)	94.33	1.16	-	-	-	0.47	4.04	-	-	-	
5086 (Literature)[2]	balance	-	0.4 max	0.5 max	0.1 max	0.2 – 0.7	3.5 – 4.5	0.05 - 0.25	0.15 max	0.25 max	0.15 max

Table 6 below shows the results of the SEM/EDXA of the HAZ on the AA5086 side of the dissimilar weld at two magnifications. Likewise,

Overview (210 X)	Coarse (1.2K X)

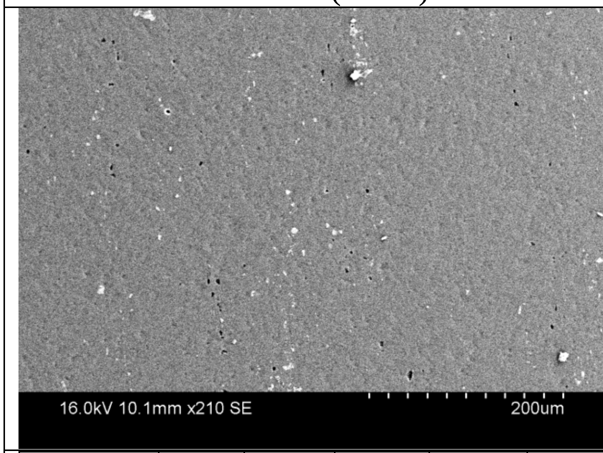

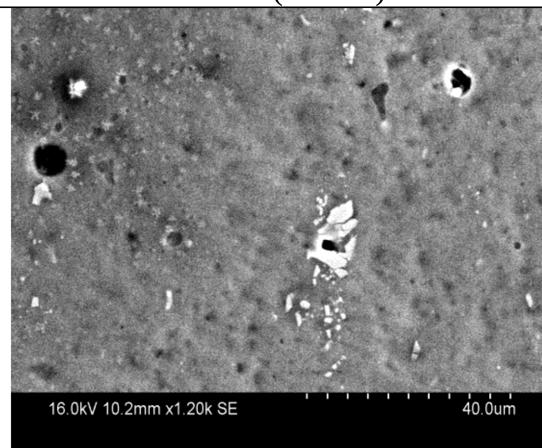

Al	**O**	**Si**	**Fe**	**Cu**	**Mn**	**Mg**	**Cr**	Ti	Zn	others
95.46	-	-	-	-	-	4.54	-	-	-	-

Table 7 shows the results for the HAZ on the AA6061 side.

Table 6. HAZ of AA5086 Side.

Overview (210 X)	Coarse (1.2K X)

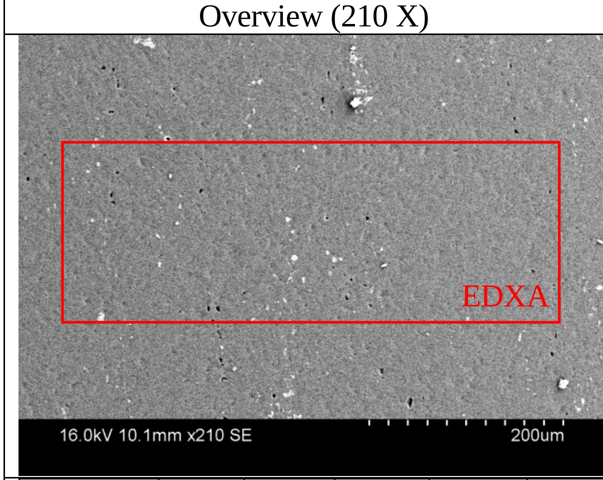

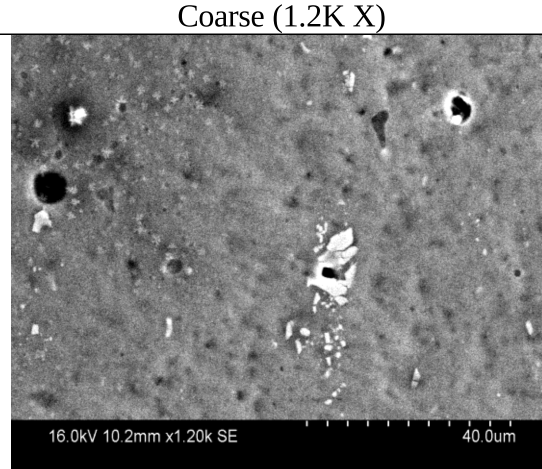

Al	**O**	**Si**	**Fe**	**Cu**	**Mn**	**Mg**	**Cr**	Ti	Zn	others
95.46	-	-	-	-	-	4.54	-	-	-	-

Table 7. HAZ of AA6061 Side.

Overview (400X)	Course (2,000X)
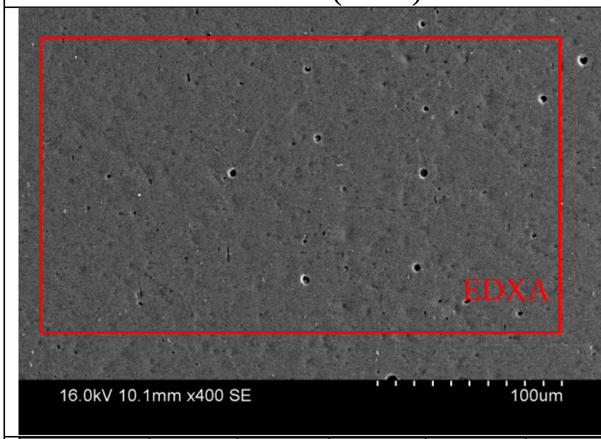	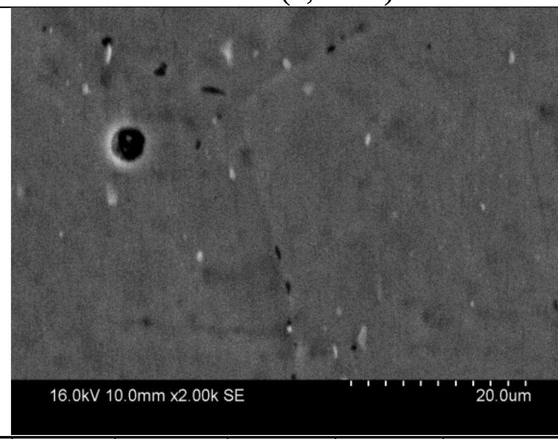

Al	**O**	**Si**	**Fe**	**Cu**	**Mn**	**Mg**	**Cr**	Ti	Zn	others
98.43	-	0.53	-	-	-	1.04	-	-	-	-

Table 8 and Table 9 below show the SEM and EDXA results for the TMAZ on the AA5086 and AA6061 side at three different magnifications, respectively.

Table 8. TMAZ of AA5086.

Overview (37X)	Course (320X)	Fine (800X)
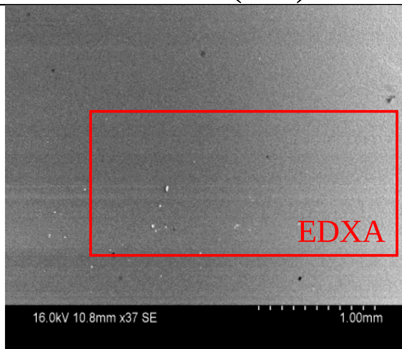	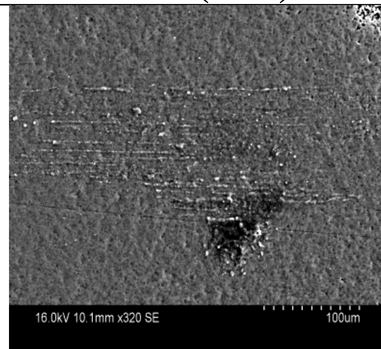	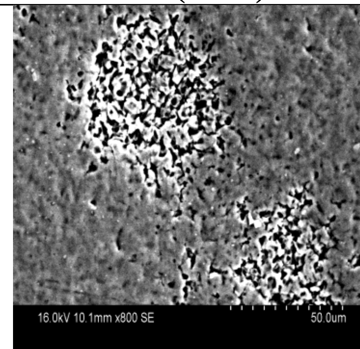

Al	**O**	**Si**	**Fe**	**Cu**	**Mn**	**Mg**	**Cr**	Ti	Zn	others
97.96	-	0.50	-	-	-	1.55	-	-	-	-

Table 9. TMAZ of AA6061.

Overview (210X)	Course (470X)	Fine (900X)
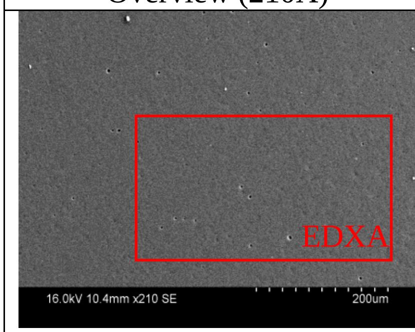	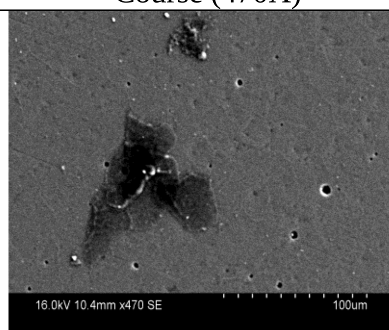	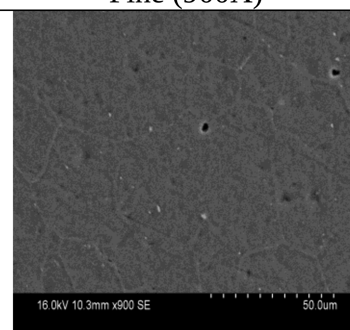

Al	**O**	**Si**	**Fe**	**Cu**	**Mn**	**Mg**	**Cr**	Ti	Zn	others
98.43	-	0.66	-	-	-	0.91	-	-	-	

Table 10 below illustrates the difference in SEM results for the topside and underside of the NZ of the dissimilar weld along with annotating the EDXA results.

Table 10. Comparison of the Topside and Underside of the AA6061-AA5086 Nugget Zone

<table>
<tr><th colspan="8">Topside(180X)</th><th colspan="8">Underside(120X)</th></tr>
<tr><td colspan="8">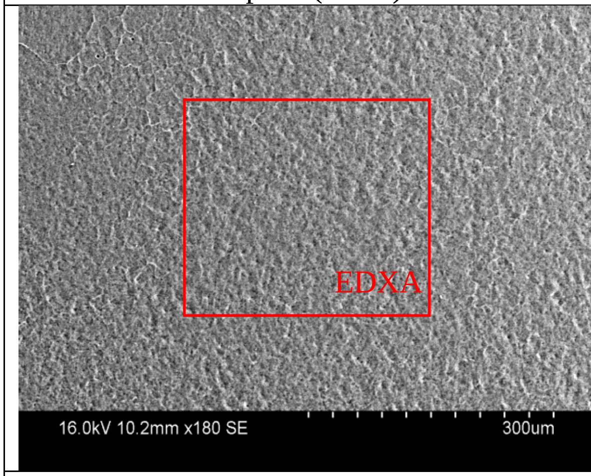
</td><td colspan="8">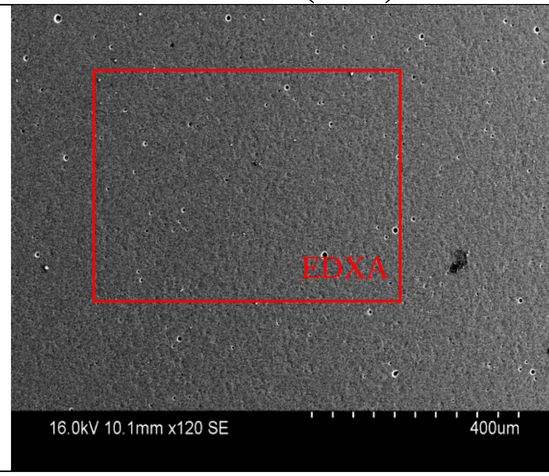
</td></tr>
<tr><td colspan="8">(1,000X)</td><td colspan="8">(1,000X)</td></tr>
<tr><td colspan="8">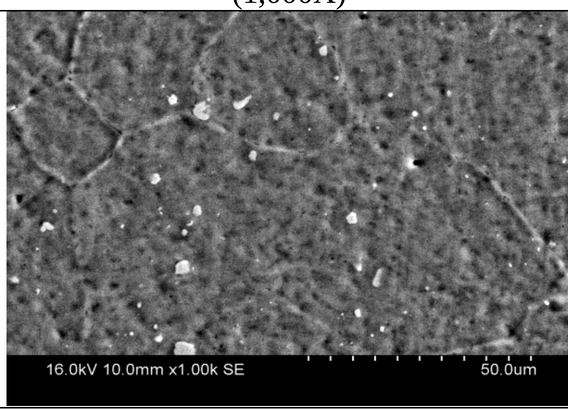
</td><td colspan="8">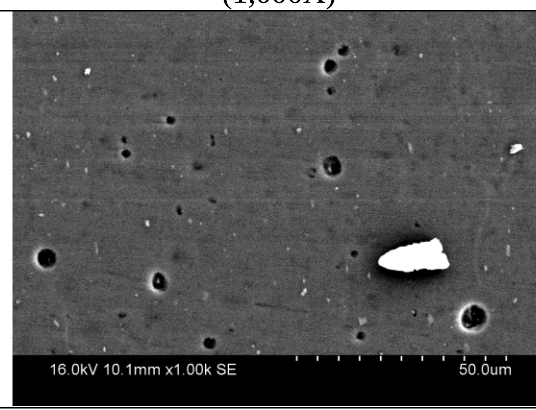
</td></tr>
<tr><td colspan="8">High porosity
Bright precipitates (flakes), 1-6 microns
Dark Pits (oval, irregular), tiny to 6 microns</td><td colspan="8">High porosity
Bright precipitates (flakes), 3-4 microns
Dark Pits (round), 1-8 microns</td></tr>
<tr><td>Al</td><td>O</td><td>Si</td><td>Fe</td><td>Cu</td><td>Mn</td><td>Mg</td><td>Cr</td><td>Al</td><td>O</td><td>Si</td><td>Fe</td><td>Cu</td><td>Mn</td><td>Mg</td><td>Cr</td></tr>
<tr><td>98.35</td><td>-</td><td>0.63</td><td>-</td><td>-</td><td>-</td><td>1.03</td><td>-</td><td>98.33</td><td>-</td><td>0.66</td><td>-</td><td>-</td><td>-</td><td>1.01</td><td>-</td></tr>
</table>

4.3.1.2 SEM and EDXA of Two Year Samples at Kilauea, Pyramid Rock, and Lyon Arboretum

This section presents the SEM and EDXA analyses for samples that accumulated the most corrosion damage, which occurred at Kilauea, Pyramid Rock, and Lyon Arboretum for the two-year exposure period. Table 11 through Table 19 exhibit the SEM results for the three types of exposed samples, AA6061-AA6061, AA5086-AA5086, and AA6061-AA5086, at the three sites.

Near means the site closer to the alphanumeric stamp, and far means the opposite. Figure 28 through Figure 36 show the EDXA results for the sample shown in the preceding table determined by taking the average of three area scans at 500X. For example, Figure 28 shows the EDXA results for the sample displayed in Table 11.

Table 11. SEM of AA6061-AA6061 at Kilauea for Two Years. (EDXA regions in red)

<table>
<tr><th></th><th></th><th>Coarse 50X</th><th>Fine 500X</th></tr>
<tr><td rowspan="7">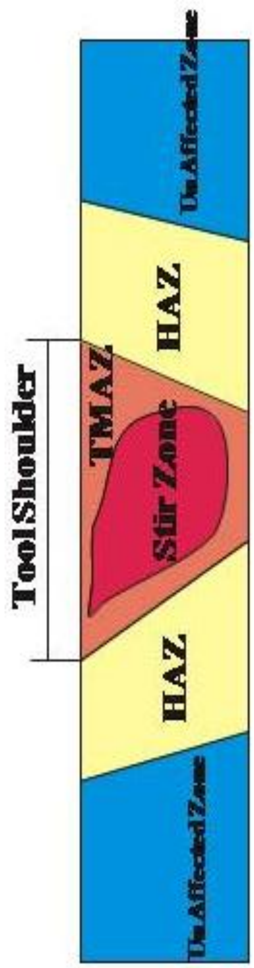
</td><td>PM Near</td><td>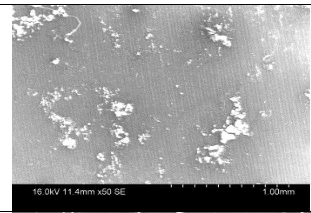
</td><td>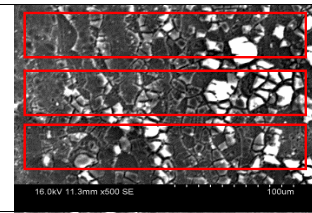
</td></tr>
<tr><td>HAZ Near</td><td>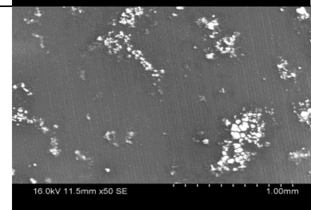
</td><td>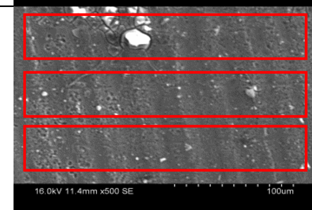
</td></tr>
<tr><td>TMAZ Near</td><td>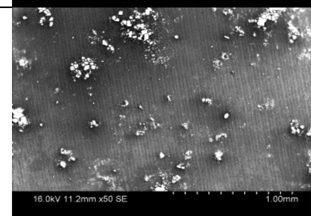
</td><td>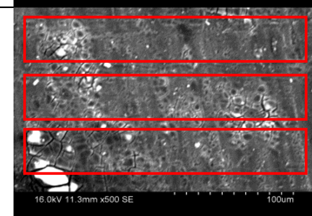
</td></tr>
<tr><td>NZ</td><td>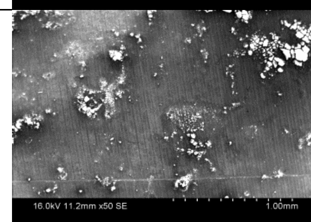
</td><td>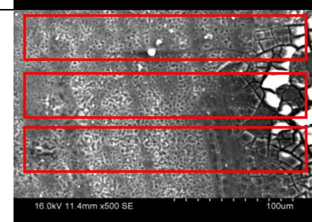
</td></tr>
<tr><td>TMAZ Far</td><td>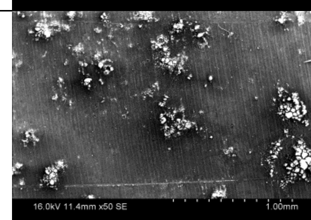
</td><td>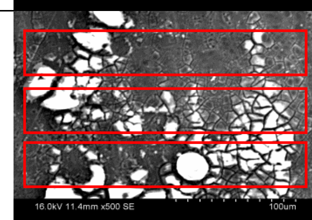
</td></tr>
<tr><td>HAZ Far</td><td>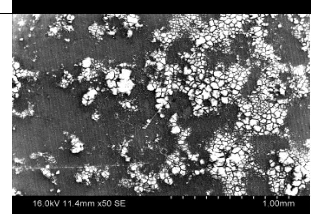
</td><td>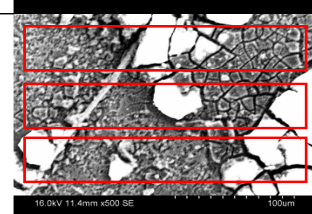
</td></tr>
<tr><td>PM Far</td><td>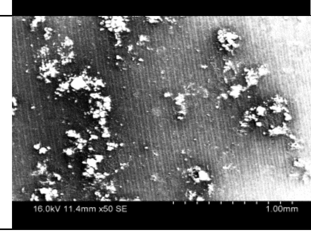
</td><td>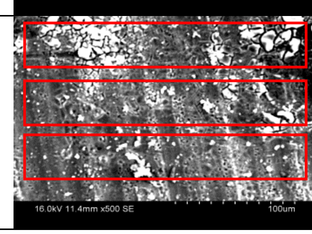
</td></tr>
</table>

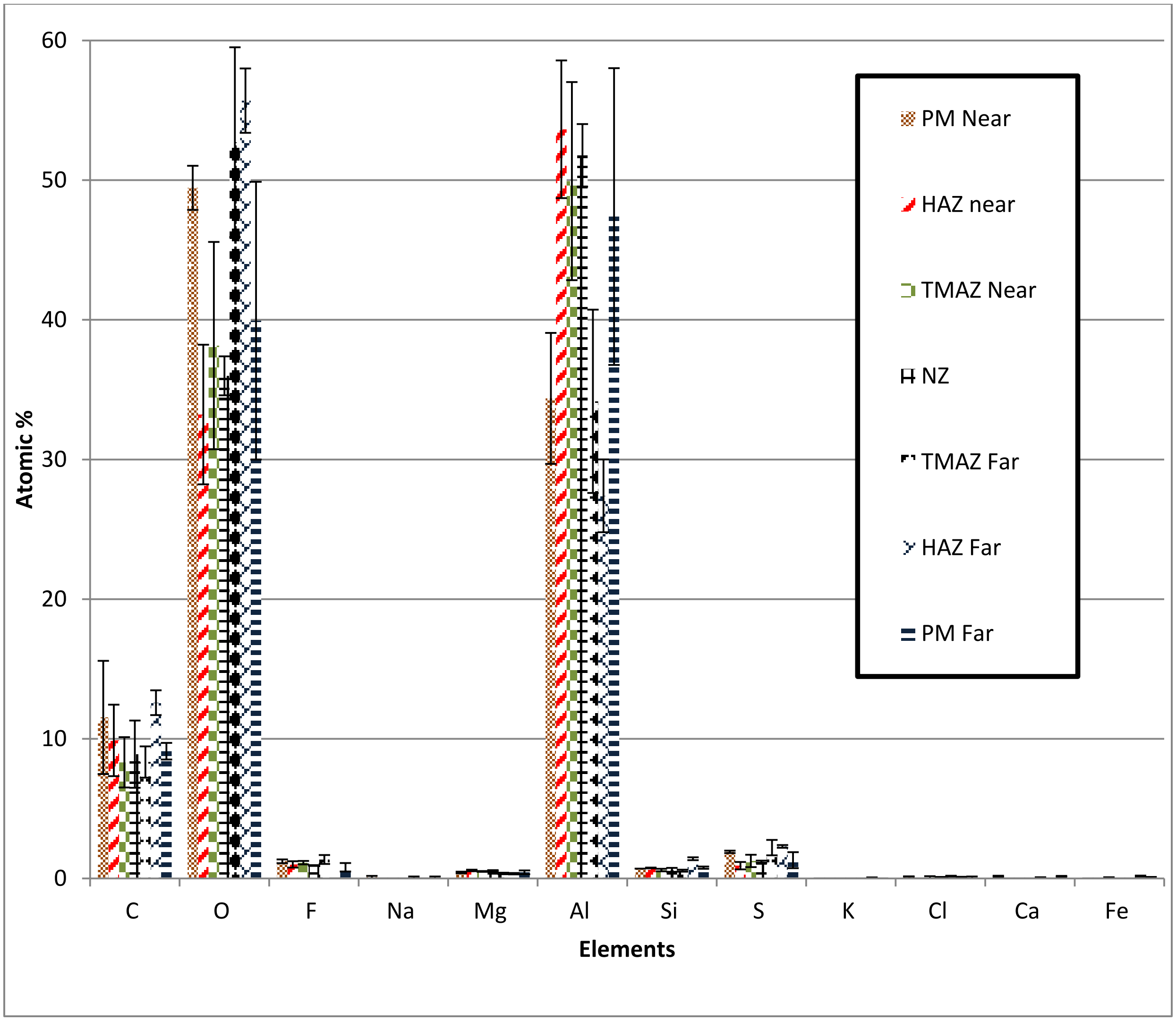

Figure 28: Chemical Composition of AA6061- AA6061 at Kilauea for Two Years.

Table 12. SEM of AA5086-AA5086 at Kilauea for Two Years. (EDXA regions in red)

		Coarse 50X	Fine 500X
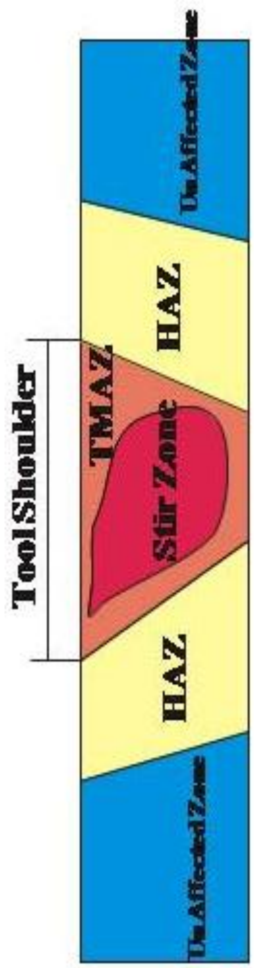	PM Near	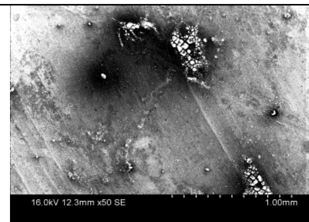	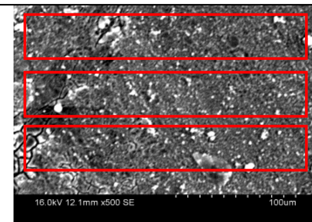
	HAZ Near	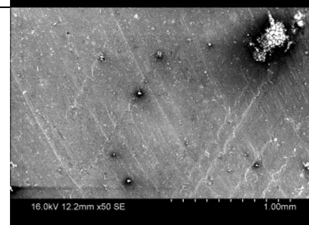	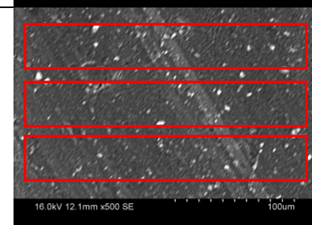
	TMAZ Near	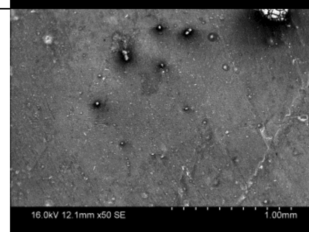	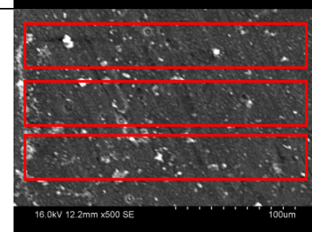
	NZ		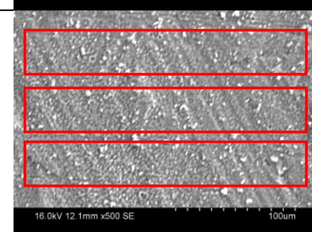
	TMAZ Far	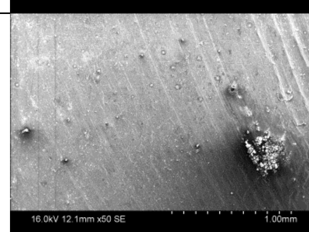	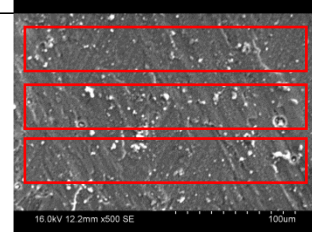
	HAZ Far	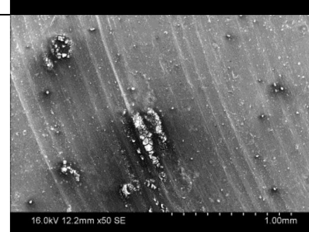	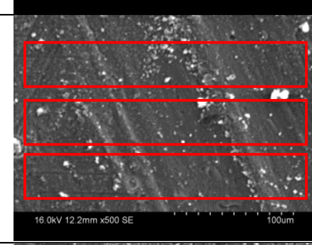
	PM Far	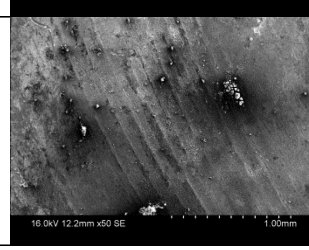	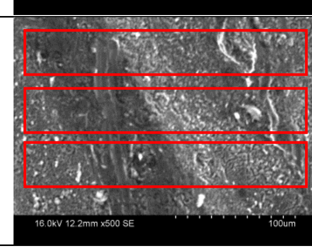

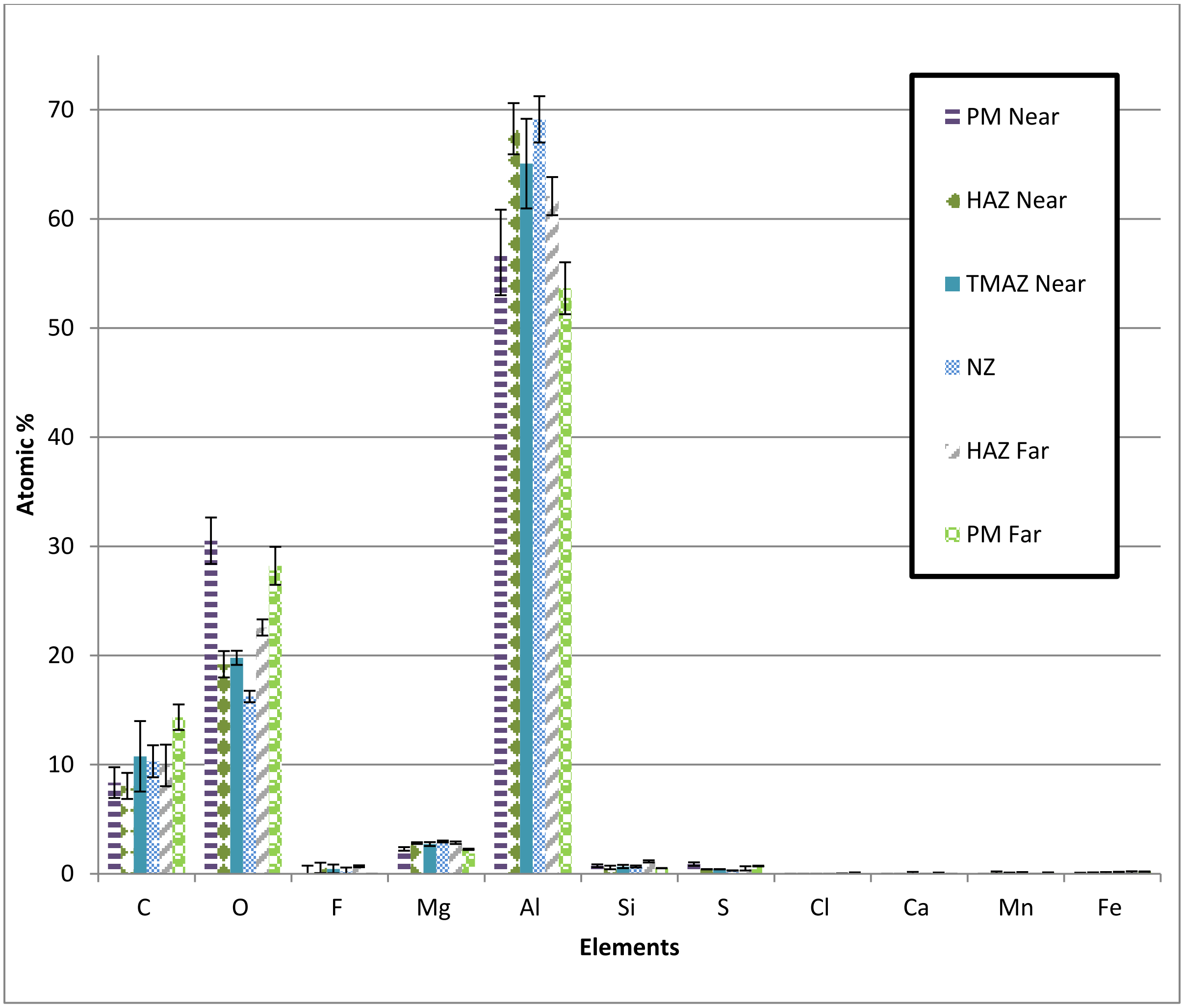

Figure 29: Chemical Composition of AA5086-AA5086 at Kilauea for Two Years.

Table 13. SEM of AA6061-AA5086 at Kilauea for Two Years. (EDXA regions in red)

		Coarse 50X	Fine 500X
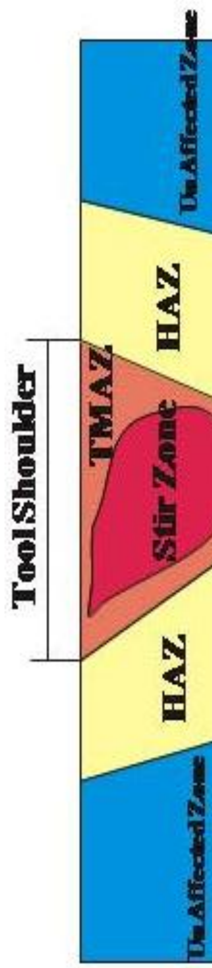	PM Near	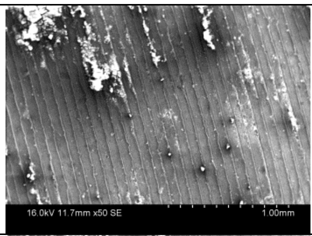	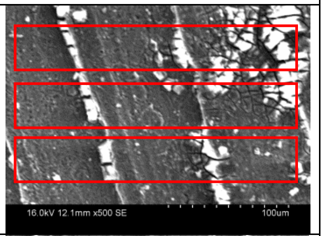
	HAZ Near	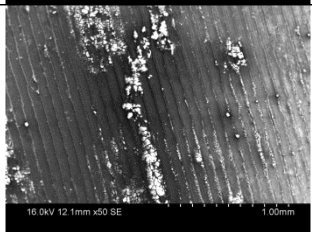	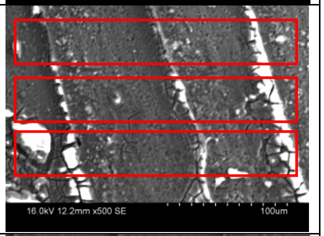
	TMAZ Near	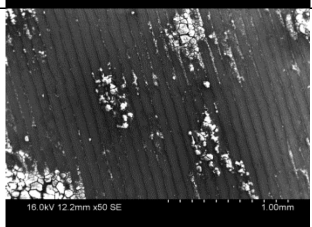	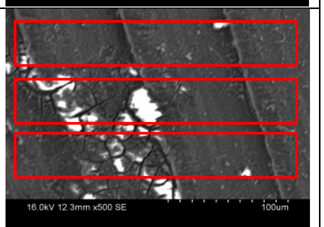
	NZ	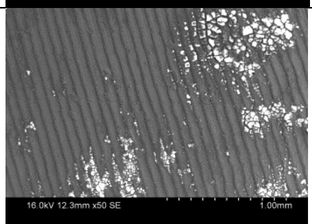	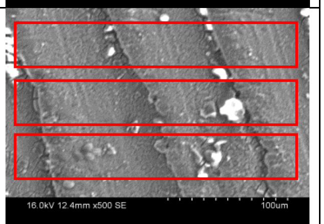
	TMAZ Far	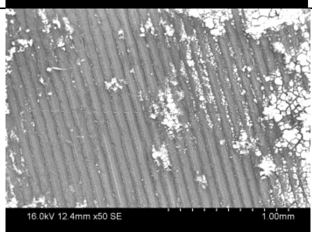	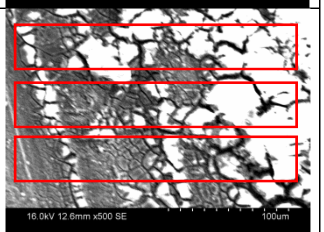
	HAZ Far	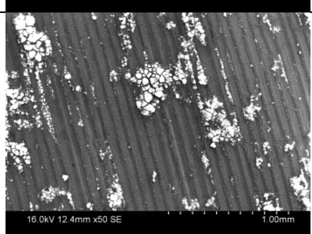	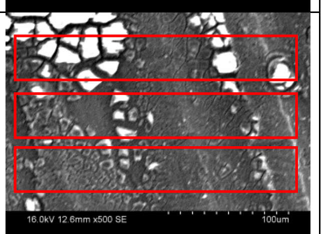
	PM Far	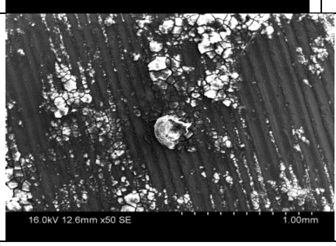	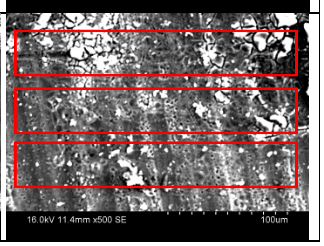

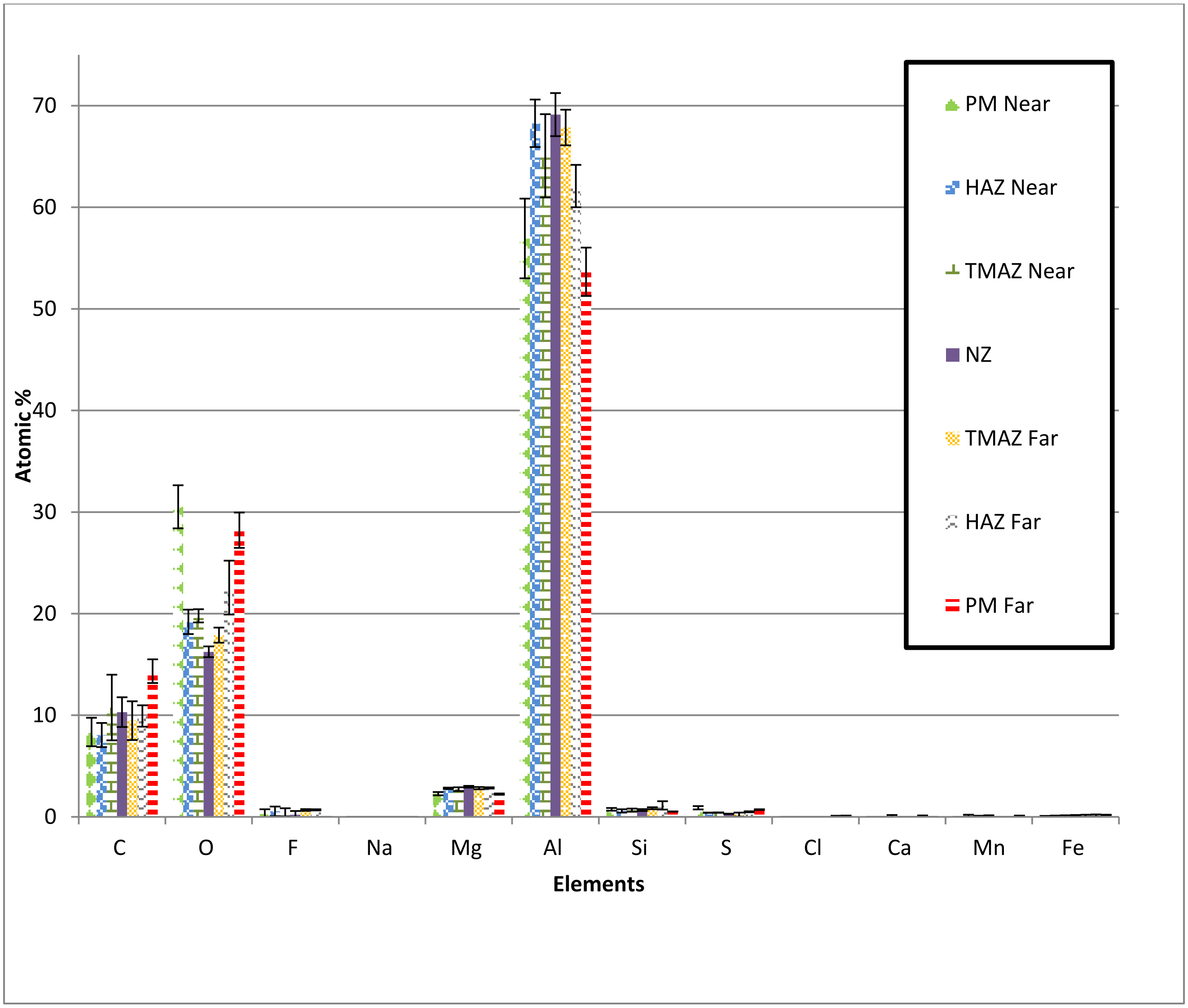

Figure 30: Chemical Composition of AA6061-AA5086 at Kilauea for Two Years.

Table 14. SEM of AA6061-AA6061 at Pyramid Rock for Two Years. (EDXA regions in red)

		Coarse 50X	Fine 500X
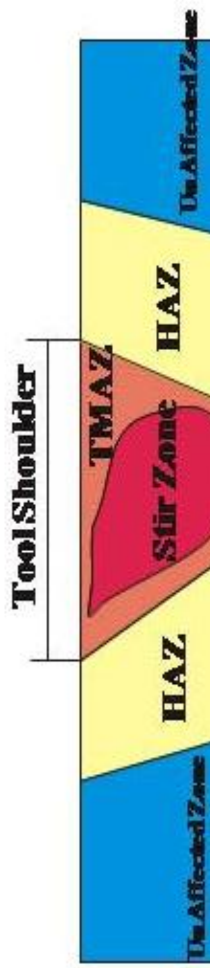	PM Near	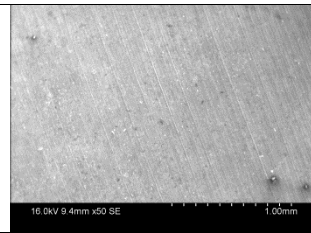	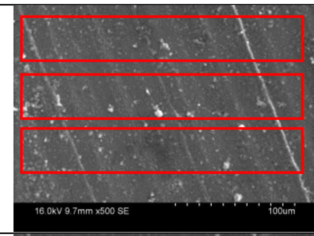
	HAZ Near	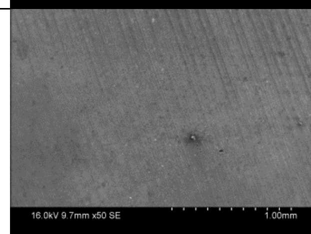	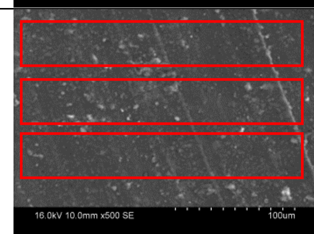
	TMAZ Near	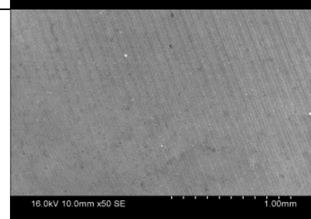	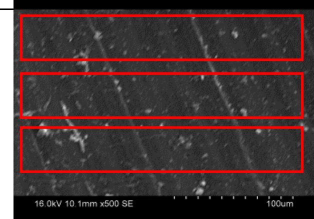
	NZ	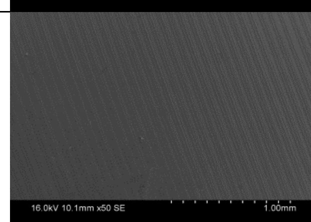	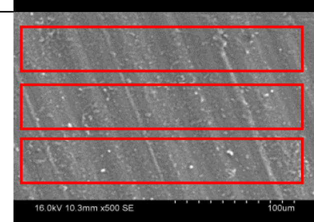
	TMAZ Far	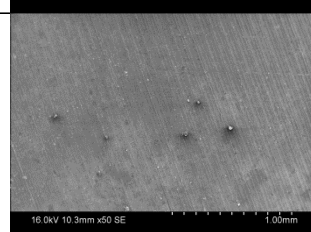	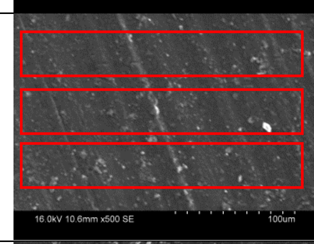
	HAZ Far	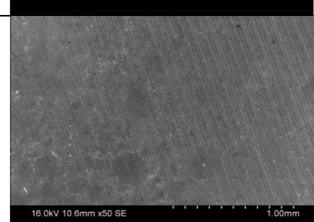	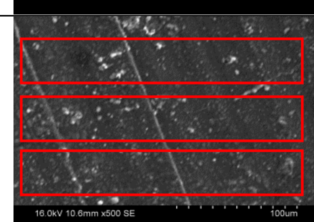
	PM Far	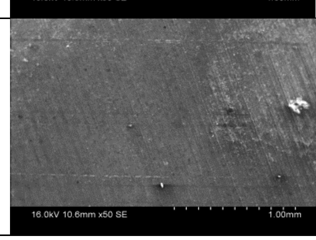	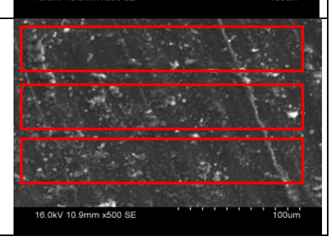

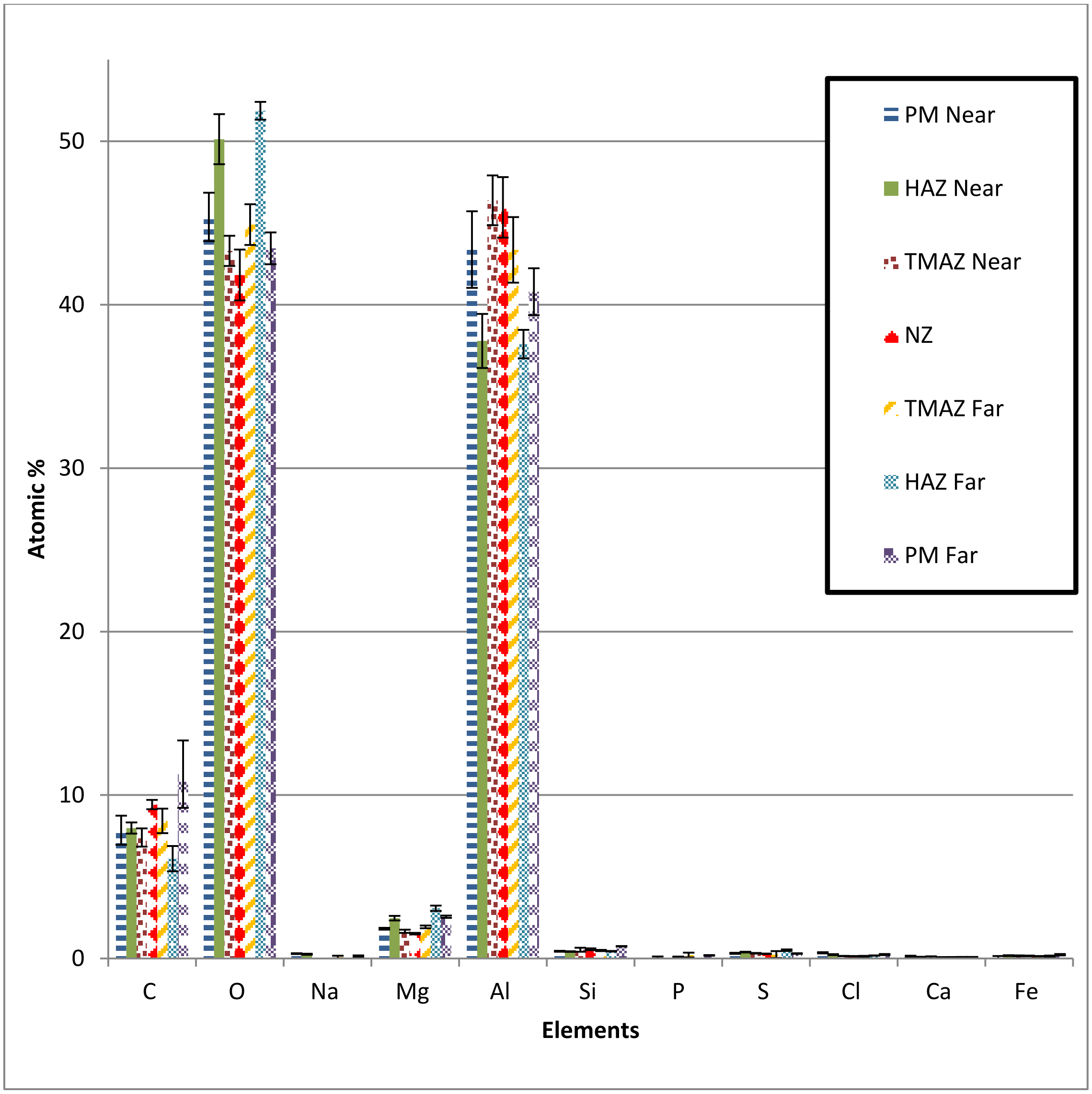

Figure 31: Chemical Composition of AA6061-AA6061 at Pyramid Rock for Two Years.

Table 15. SEM of AA5086-AA5086 at Pyramid Rock for Two Years. (EDXA regions in red)

		Coarse 50X	Fine 500X
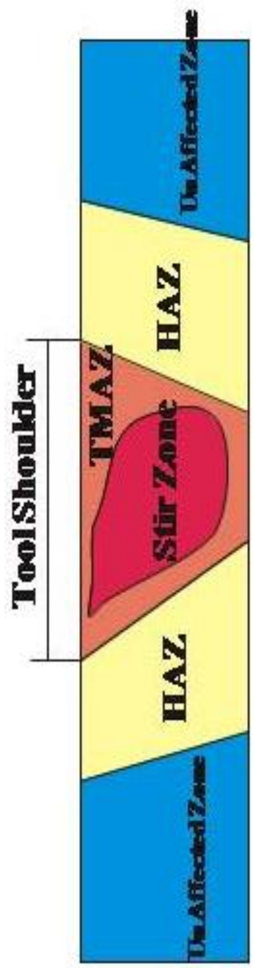	PM Near	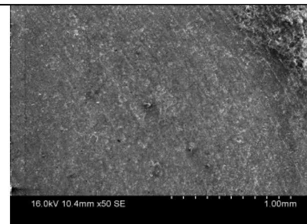	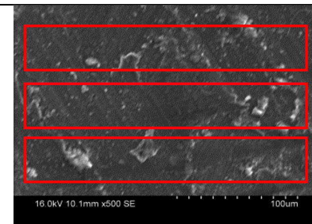
	HAZ Near	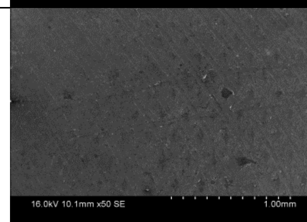	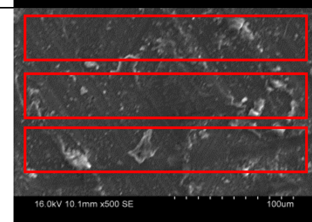
	TMAZ Near	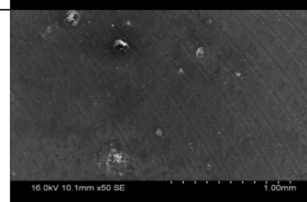	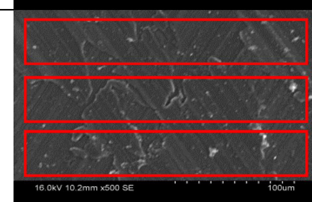
	NZ	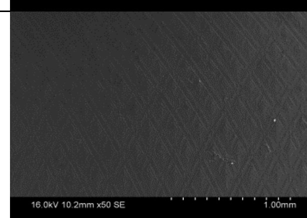	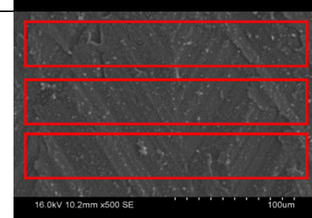
	TMAZ Far	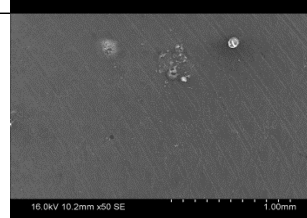	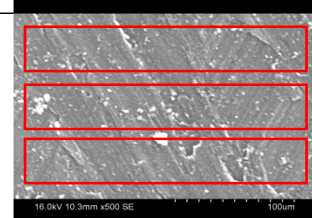
	HAZ Far	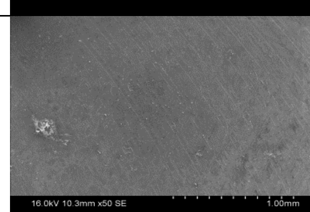	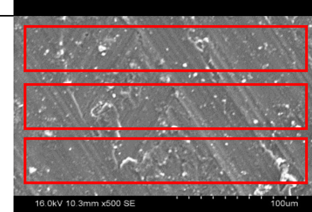
	PM Far	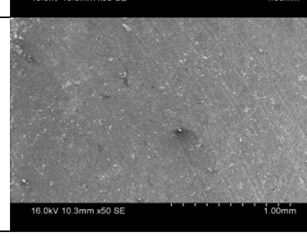	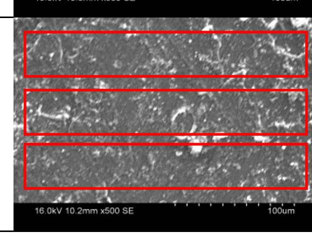

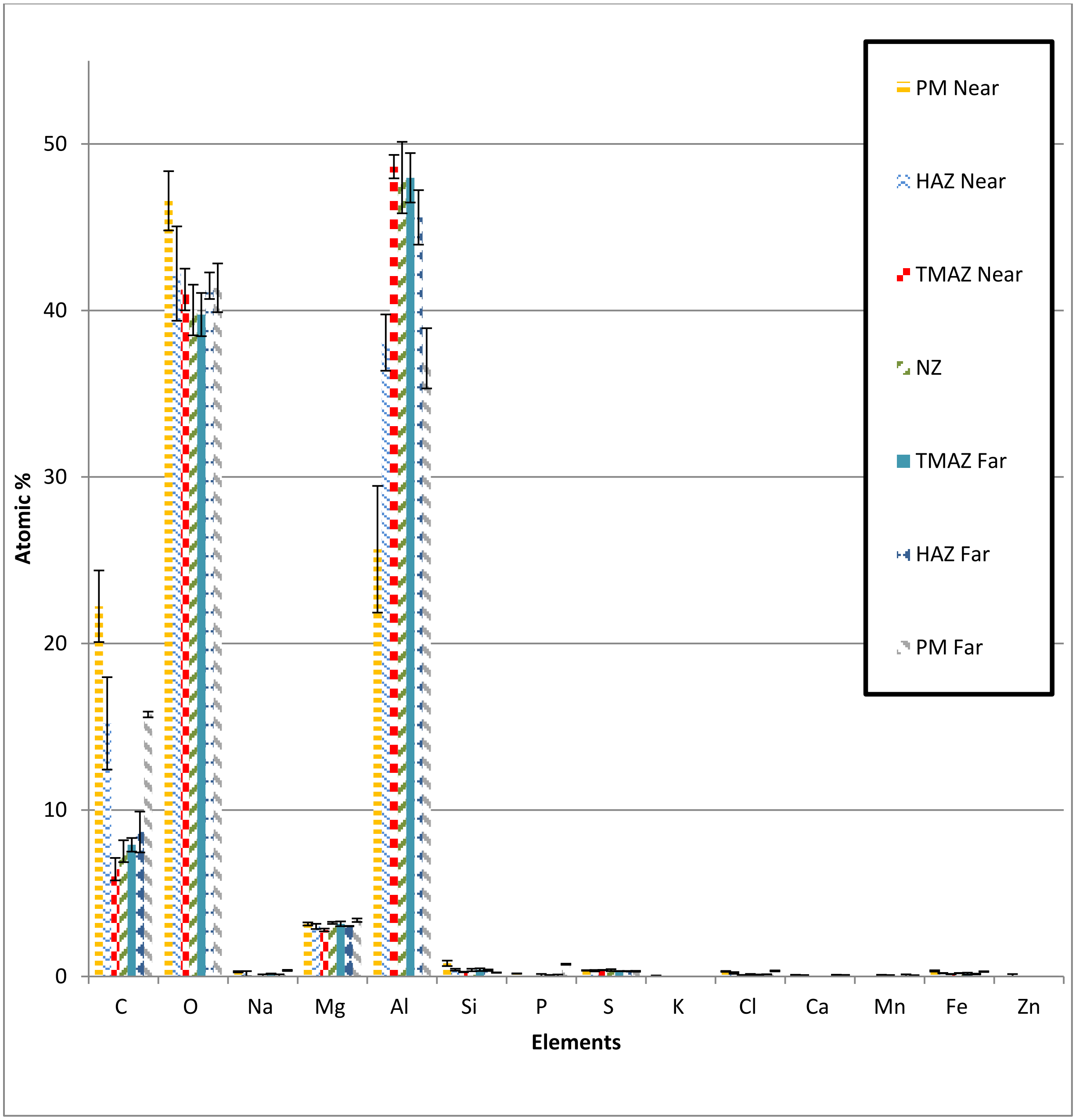

Figure 32: Chemical Composition of AA5086-AA5086 at Pyramid Rock for Two Years.

Table 16. SEM of AA6061-AA5086 at Pyramid Rock for Two Years. (EDXA regions in red)

		Coarse 50X	Fine 500X
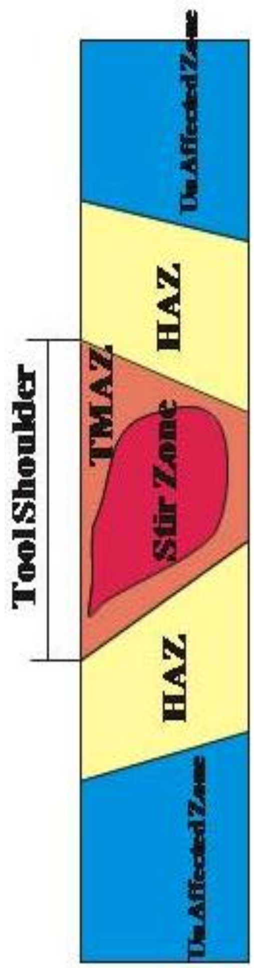	PM Near	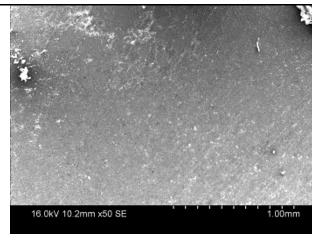	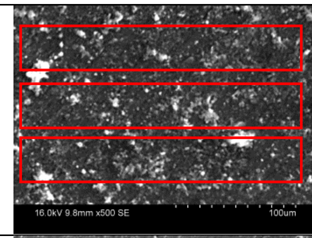
	HAZ Near	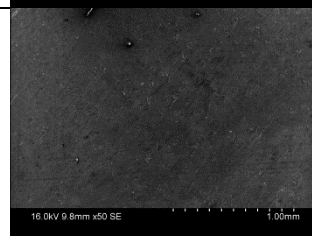	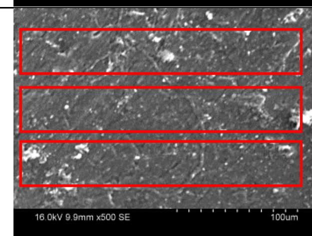
	TMAZ Near	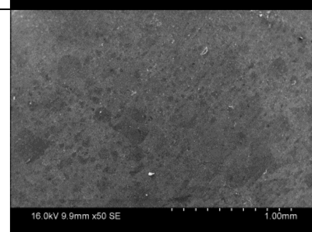	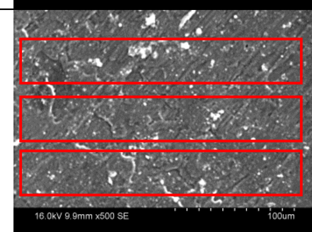
	NZ	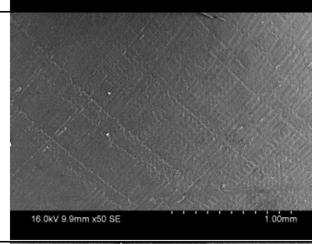	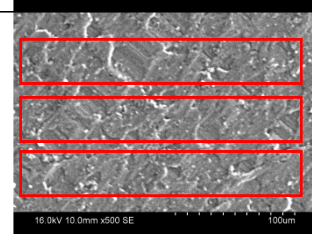
	TMAZ Far	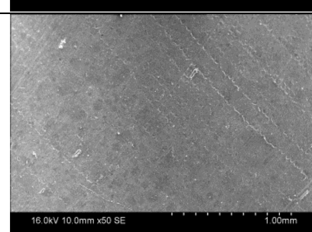	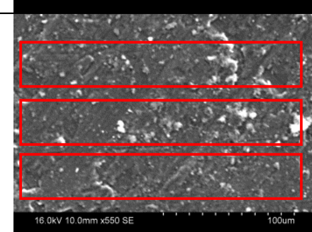
	HAZ Far	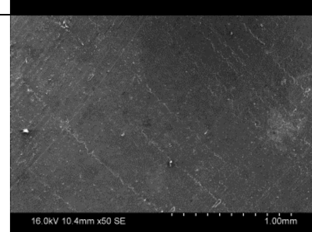	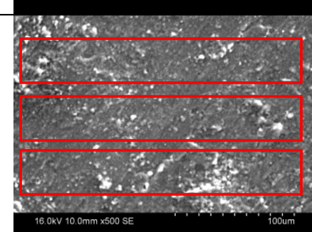
	PM Far	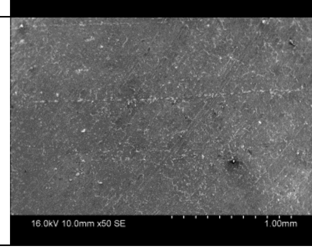	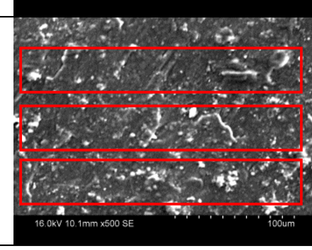

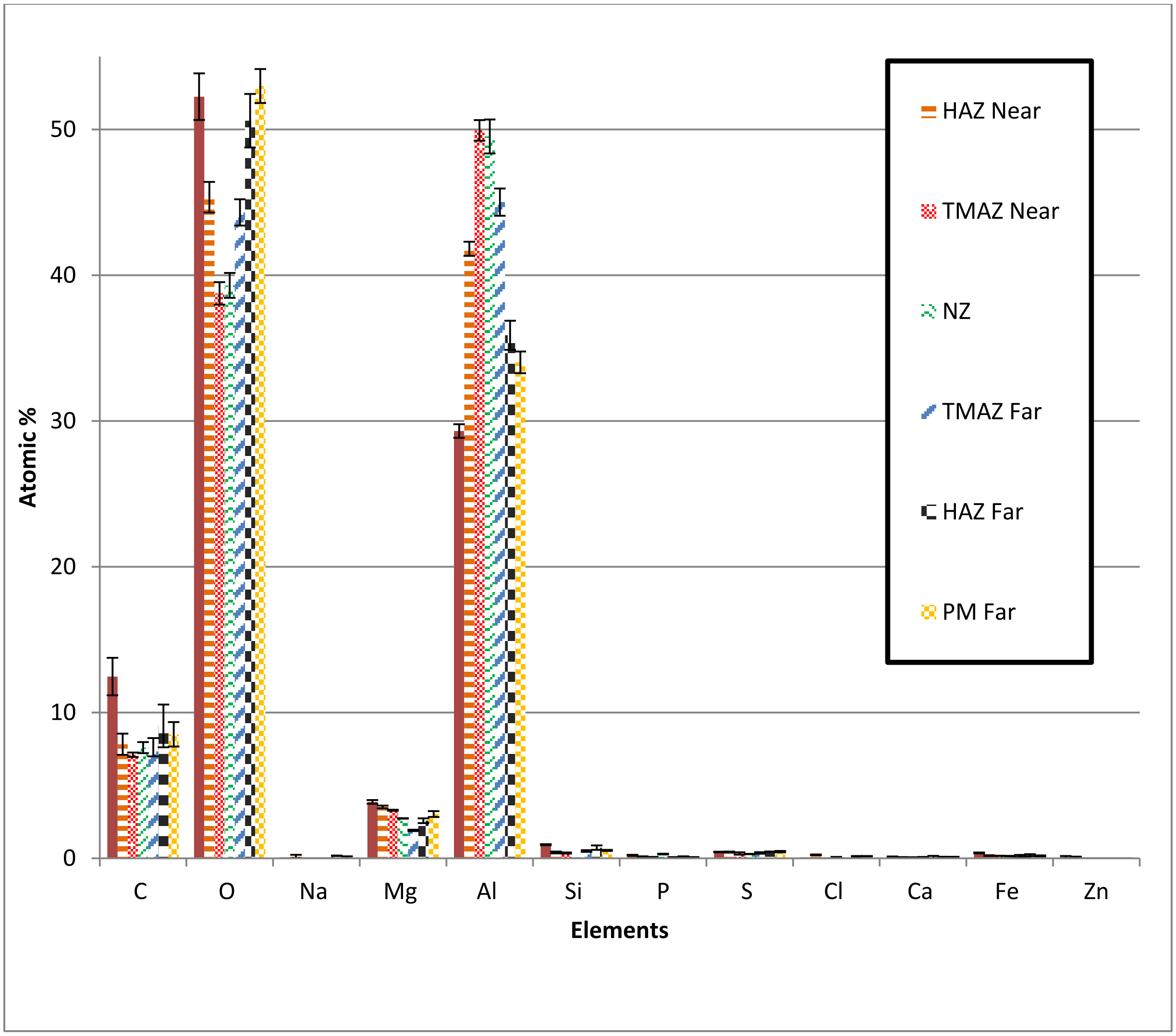

Figure 33: Chemical Composition of AA6061-AA5086 at Pyramid Rock for Two Years.

Table 17. SEM of AA6061-AA6061 at Lyon Arboretum for Two Years. (EDXA regions in red)

		Coarse 50X	Fine 500X
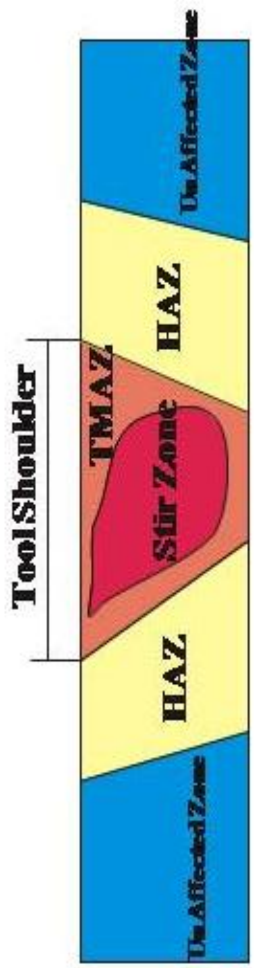	PM Near	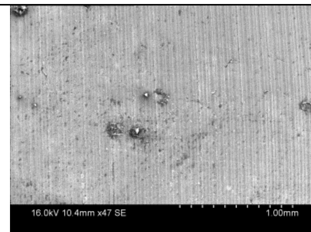	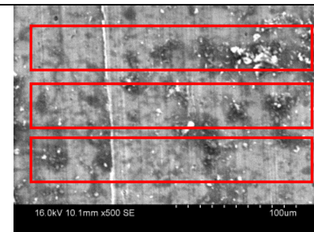
	HAZ Near	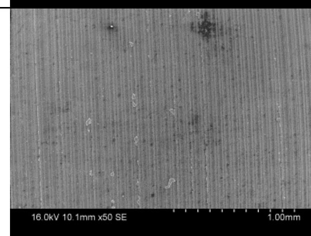	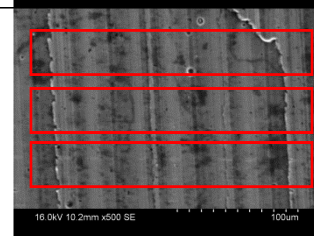
	TMAZ Near	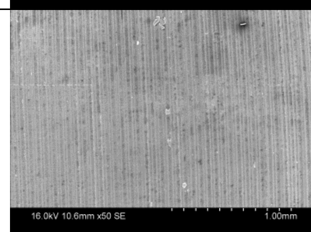	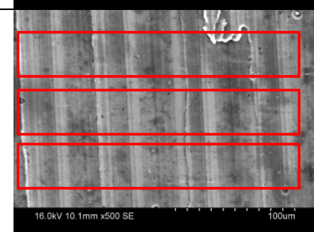
	NZ	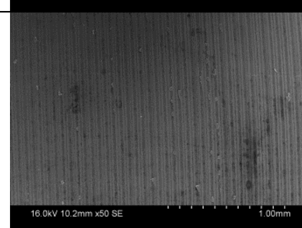	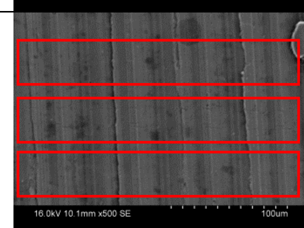
	TMAZ Far	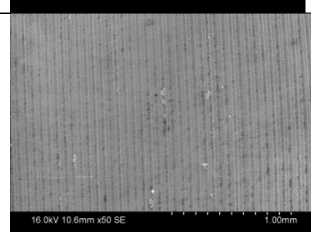	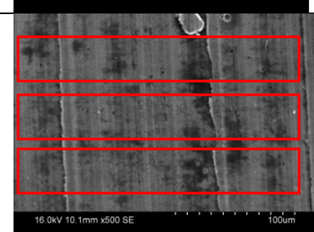
	HAZ Far	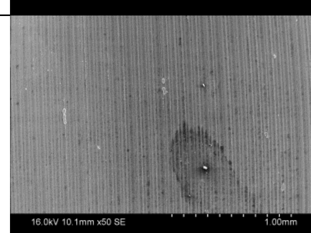	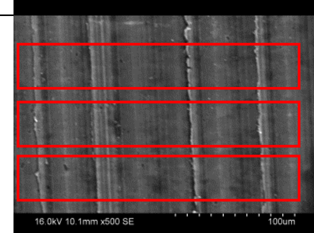
	PM Far	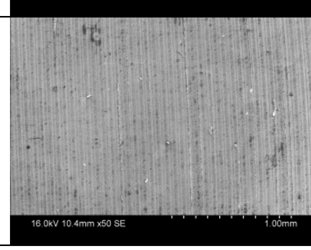	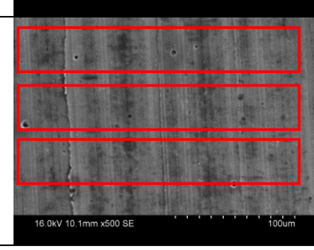

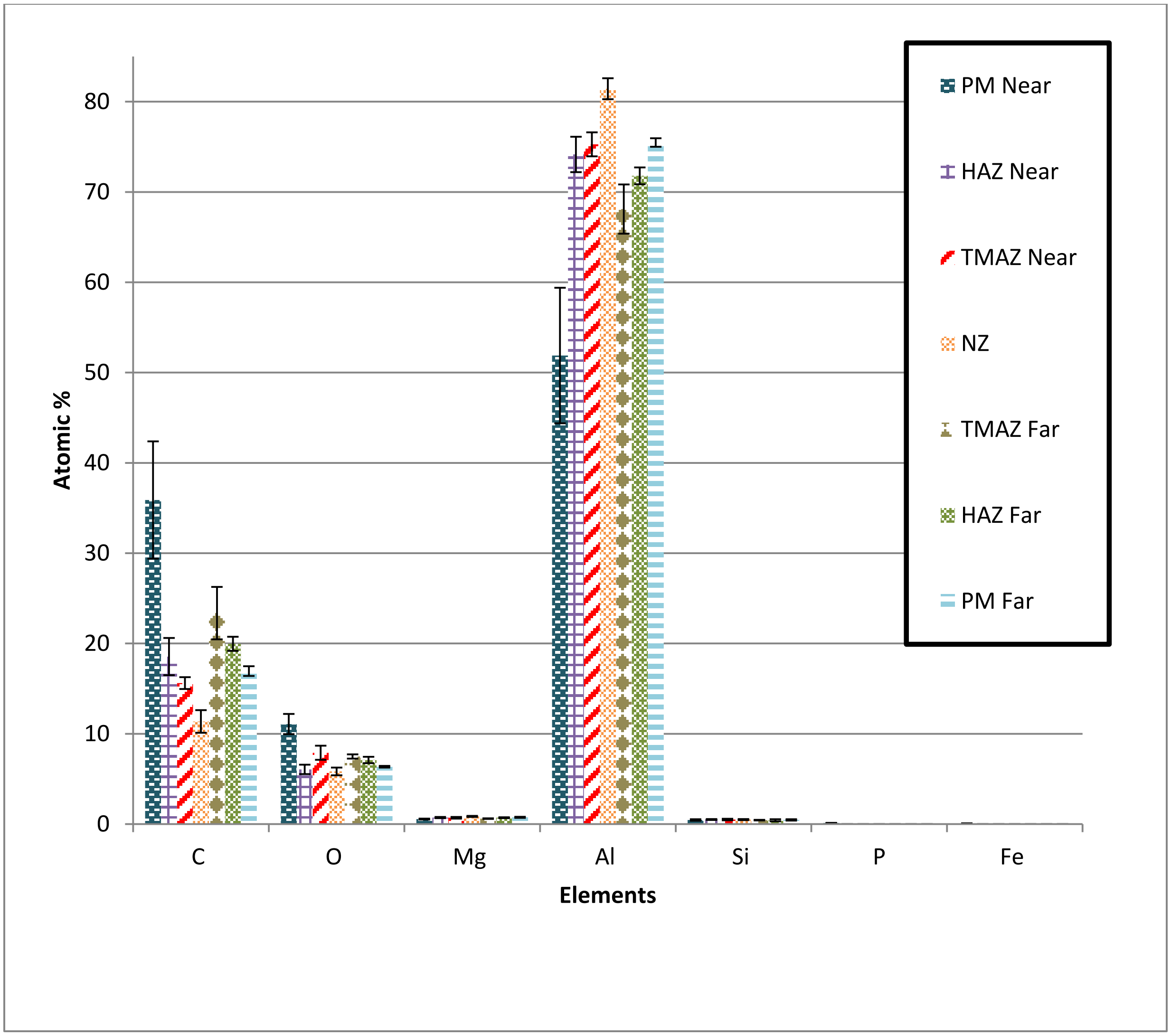

Figure 34: Chemical Composition of AA6061-AA6061 at Lyon Arboretum Rock for Two Years.

Table 18. SEM of AA5086-AA5086 at Lyon Arboretum for Two Years. (EDXA regions in red)

		Coarse 50X	Fine 500X
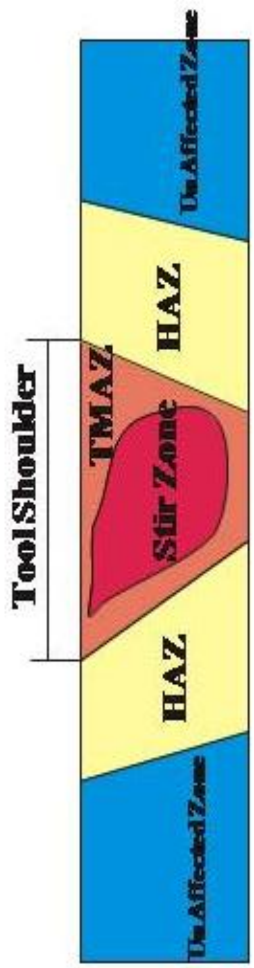	PM Near	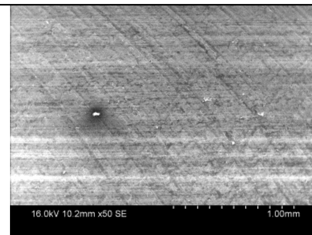	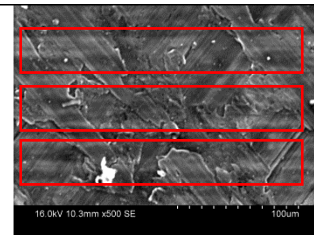
	HAZ Near	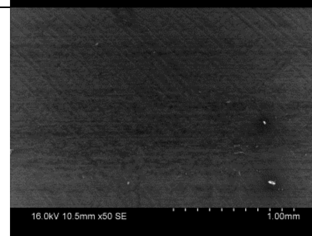	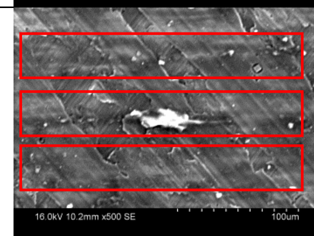
	TMAZ Near	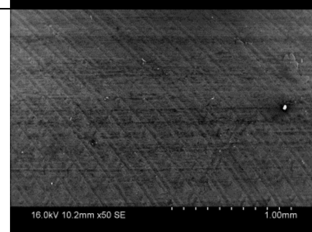	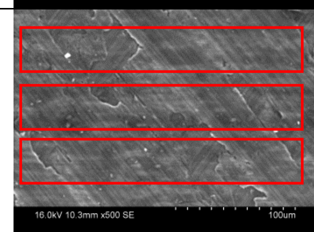
	NZ	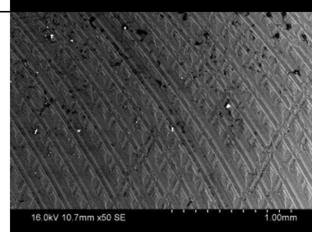	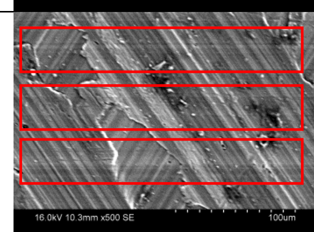
	TMAZ Far	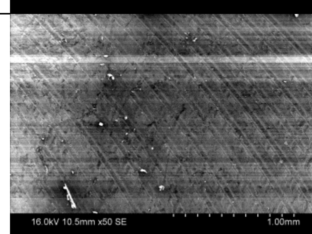	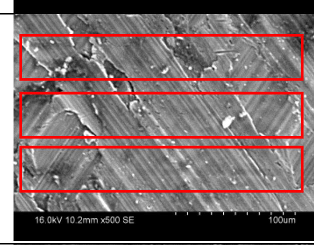
	HAZ Far	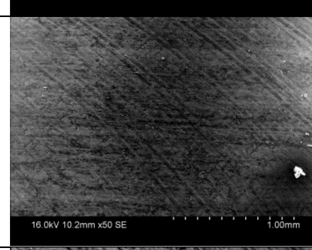	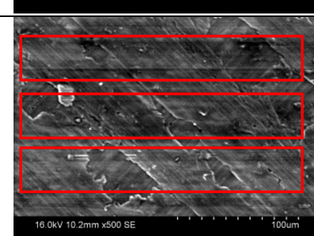
	PM Far	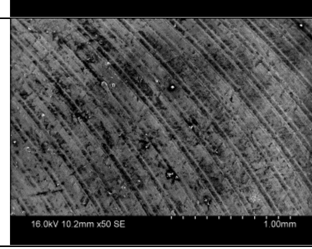	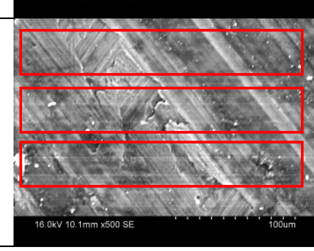

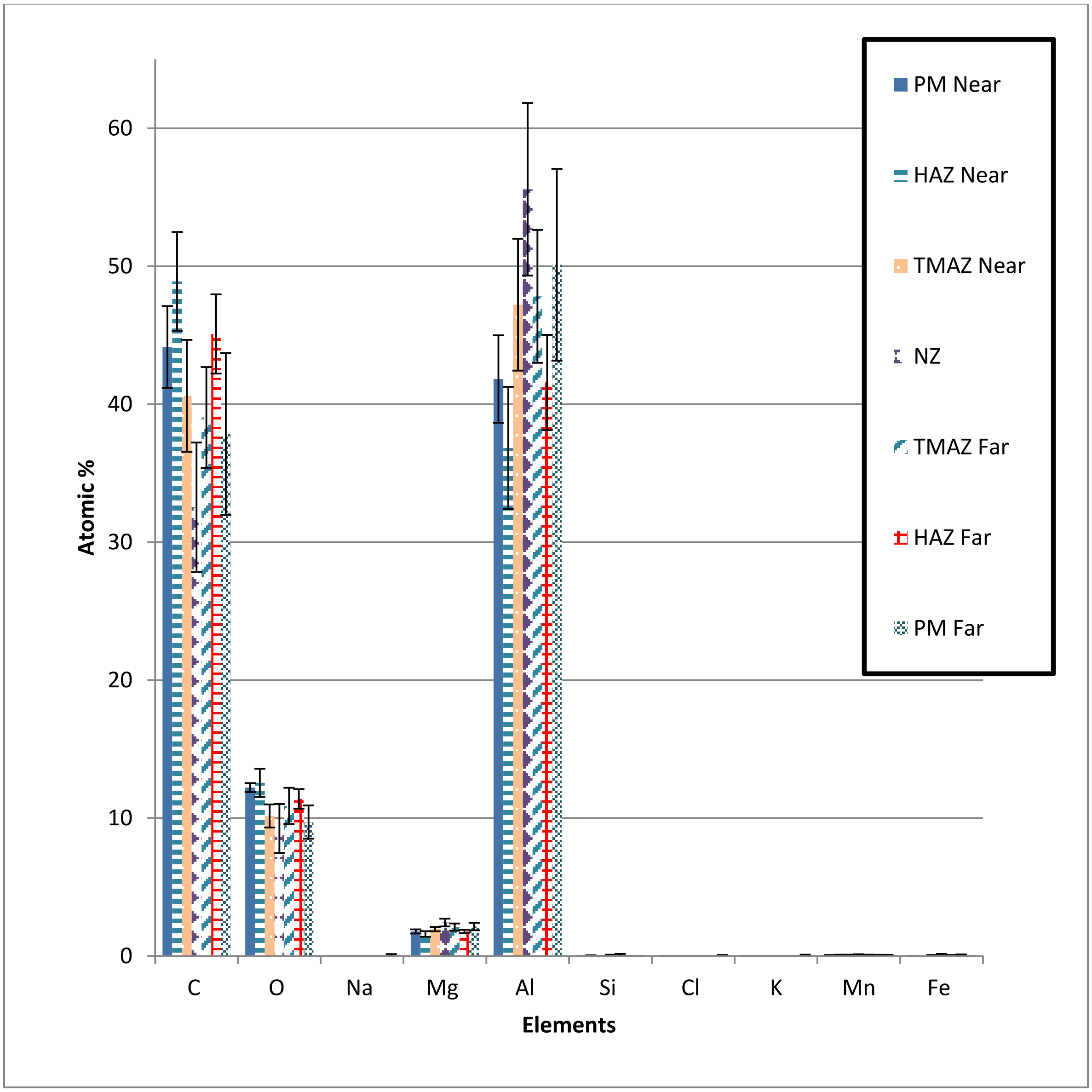

Figure 35: Chemical Composition of AA5086-AA5086 at Lyon Arboretum for Two Years.

Table 19. SEM of AA6061-AA5086 at Lyon Arboretum for Two Years. (EDXA regions in red)

		Coarse 50X	Fine 500X
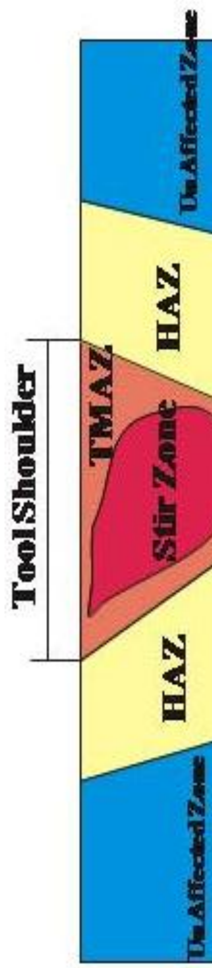	PM Near	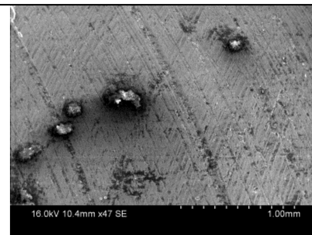	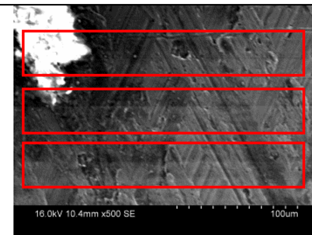
	HAZ Near	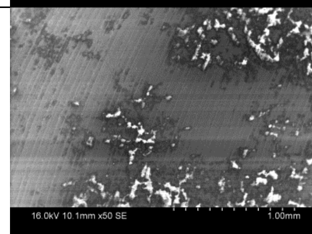	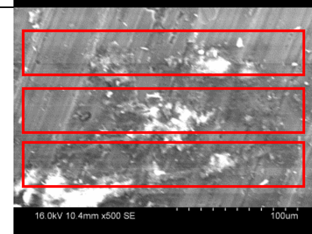
	TMAZ Near	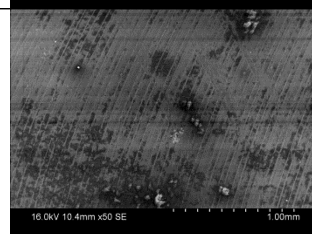	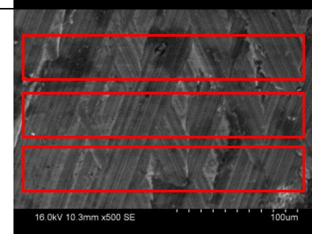
	NZ	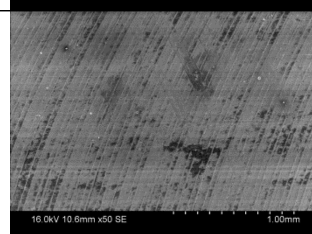	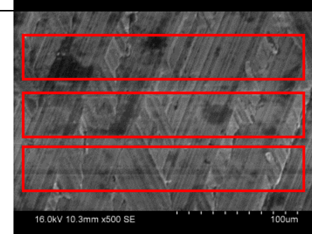
	TMAZ Far	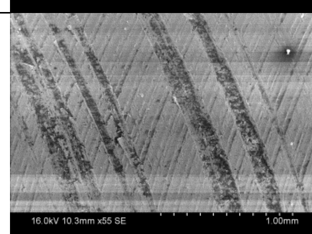	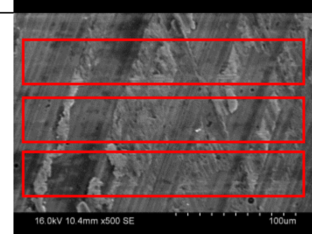
	HAZ Far	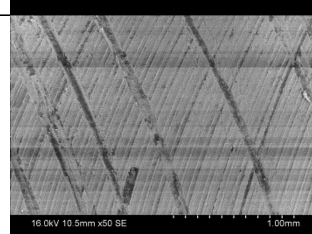	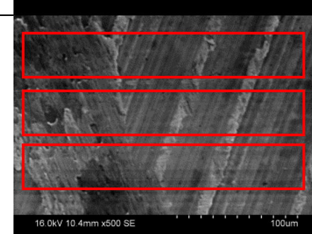
	PM Far	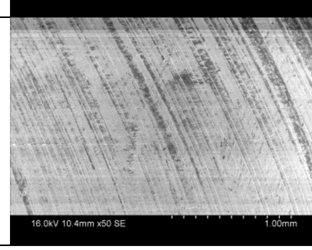	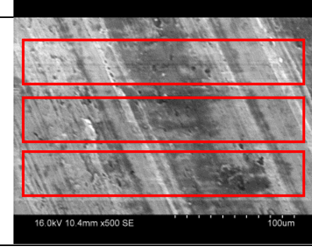

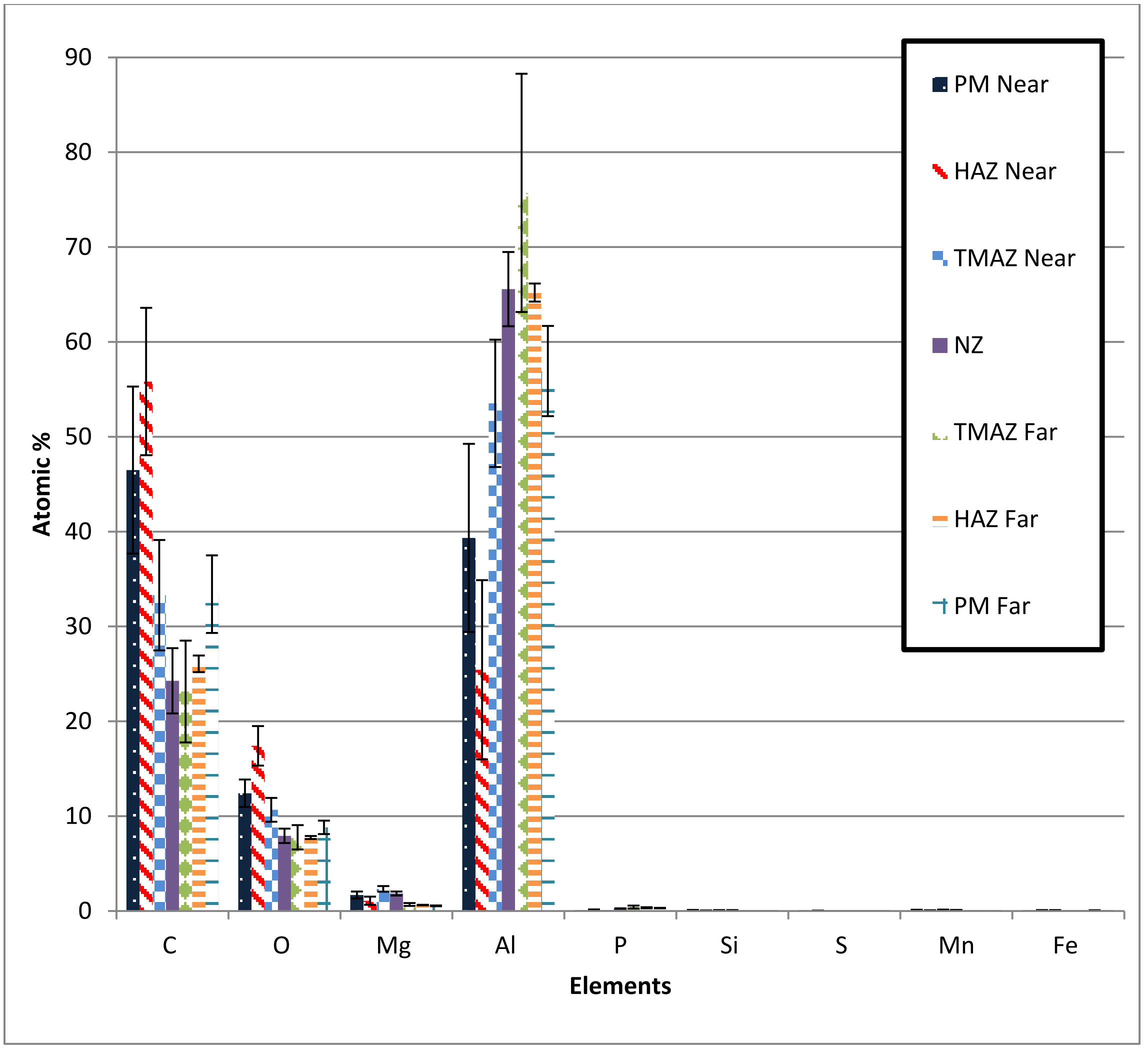

Figure 36: Chemical Composition of AA6061-AA5086 at Lyon Arboretum for Two Years.

4.3.2 Discussion

This section discusses some prominent observations from the preceding tables and figures. First, a comparison between an unexposed and exposed dissimilar weld of AA6061-AA5086 will be presented. Then, a comparison between the samples at the Kilauea, Pyramid rock, and Lyon Arboretum will be presented.

4.3.2.1 Comparison of Unexposed Parent Metal and the Two-Year, Kilauea-Exposed AA6061-AA5086 Weld Samples

The unexposed AA5086 and AA6061 parent metals exhibited slight signs of porosity or pitting (Table 4), which may have resulted during polishing of the metallographic specimens. Traces of white precipitates were also observed on the specimens, which may have been corrosion products resulting from the polishing and subsequent cleaning process. These white precipitates were scattered and singular in formation. Meanwhile, the parent AA5086 and AA6061 zones of the dissimilar weld sample at Kilauea had tremendous accumulation and clustering of corrosion products (Table 13). Both the unexposed AA6061 parent metal (Table 4) and the AA6061 parent metal on the dissimilar weld exposed to Kilauea (Table 13) exhibited more signs of corrosion product than the unexposed (Table 4) and exposed (Table 13) AA5086 parent metal in the dissimilar weld. The unexposed AA6061 and AA5086 parent material did not show traces of carbon, whereas, the exposed samples showed significant amounts. The carbon content of the exposed samples could be due carbonates such as calcium carbonate from coral sand, or organic matter such as algae or moss. Note that at the marine Pyramid Rock and Kilauea sites, the carbon content was approximately 10% and likely caused by sand; whereas, at Lyon Arboretum, the carbon content was approximately 50% which was likely due to residual algae or moss on the samples. Additionally, the oxygen percentage for the unexposed samples of the parent material zones were less than 2% while the exposed sample at Kilauea were nearly 30%. Aluminum level was lower in the exposed sample. For example, the unexposed sample had over 90% Al while the exposed sample had less than 60%. The low oxygen and high aluminum content signifies very little corrosion while the high oxygen and low aluminum content indicates the presence of aluminum oxide corrosion products. Furthermore, the bright precipitates seen on the unexposed samples were roughly between 1-9 microns while those in the exposed samples were at least one order of magnitude larger.

The heat affected zone on the AA5086 side of the unexposed sample (Table 6) showed signs of circular voids or pits along with sparse white corrosion product resulting from the polishing and subsequent cleaning process. The SEM results of the two-year sample at Kilauea did not show any signs of pitting, but they did show significantly more white corrosion products in large clusters (Table 13). The bright corrosion product appeared to be located near the pits for unexposed sample which is not the case for the exposed sample. The HAZ for the AA6061 side of the unexposed sample had 98.43% Al while the same zone in the exposed sample almost 70%. Similarly, the HAZ of the AA5086 unexposed sample had 95.46% Al while the same zone in the exposed sample had almost 70%. The drop in Al was nearly the same for the two HAZs.

The thermo-mechanically affected zone of the unexposed sample on the AA5086 side was more porous than the AA6061 side. This observation was not present in the exposed sample (Table 13), but porous regions could have been hidden under the corrosion product layer. The TMAZ of the unexposed AA5086 side had pits that were irregular in shape (Table 8) while the TMAZ of the unexposed AA6061 side had circular pits. The exposed samples showed signs of cracks in the corrosion product layer only and no pits were visible. Corrosion products were significantly more on the exposed samples. There was a slight rise of Si percentage in the exposed sample. In the unexposed sample, Si percentage was 0.50% and 0.66% for the TMAZ of AA5086 and AA6061, respectively. In the exposed sample, the percentages were 0.65% and 0.85% for the TMAZ of AA5086 and AA6061, respectively.

In the nugget zone of the unexposed sample (Table 10), pits or porosity were present on the topside and even more on the underside. On the exposed sample, pits were not visible, but could have been hidden under the corrosion products. The white precipitates on the unexposed sample ranged from 1-6 microns on the topside and from 3-4 microns on the underside. There was no oxygen in the unexposed sample, while there was about 17% present in the exposed sample at the NZ.

4.3.2.2 Comparison of Two-Year Exposed AA6061-AA5086 Weld Samples at Kilauea, Pyramid Rock, and Lyon Arboretum

There were some general trends among the samples at the various sites. Kilauea samples had more corrosion product visible than the other two sites with the AA6061 sample there being the most corroded of all the samples. The percentage of aluminum tended to be higher and oxygen lower closer to the NZ among the samples. In the outer zones, aluminum tended to be lower and oxygen higher with increasing distance from the NZ. This trend is indicative of lower amounts of corrosion in the NZ and higher amounts of corrosion farther from the NZ. Lyon Arboretum generally had less oxygen, around 10%, than the other two sites, around 20%-50%. The lower oxygen percentage at Lyon Arboretum was likely caused by the significant presence of carbon due to the presence of residual algae or moss.

Most of the oxygen-to-aluminum ratios from the EDXA analyses did not match up stoichiometrically with that of typical aluminum corrosion products. Aluminum hydroxide $Al(OH)_3$ and aluminum oxide Al_2O_3 have O-to-Al ratios of 3:1 and 1.5:1, respectively. At Kilauea, where the corrosion rates were highest, it would be expected that the uncleaned, exposed samples analyzed in the SEM would have shown O-to-Al ratios similar to that of the aluminum corrosion products; whereas, in fact, the O-to-Al ratios ranged from 1:1 to 1:3 for the various specimens. One explanation for this incongruity could be due to the presence of acid rain at Kilauea that could wash away most of the $Al(OH)_3$ or Al_2O_3, both of which are amphoteric. If the oxide layer is thin, the EDXA sampling volume will include substrate aluminum, hence, decreasing the O-to-Al ratio. At Pyramid Rock, the O-to-Al ratios were approximately 1:1 but still lower than the expected 3:1 or 1.5:1 ratio. At Lyon Arboretum, where corrosion rates were the least of the three sites, the O-to-Al ratios ranged from approximately 1:5 to 1:15.

Other abnormal element percentages can also be explained. Carbon presence was appreciable at the three sites, particularly Lyon Arboretum (Figures 34, 35, and 36). The high percentage of carbon at Lyon Arboretum could be attributed to the algae or moss growth or transfer of organic matter from nearby plants. The higher than standard percentages of Si were observed at the Volcanoes National Park at Kilauea could possibly be due to the high content of Si in the basaltic lava field in which the test rack is situated. Similarly, the site at Pyramid Rock could have its higher than standard level of Si due to being exposed to the sandy beach nearby.

Chapter 5

CONCLUSIONS

In this study, the corrosion behavior, mechanical properties, and microstructure of similar AA6061-AA6061 and AA5086-AA5086 and dissimilar AA5086-AA6061 welds were examined for three exposure periods of 6-month, 1-year, and 2-year.

5.1 Corrosion Behavior

When comparing materials, the AA5086-AA5086 demonstrated best corrosion resistance at the most corrosive site, Kilauea. At other sites, the three materials exhibited comparable weight loss values that were generally within the bounds set by standard deviation bars for each material. Regarding exposure period, the corrosion rate consistently decreased as the time exposure increased. Comparing test sites, Kilauea (acid rain) generated the highest corrosion rates of all, Pyramid Rock (severe marine) was ranked second in corrosion rates, and the Waipahu (arid), Coconut Island (mild marine) and Lyon Arboretum (rain forest) sites produced significantly lower rates. Lyon Arboretum consistently generated the lowest corrosion rates which is highly likely to be related to the very low levels of chlorides.

5.2 Mechanical Properties

No consistent changes in yield strength based on exposure time or test site location were observed for all three materials. The slight variations in yield strength were likely due to slight variations in the weld properties. Comparing weld types showed that the AA5086-AA5086 had the highest yield strength by a small margin while AA6061-AA6061 and the AA6061-AA5086 were very similar. Lack of significant decreases in the yield strength was expected since the corrosion damage, i.e. decrease in cross-sectional areas, of the specimens were relatively low.

The AA5086-AA5086 welds had the highest UTS; however, there was large degradation in the UTS at Kilauea (acidic), Waipahu (arid), and Lyon Arboretum (rainforest) most likely due to sensitization of 5000-series aluminum alloys: Mg migrated to grain boundaries and caused cracking. For the AA6061-AA6061 and the AA6061-AA5086 welded specimens UTS did not change significantly for different exposure time and were fairly comparable with the latter being slightly lower. The AA6061-AA5086 specimens always fractured on the AA6061 side. The lower UTS of the AA6061-AA5086 welds compared to that of the AA6061-AA6061 welds indicate that the mixing of the AA6061 and AA5086 alloys during FSW had a slight deleterious effect.

Further investigation showed that some of the AA5086-AA5086 specimens experienced premature fracturing before fully elongated. For AA5086-AA5086 samples that fully elongated, the microstructure of the fracture surface was very fine and homogenous in color while the microstructure of the premature fracture surface was course with large cavities and non-uniform color.

The most ductile were AA5086-AA5086 welds accompanied with the largest variability. The variation in elongation to failure for the AA5086-AA5086 welds seemed to generally be an amplification of the variations seen in UTS. In general, AA6061-AA5086 had similar elongation percentage as AA6061-AA6061 with the latter having slightly higher ductility. AA5086-AA5086 had the highest elongation to failure with the least variation in samples from Pyramid Rock and Coconut Island. Currently, it is not known if the variation in elongation to failure is related to the surface temperature of the specimens, which could influence the sensitization of the AA5086-AA5086 welds.

5.3 Microstructure

Comparisons were made between unexposed AA6061-AA5086 welds and exposed AA6061-AA5086 welds from Kilauea, Pyramid rock, and Lyon Arboretum.

5.3.1 Comparison of Unexposed Parent Metal and the Two-Year, Kilauea-Exposed AA6061-AA5086 Weld Samples

5.3.1.1 Parent Material

The unexposed AA5086 and AA6061 parent metals exhibited slight signs of porosity or pitting, which may have resulted from polishing of the metallographic specimens. Traces of white precipitates were also observed on the specimens, which may have been corrosion products resulting from the polishing and subsequent cleaning process. The parent AA5086 and AA6061 zones of the dissimilar weld sample at Kilauea had significant accumulation and clustering of corrosion products. The unexposed AA6061 and AA5086 parent material did not show traces of carbon, whereas, the exposed samples showed significant amounts. The carbon content of the exposed samples could be due to carbonates such as calcium carbonate from coral sand, or organic matter such as algae or moss. Additionally, the oxygen percentage for the unexposed samples of the parent material zones was less than 2% while oxygen percentage of the exposed sample at Kilauea was nearly 30%. Aluminum level was lower in the exposed sample. For example, the unexposed sample had over 90% Al while the exposed sample had less than 60%. The low oxygen and high aluminum content signifies very little corrosion while the high oxygen and low aluminum content indicates the presence of aluminum oxide corrosion products.

5.3.1.2 Heat Affected Zone

The heat affected zone on the AA5086 side of the unexposed sample showed signs of circular voids or pits along with sparse white corrosion product resulting from the polishing and subsequent cleaning process. The SEM results of the two-year sample at Kilauea did not show any signs of pitting, but they did show significantly more white corrosion products in large clusters. The HAZ for the AA6061 side of the unexposed sample had 98.43% Al while the same zone in the exposed sample almost 70% Al. Similarly, the HAZ of the AA5086 unexposed sample had 95.46% Al while the same zone in the exposed sample had almost 70% Al.

5.3.1.3 Thermo-Mechanically Affected Zone

The thermo-mechanically affected zone of the unexposed sample on the AA5086 side was more porous than the AA6061 side. This was not observed in the exposed sample, but porous regions could have been hidden under the corrosion product layer. The TMAZ of the unexposed AA5086 side had pits that were irregular in shape while the TMAZ of the unexposed AA6061 side had circular pits. The exposed samples showed signs of cracks in the corrosion product layer only and no pits were visible. Corrosion products were significantly more on the exposed samples. There was a slight rise of Si percentage in some of the exposed sample that could have been related to mineral deposits from the surrounding environment

5.3.1.4 Nugget Zone

In the nugget zone of the unexposed sample, pits or porosity were present on the topside and even more on the underside. On the exposed sample, pit were not visible, but could have been hidden under the corrosion products.

5.3.2 Comparison of Two-Year Exposure Samples at Kilauea, Pyramid Rock, and Lyon Arboretum

There were some general trends among the samples at the various sites. Kilauea was the most corrosive site. Generally at all of the sites, the percentage of aluminum tended to be higher and oxygen lower closer to the NZ. In the outer zones, aluminum tended to be lower and oxygen higher with increasing distance from the NZ. This trend is indicative of lower amounts of corrosion in the NZ and higher amounts of corrosion farther from the NZ.

Most of the oxygen-to-aluminum ratios from the EDXA analyses did not match up stoichiometrically with that of typical aluminum corrosion products. Aluminum hydroxide $Al(OH)_3$ and aluminum oxide Al_2O_3 have O-to-Al ratios of 3:1 and 1.5:1, respectively. At Kilauea, where the corrosion rates were highest, it would be expected that the uncleaned, exposed samples analyzed in the SEM would have shown O-to-Al ratios similar to that of the aluminum corrosion products; whereas, in fact, the O-to-Al ratios ranged from 1:1 to 1:3 for the various specimens. One explanation for this incongruity could be due to the presence of acid rain at Kilauea that could wash away most of the $Al(OH)_3$ or Al_2O_3, both of which are amphoteric. If the oxide layer is thin, the EDXA sampling volume will include substrate aluminum, hence, decreasing the O-to-Al ratio. At Pyramid Rock, the O-to-Al ratios were approximately 1:1 but still lower than the expected 3:1 or 1.5:1 ratio. At Lyon Arboretum, where corrosion rates were the least of the three sites, the O-to-Al ratios ranged from approximately 1:5 to 1:15.

Other abnormal element percentages can also be explained. Carbon presence was appreciable at the three sites, particularly Lyon Arboretum. The high percentage of carbon at Lyon Arboretum could be attributed to the algae or moss growth or transfer of organic matter from nearby plants. The higher than standard percentages of Si observed at the Volcanoes National Park at Kilauea could possibly be due to the high content of Si in the basaltic lava field in which the test rack is situated. Similarly, the samples from Pyramid Rock could have higher than standard level of Si due to being exposed to the sandy beach nearby.

References

[1] Mahoney, M. W., and Mishra, R. S., 2007, "Friction Stir Welding Process," ASM International, United States, Chap. 5.

[2] Thomas, W. M., 1997, "Friction Stir Welding for the Transportation Industries," Materials and Design, Abington Hall, Abington, Cambridge, pp.269-273.

[3] So, F., 2005, "Materials Science and Engineering: R: Reports," Vol. 50, pp. 1.

[4] Williams, S. W., 2001, "Welding of Airframes Using Friction Stir," Air and Space, Europe, pp. 64-66.

[5] Mahoney, M. W, Rhodes, C. G., Flintoff, J. G., Spurling, R. A., and Bingel, W. H., 1998, "Properties of Friction-Stir-Welded 7075 T651 Aluminum," Metallurgical and Materials Transactions A, Vol. 29A, pp. 4.

[6] Heinz, B., and Skrotzki, B., 2002, "Characterization of a Friction-Stir Welded Aluminum Alloy 6013," Metallurgical and Materials Transactions B. Vol. 33(3), pp. 491.

[7] Su, J. Q., Nelson, T. W., Mishra, and R., Mahoney, M., 2003, "Microstructural Investigation of Friction Stir Welded 7050-T651 Aluminum," Acta Materialia, Vol. 51(3), pp.713-729.

[8] Çam, G., and Mistikoglu, S., 2014, "Recent Developments in Friction Stir Welding of Al-alloys,"Journal of Materials Engineering and Performance, Vol. 23(6), pp.1940.

[9] Mishra, R.S., and Ma, Z.Y., 2005, "Friction Stir Welding and Processing", Mater. Sci. Eng. R, Vol. 50, pp. 1–78.

[10] Threadgill, P.L., Leonard, A.J., Shercliff, H.R., and P.J. Withers, 2009, "Friction Stir Welding of Aluminium Alloys," Int. Mater. Rev., Vol. 54, pp 49–93.

[11] Rhodes, C.G., Mahoney, M.W., Bingel, W.H., Spurling, R.A., and Bampton, C.C., 1997, "Effects of Friction Stir Welding on Microstructure of 7075 Aluminum," Scripta Materialia, Vol.36(1), pp.69-75.

[12] Fuller, C. B., Mahoney, M.W., Calabrese, M., and Micona, L., 2010, "Evolution of Microstructure and Mechanical Properties in Naturally Aged 7050 and 7075 Al Friction Stir Welds," Materials Science & Engineering A, Vol. 527(9), pp.2233-2240.

[13] Sato, Y.S., Kokawa, H., Enmoto, M., and S. Jogan, 1999, Metallurgical and Materials Transactions A, Vol. 30, pp. 2429.

[14] Jata, K.V., Sankaran, K.K., and Ruschau, J.J., 2000, Metallurgical and Materials Transactions A, Vol. 31, p. 2181

[15] Silva, A. C. F., Braga, D.F.O., Figueiredo, M. A. V., and Moreira, P. M. G. P., 2015, “Ultimate Tensile Strength Optimization of Different FSW Aluminium Alloy Joints,” The International Journal of Advanced Manufacturing Technology, Vol. 79 (5), pp. 805-814.

[16] Krasnowski, K., Hamilton, C. , and Dymek, S., 2015, “Influence of the Tool Shape and Weld Configuration on Microstructure and Mechanical Properties of the Al6082 alloy FSW Joints,” Archives of Civil and Mechanical Engineering, Vol. 5, pp. 133-141.

[17] Aditya, S. K., 2015, “Analysis of Friction Stir Welding of Aluminum Alloys and Optimization of Welding Parameters for Maximum Tensile Strength,” International Journal of Engineering Research and Applications, Vol. 5 (5) pp. 39.

[18] Shigematsu, I., Kwon, Y.J., Suzuki, K., Imai, T., and Saito, N., 2003, “Joining of 5083 and 6061Aluminum Alloys by Friction Stir Welding,” Journal of Materials Science Letters, Vol. 22, pp. 353-356.

[19] Leitao, C., Leal, R.M., Rodrigues, D.M., Loureiro, A., and Vilaca, P., 2008, “Mechanical Behaviour of Similar and Dissimilar AA5182-H111 and AA6016-T4 Thin Friction Stir Welds,” Estudo Geral, Universidade de Coimbra, pp.1.

[20] Miles, M., Nelson, T., and Melton, D., 2005, “Formability of Friction-Stir-Welded Dissimilar-Aluminum Alloy Sheets,” Metallurgical and Materials Transactions A, 2005, Vol. 36 (1), pp. 3335-3342.

[21] Davis, J. R., 1999, “Corrosion of Aluminum and Aluminum Alloys,” ASM International, Chap. 2.

[22] Hatch, J. E., 1984, “Aluminum Properties and Physical Metallurgy,” ASM International, Ohio, Chap. 7.

[23] Chen., Z., 2014, “Microstructure Characterization, Mechanical Properties, and Corrosion Behaviors of Friction Stir Welded AA5086 and AA6061,” Master’s Thesis at University of Hawai’i at Manoa, Chap. 5.

[24] Nakayama, Y., Takaai, T., and Jin, D., 1996, “Precipitation Behaviors of β-Phase and Changes in Mechanical Properties of AL-MG System Alloys,” Materials and Science Forum, Vol. 217–222, pp. 1269– 1274.

[25] Sanders, T.H. Jr., Starke, E.A. Jr., and Cassada, W.A., 1994, “Aluminum Alloys—Their Physical and Mechanical Properties,” Materials Science Forum, Atlanta, USA, Vol. (1), pp. 378–385.

[26] Popovic, M., and Romhanji, E., 2008, “Characterization of Microstructural Changes in an Al-6.8wt% Mg alloy by Electrical Resistivity Measurements,” Material Science and Engineering A, Vol. (492), pp. 460–467.

[27] Smith, W.F., 1981, “Structure and Properties of Engineering Alloys,” McGraw-Hill Companies, Inc.

[28] “Vectrax - 9 Inch Wide x 48 Inch Long Table, Variable Speed Pulley Control, 3 Phase Knee Milling Machine,” MSC Industrial Supply Co., http://www.mscdirect.com/product/details/72526049.

[29] “Rainfall Atlas of Hawai’i,” Geography Department-University of Hawai’i at Manoa, http://rainfall.geography.hawaii.edu/history.html.

[30]”Volcanic Gas,” USGS, http://volcanoes.usgs.gov/hazards/gas/volgaspollution.php.

[31] Climate of Hawai’i,” Geography Department-University of Hawai’i at Manoa, http://climate.geography.hawaii.edu/interactivemap.html.

[32] Giambelluca, T.W., Shuai, X., Barnes, M.L., Alliss, R.J., Longman, R.J., Miura, T., Chen, Q., Frazier, A.G., Mudd, R.G., Cuo, L., and Businger. A.D., 2014, “Evapotranspiration of Hawai‘i. Final report submitted to the U.S. Army Corps of Engineers—Honolulu District, and the Commission on Water Resource Management, State of Hawai‘i,” http://climate.geography.hawaii.edu/howtocite.html.

[33] “Lyon Arboretum,” University of Hawai’i at Manoa, http://manoa.hawaii.edu/lyonarboretum/about/.

[34] 2005, “Aluminum and Magnesium Alloys, Specification for Aluminum and Aluminum-Alloy Sheet and Plate,” ASTM Standard B0209M-04, Vol. 02(02).